International Journal of Hydrogen Energy 232 (2026) 155001

Contents lists available at ScienceDirect

International Journal of Hydrogen Energy

journal homepage: www.elsevier.com/locate/he

Multi-objective optimization of hydrogen-integrated hybrid renewable energy systems using an adaptive evolutionary framework☆

Waqar Ali Khan [a,b], Ashkan Pakseresht [c], Caslon Chua [a], Ali Yavari [a,b,*]

[a] School of Science, Computing and Engineering Technologies, Swinburne University of Technology, Melbourne, Victoria 3122, Australia
[b] Hydrogen 4.0 Lab, Swinburne University of Technology, Melbourne, Victoria 3122, Australia
[c] Brunel Business School, Brunel University London, Uxbridge UB8 3PH, United Kingdom

ARTICLE INFO

Keywords:
Hydrogen-integrated hybrid renewable energy system (H-HRES)
Hybrid renewable energy system (HRES)
Multi-objective optimization
Energy dispatch management system
Sustainable energy systems

ABSTRACT

The optimization of Hydrogen-Integrated Hybrid Renewable Energy Systems remains challenging due to conflicting objectives, nonlinear operational constraints, and the limited adaptability of conventional evolutionary algorithms. This study introduces an adaptive Non-dominated Sorting Genetic Algorithm II (NSGA-II) framework that integrates dynamic mutation, selective local search, constraint-aware offspring generation, and cross-run learning. The method is applied to a residential-scale hybrid hydrogen–renewable energy system in Broadmeadows, Melbourne, comprising photovoltaic panels, wind turbines, battery storage, proton exchange membrane electrolyzers, hydrogen tanks, fuel cells, and diesel backup. Four objectives are considered: levelized cost of electricity (LCOE), carbon dioxide (CO_2) emissions, non-renewable hours (NRH), and renewable energy fraction (REF) penalty. The optimization is performed within a dispatch-coupled model that enforces hourly energy balances and state-of-charge limits, supported by demand and resource forecasts generated using extreme gradient boosting models trained on long-term meteorological data. The proposed adaptive NSGA-II achieves stronger performance than the conventional NSGA-II across hypervolume, Pareto diversity, and convergence indicators. The optimal designs favor greater storage capacity, with battery capacity rising from 105 MWh to 112 MWh, hydrogen storage increasing from 0.39 tons to 1.0 ton, and electrolyzer capacity growing from 4.8 MW to 5.2 MW. These adjustments reduce LCOE from 5.9169 to 5.8083 AUD/kWh, lower annual CO_2 emissions by 45% (from 94 tons/year to 52 tons/year), improve REF from 82.34% to 88.41%, and decrease NRH from 103 to 53 h. The results demonstrate that adaptive NSGA-II produces balanced solution portfolios that support high renewable utilization, reduce reliance on fossil backup, and provide practical insights for planning hydrogen-integrated sustainable energy systems.

1. Introduction

Global energy systems remain dominated by fossil fuels, which in 2023 still supplied over four-fifths of total primary energy demand [1]. This dependence keeps CO_2 emissions on an upward trajectory, reaching an estimated 41.6 gigatons of carbon dioxide ($GtCO_2$) in 2024, about 2% higher than the previous years [2,3]. The need to transition to cleaner energy is evident worldwide, but it is particularly pronounced in Victoria, Australia, where electricity generation contributes more than half of state-wide Greenhouse Gas (GHG) emissions [4]. Climate projections for Victoria indicate a 2.4 °C rise in average temperature, a doubling in the number of very hot days, longer fire seasons, and heavier rainfall extremes in coming decades [5]. To mitigate these risks and strengthen energy security, there has been a significant global shift in recent years toward Renewable Energy (RE) systems [6,7]. However, despite rapid growth in RE deployment driven by climate and security imperatives, the variability of renewable resources remains a central challenge. Solar and wind are abundant but intermittent, and reliance on fossil-fuel backup during low-renewable periods increases both system cost and carbon intensity [8].

HRES, which integrate multiple renewable sources with energy storage, have emerged as a promising solution to address these challenges by stabilizing supply through diversified generation [9,10]. Among available storage options, hydrogen stands out for its suitability for long-duration and seasonal storage, its high specific energy density, and its ability to link the power sector with other sectors via power-to-hydrogen and hydrogen-to-power pathways [11,12]. Building on

☆ This article is part of a Special issue entitled: 'Green Cities (Ramadan)' published in International Journal of Hydrogen Energy.

* Correspondence to: John Street, Hawthorn, Victoria, 3122, Australia
E-mail addresses: wkhan@swin.edu.au (W.A. Khan), ashkan.pakseresht@brunel.ac.uk (A. Pakseresht), cchua@swin.edu.au (C. Chua), mail@aliyavari.com (A. Yavari).

https://doi.org/10.1016/j.ijhydene.2026.155001
Received 21 December 2025; Received in revised form 12 February 2026; Accepted 10 April 2026
Available online 16 April 2026
0360-3199/© 2026 The Authors. Published by Elsevier Ltd on behalf of Hydrogen Energy Publications LLC. This is an open access article under the CC BY license (http://creativecommons.org/licenses/by/4.0/).

these advantages, H-HRES couple electrolyzers and fuel cells with PV, wind, and short-term storage such as batteries to extend the benefits of hydrogen storage. In an H-HRES, surplus renewable electricity can be converted to hydrogen during periods of oversupply, stored, and later reconverted to power when renewable output is low [13]. This mechanism effectively decouples generation from consumption, reduces curtailment, and improves system resilience under high RE penetration [14,15]. Designing such systems is inherently multi-objective. Economic objectives (such as system cost or LCOE) must be balanced against environmental impacts (e.g., CO_2 emissions) and reliability metrics (such as unmet load or REF), which often conflict. Moreover, enforcing operational constraints—such as electrolyzer and fuel-cell operating limits, hydrogen-storage capacity, and battery State of Charge (SOC) boundaries—greatly increases the complexity of the optimization problem [16,17]. These constraints require a detailed dispatch simulation and further enlarge the search space the optimizer must navigate.

To address this complexity, multi-objective optimization approaches have become standard in HRES planning. Pareto-based optimization yields a set of non-dominated solutions instead of a single optimum, allowing decision-makers to evaluate explicit trade-offs among objectives [18]. Evolutionary Algorithm (EA)s are well suited to such problems because they can approximate complex Pareto fronts without requiring convexity assumptions in the objective space. Among these, the NSGA-II has been the most widely used for HRES design [18–21]. Other techniques, including Multi-objective Particle Swarm Optimization (MPSO), Grey Wolf Optimizer (GWO), Technique for Order Preference by Similarity to Ideal Solution (TOPSIS) and more recent Non-dominated Sorting Genetic Algorithm III (NSGA-III) variants, have also been applied [22–25]. These algorithms have been used in grid-connected and off-grid settings [23] to minimize cost (e.g., LCOE), reduce CO_2 emissions, and maintain supply reliability. In some studies, such as [26,27], additional objectives such as energy autonomy or curtailment reduction have been included to reflect specific project priorities.

Existing studies on hydrogen-integrated HRES widely in system scope and methodological depth. Early work focused on PV–wind systems with electrolyzer-based hydrogen storage and used single-objective or bi-objective formulations based on cost or net-present-cost minimization under simple reliability constraints (e.g. satisfying a loss-of-load probability) [15,28–31]. Studies, such as [32,33] have expanded this scope by combining hydrogen with batteries to improve renewable utilization and supply reliability. Other contributions [34,35], apply hybrid optimization methods, where metaheuristic algorithms are combined with mathematical programming (e.g. Genetic Algorithm (GA) combined with Mixed-integer Linear Programming (MILP))to improve tractability under operational constraints. While [36], employ advanced evolutionary methods have also been introduced; for example, hypervolume-guided NSGA-III has been used to maintain solution diversity in higher-dimensional problems. System configurations have broadened as well, from PV–wind–hydrogen (H_2) microgrids to designs incorporating second-life Electrical Vehicle (EV) batteries or geological hydrogen storage [37–39]. Case-study applications used in [29,40,41] highlight site-specific benefits such as off-grid resilience or reduced reliance on diesel, but dispatch strategies are often simplified, limiting realism. These studies simplify the operational dispatch strategy (using, for instance, rule-based dispatch or coarse time-steps), which can under-represent hourly balancing, ramping dynamics, and the operating limits of electrolyzers, fuel cells, or batteries. Such simplifications risk biasing the estimated cost, performance, and feasibility of the solutions. Recent review [21,27,42–45] report similar issues and note that most optimization studies consider only a narrow set of objectives, mainly cost, emissions, and reliability, while detailed operational modeling is often omitted.

Table 1 summarizes these recent H-HRES optimization studies in a comparative format and highlights patterns that are not visible when the studies are viewed individually. The Table 1 shows substantial variation in dispatch realism and constraint enforcement across the literature. Decision-support tools such as weighted ranking or stakeholder-oriented sensitivity analysis appear in only a few studies. Benchmark testing of optimization algorithms is also uncommon. It also indicates that objectives related to NRH or REF compliance appear infrequently. These observations point to the need for optimization frameworks that include broader objective sets, realistic dispatch coupling, and structured post-optimization decision support.

To address the gaps identified in the literature, this paper proposes a comprehensive multi-objective optimization framework for H-HRES that integrates four key elements. First, the optimization problem is expanded to include a four-objective formulation that captures economic, environmental, and reliability priorities simultaneously. The objectives are to minimize the LCOE, CO_2 emissions, reliance on NRH, and a penalty for insufficient renewable energy fraction (REF shortfall). This broader objective set explicitly incorporates energy security and policy compliance through the NRH and REF metrics, in addition to cost and emissions. Second, each candidate solution is evaluated through a dispatch-coupled simulation. The time-series model enforces hourly energy balance and the operational limits of the battery, electrolyzer, fuel cell, hydrogen storage system, and any backup generator. By coupling the optimizer with a realistic dispatch model, only technically feasible solutions remain in the search space. Third, the framework incorporates decision-support analysis beyond the raw pareto front. After obtaining the pareto-optimal set, a weighted ranking approach is applied and sensitivity analyses are conducted on stakeholder preference weights. This allows identification of solutions that remain attractive under different priority scenarios, such as cost-driven utilities, emissions-constrained policymakers, or resilience-oriented communities. Finally, the methodology is validated on benchmark test functions of varying complexity to assess the optimizer's performance in a general context. By comparing results on standard multi-objective benchmark problems, the convergence, diversity, and robustness of the proposed adaptive algorithm are evaluated beyond the specific case study.

We implement this framework using an A-NSGA-II algorithm tailored for H-HRES. The A-NSGA-II introduces dynamic parameter adaptation, including mutation strength adjustments, and uses clustering-based initialization to maintain population diversity while accelerating convergence in the large solution space. The system model co-optimizes the capacities of PV, wind, battery storage, hydrogen storage, and a backup diesel generator under the four-objective formulation as mentioned above. The dispatch simulation ensures that each configuration meets hourly demand within component constraints. A real-world case study in Broadmeadows, Melbourne (Australia), is used to demonstrate the approach. The simulation employs a full year of hourly demand data and locally measured weather profiles, and incorporates a forecasting module for solar irradiance and wind speed to emulate realistic operation. This testbed captures demand variability, renewable intermittency, and component-level limitations, and highlights the trade-offs faced by planners. The optimization produces a diverse set of high-quality system designs, which are then analyzed through the decision-support tools to identify robust choices under varying stakeholder priorities.

Building on this framing, the present work is guided by four interrelated research questions:

1. How does the A-NSGA-II compare with conventional NSGA-II in optimizing H-HRES across four key objectives: LCOE, CO_2 emissions, REF, and NRH?
2. In what ways does the A-NSGA-II provide more practical and policy-aligned solutions when combined with weighted ranking and sensitivity analysis under different stakeholder priorities?
3. How do performance indicators such as hypervolume, convergence, and spacing describe the diversity and convergence behavior of pareto-optimal solutions in H-HRES optimization?

Table 1
Comparison of recent optimization studies on H-HRES, highlighting system configurations, objectives, algorithms, and decision-support features.

PV	Wind turbines (WT)	Battery	H_2 electrolyzis	H_2 fuel cell	H_2 storage	Diesel	Other	Objectives	Algorithm	Dispatch realism	Decision support	Ref.
✓	✓	✓	✓	✓	✓	–	–	Cost, Reliability	NSGA-II + metamodel	Simplified	–	[29,32]
✓	✓	✓	✓	–	✓	–	–	Cost, Efficiency	NSGA-II variant	Simplified	–	[29]
✓	✓	✓	–	–	–	–	Thermal	Cost, CO_2, Reliability	NSGA-III	Constraint-aware	Hypervolume	[28]
✓	✓	–	✓	✓	✓	–	–	Cost, CO_2, Reliability	Multiple Multi-Objective Evolutionary Algorithm (MOEA)s	Mixed	–	[46]
✓	✓	✓	✓	✓	✓	–	–	Various	Multiple MOEAs	Mixed	–	[35]
✓	–	✓ (EV)	✓	✓	✓	–	EV battery reuse	Cost, CO_2, Reliability	NSGA-II	Hourly	Long-term evaluation	[36]
✓	✓	–	✓	–	Salt cavern	–	–	Cost, Net-zero match	GA + MILP	Bi-level	Sensitivity	[39]
✓	✓	–	✓	✓	✓	–	–	Cost, Efficiency	MOEA	Simplified	–	[37]
✓	✓	✓	✓	✓	✓	–	–	Cost, CO_2, Reliability	NSGA-II	Dispatch	Benchmark tests	[38]
✓	✓	✓	✓	✓	✓	–	–	Cost, CO_2, Reliability, REF	GA/PSO	Hourly dispatch	Sensitivity	[40]
–	✓	✓	–	✓	✓	–	–	Reliability, Stability	NSGA-II	Dispatch	Convergence + spacing metrics	[21]
✓	✓	✓	✓	✓	✓	✓	–	Cost, CO_2, NRHs, REF penalty	A-NSGA-II	Dispatch-coupled	Sensitivity + Weighted ranking + Benchmarks	Proposed system (this work)

4. How does the A-NSGA-II perform on benchmark problems of varying complexity, relative to conventional NSGA-II, in terms of generalizability and pareto front quality?

By addressing these questions, the study aims to provide evidence that supports energy planners, policymakers, and industry stakeholders in selecting H-HRES configurations that balance cost, emissions, and resilience.

The remainder of this paper is organized as follows. Section 2 introduces the Broadmeadows case study and details the data preparation, component modeling, and mathematical formulation of the H-HRES problem. The optimization setup is also described in Section 2, including the configuration of the conventional NSGA-II and the proposed A-NSGA-II algorithm. Section 3 presents the results, with emphasis on the optimization outcomes, the decision-support findings, and the performance comparison between conventional NSGA-II and proposed A-NSGA-II, including benchmark tests and pareto front quality metrics. Section 4 provides the discussion, focusing on the implications for H-HRES design, policy relevance, and the broader role of hydrogen in distributed energy systems. Section 5 concludes the paper by highlighting the main findings and suggesting directions for future research.

2. Methodology and system overview

This section summarizes the end-to-end methodological framework used to model and optimize the proposed H-HRES for the Broadmeadows case study. It first introduces the study area and input datasets, then details the forecasting pipeline for solar and wind resources, the component-level techno-economic models, and the dispatch-coupled hourly simulation used to evaluate candidate designs. Finally, the conventional NSGA-II and the proposed A-NSGA-II optimization configurations are described, leading to Pareto-optimal system sizing outcomes.

2.1. Study area and data sources

This subsection describes the geographical context of the case study and the datasets used to construct the modeling framework. It outlines the climatic characteristics of Broadmeadows, the household demand profile, and the meteorological inputs adopted for solar irradiance and wind speed forecasting. These datasets form the foundation for the subsequent resource prediction, dispatch simulation, and multi-objective optimization processes.

2.1.1. Study area

The present study focuses on Broadmeadows, a suburban residential district located in the northern metropolitan region of Melbourne, Victoria, Australia. Geographically situated at approximately 37.68°S latitude and 144.92°E longitude. Broadmeadows lies within the temperate climate zone of southeastern Australia, experiencing mild winters and warm summers. The area is characterized by a mix of detached dwellings and low-rise apartment housing, making it representative of suburban energy consumption patterns in Australian urban planning.

Broadmeadows has been previously identified as a suitable location for HRES design due to its dual access to solar and wind resources, relatively stable weather trends, and proximity to established grid infrastructure. As highlighted in our prior techno-economic assessment, the suburb exhibits average daily Global Horizontal Irradiance (GHI) values in the range of 4.0–5.5 kWh/m^2 and moderate annual wind speeds at turbine hub height, offering a viable foundation for integrating PV and wind-based generation technologies.

In addition to its renewable resource potential, Broadmeadows serves as a suitable testbed for hydrogen-based energy transition frameworks due to the policy interest in distributed energy resilience, particularly in low-to-medium-density residential regions. The present study extends our earlier work by incorporating advanced optimization strategies and predictive modeling to evaluate optimal HRES configurations with hydrogen and diesel backup integration, tailored to the local

Table 2
Input meteorological variables used for forecasting.

Variable	Unit	Description
Solar Irradiance (ALLSKY_SFC_SW_DWN)	W/m^2	All-sky surface shortwave radiation
Temperature (T2M)	°C	Air temperature at 2 m
Relative Humidity (RH2M)	%	Relative humidity at 2 m
Surface Pressure (PS)	kPa	Surface atmospheric pressure
Wind Speed (WS10M)	m/s	Wind speed at 10 m
Cloud Cover (CLRSKY)	%	Clear sky frequency estimate

climatic and demand conditions in Broadmeadows. To model energy generation dynamics at high temporal resolution, we next describe the meteorological inputs and processing pipeline adopted for this study.

2.1.2. Meteorological data sources and processing

To enable high-resolution RE forecasting, this study employed historical meteorological data from 2012 to 2022 for the Broadmeadows site, sourced from National Aeronautics and Space Administration Prediction Of Worldwide Energy Resources (NASA POWER) database. This dataset includes a comprehensive suite of atmospheric and temporal variables essential for modeling solar irradiance and wind speed. The complete list of input features is summarized in Table 2, encompassing direct and derived environmental variables such as solar radiation, temperature, humidity, wind vector components, surface pressure, and time-based indicators (e.g., hour, season).

A Machine Learning (ML)-based approach was adopted to improve forecasting accuracy beyond previous extrapolation techniques. Specifically, two gradient boosting regression models—one predicting hourly solar irradiance (I_{solar}), the other wind speed at 50 m ($WS_{50\ \text{m}}$)— were trained using hourly meteorological data from 2012 to 2022, with 2023 data used for validation. This approach was adapted and extended from the methodology proposed by [47], who demonstrated the reliability of gradient boosting for solar and wind forecasting across multi-year datasets. Model performance was assessed using Mean Absolute Error (MAE), Root Mean Square Error (RMSE), and R-squared (R^2). A complete outline of the pipeline, from feature engineering to hourly predictions for 2024, is presented in Algorithm 1.

Algorithm 1 Forecasting Hourly Solar Irradiance and Wind Speed for 2024 using Supervised Learning

Input:
  Historical meteorological data (2012–2022)
  Validation year: 2023
  Target variables: Solar irradiance (I_{solar}), Wind speed at 50m (WS_{50m})
// Step 1: Construct input feature vector
$X \leftarrow$ {ALLSKY_SFC_SW_DWN, CLRSKY_SFC_SW_DWN, T2M, RH2M, WS10M, WS50M, U10M, V10M, PS, hour, dayofyear, season}
// Step 2: Train prediction models
Train gradient boosting model f_1: $X \rightarrow I_{\text{solar}}$
Train gradient boosting model f_2: $X \rightarrow WS_{50m}$
// Step 3: Validate model performance on 2023 data
Evaluate f_1, f_2 using MAE, RMSE, and R^2
// Step 4: Forecast values for 2024
for each hour $h \in [1, 8784]$ **do**
  Predict $I_{\text{solar}}(h) \leftarrow f_1(X_h)$
  Predict $WS_{50m}(h) \leftarrow f_2(X_h)$
  Enforce $I_{\text{solar}}(h), WS_{50m}(h) \geq 0$
end for
Output: Predicted hourly values $\{I_{\text{solar}}(h)\}$, $\{WS_{50m}(h)\}$ for 2024

Table 3
Model performance on 2023 validation set.

Forecasted variable	RMSE	MAE	R^2
Solar irradiance (G(b))	3.7211	1.9151	0.9998
Wind speed at 50 m ($WS_{50\ \text{m}}$)	0.4315	0.3144	0.9731

Model performance on the 2023 validation dataset is presented in Table 3. Both forecasting models demonstrate high predictive accuracy and strong generalization capability for hourly-resolution applications. The solar irradiance model achieves exceptionally low error metrics, with an RMSE of 3.72 W/m^2 and an R^2 of 0.9998, indicating near-perfect fit and minimal deviation from actual values. Similarly, the wind speed model at 50 m attains an RMSE of 0.43 m/s and an R^2 of 0.9731, confirming robust performance across varying seasonal conditions. These results validate the reliability of the gradient boosting approach in capturing the non-linear dependencies inherent in renewable resource dynamics.

To mitigate the risk of overfitting and to verify the reliability of the high prediction accuracy reported in Table 3 (R^2 = 0.9998 for solar irradiance), a strict temporal validation strategy was adopted. Models were trained exclusively on historical meteorological data from 2012–2022 and evaluated on a fully unseen hold-out year (2023), ensuring chronological separation between training and validation datasets. No random shuffling across years was performed, thereby preserving the natural temporal structure of the data and preventing information leakage. All feature engineering and preprocessing steps, including scaling and hyperparameter tuning, were confined to the training dataset only. Hyperparameters for the gradient boosting models were optimized using cross-validation within the training period, and model selection was based on performance stability rather than peak accuracy alone. The very high R^2 value reflects the strongly periodic and physically deterministic nature of solar irradiance patterns (diurnal and seasonal cycles) rather than model overfitting. This temporal hold-out approach strengthens generalization reliability for the 2024 forecasting stage.

To visualize both seasonal patterns and the performance of the forecasting models, three diagnostic plots incorporating both actual and predicted values were generated. Fig. 1(a) shows monthly solar irradiance and wind speed, capturing the typical seasonal trends—solar irradiance exhibits a clear summer peak and winter dip, while wind speed remains comparatively stable throughout the year. Fig. 1(b) presents density scatter plots comparing actual versus predicted values for 2024, with points concentrated along the diagonal, confirming strong predictive agreement. Fig. 1(c) illustrates the distribution of prediction errors for both solar and wind. The solar irradiance model exhibits a sharply peaked error profile centered around zero with minor right skewness, indicating high accuracy and occasional overestimation. In contrast, the wind speed error distribution is nearly symmetric and normally distributed around zero, suggesting consistent and unbiased forecasting performance.

2.1.3. Demand profile estimation using machine learning

Accurate residential electricity demand forecasting plays a pivotal role in the design and operation of HRES, particularly when simulating system behavior under hourly dispatch constraints. In our previous study, we successfully developed a methodology to extend one week of measured household consumption data into a full-year demand profile for the Broadmeadows region [48]. That dataset now serves as the foundational basis for training predictive models to estimate electricity demand under future meteorological and temporal conditions.

This study employed a supervised ML approach to forecast hourly electricity demand for 2024. A training dataset was constructed using actual hourly demand records from 2023, augmented with meteorological variables obtained from the Photovoltaic Geographical Information

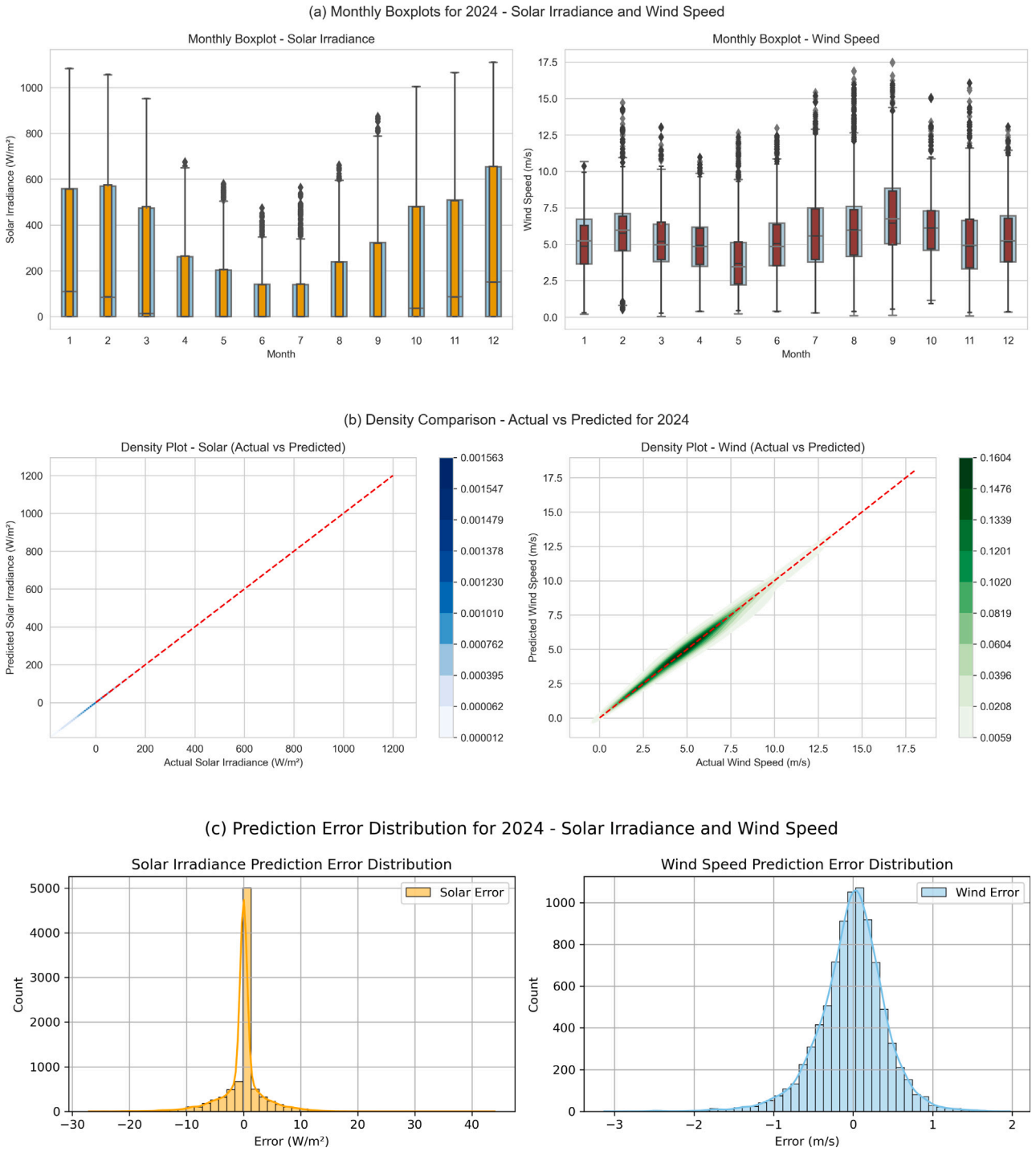

Fig. 1. Diagnostic evaluation of forecasting performance: (a) monthly variability, (b) predicted vs. actual scatter density, and (c) error distributions for solar irradiance and wind speed.

System Typical Meteorological Year (PVGIS (TMY)) dataset and temporal indicators representing user activity cycles. The feature space included nine atmospheric predictors — such as GHI, air temperature, dew point, wind speed, and cloud cover — alongside engineered time-based features capturing weekday/weekend effects, holiday markers, seasonal transitions, and peak-hour occupancy periods. This structured combination allowed the model to capture both physical influences and human behavioral signals affecting electricity usage. A summary of the predictor variables is provided in Table 4. The full demand forecasting workflow, including feature engineering, model training, and hourly prediction logic, is outlined in Algorithm 2.

Among the engineered features, "Temperature Deviation" represents the difference between the observed hourly ambient temperature and a seasonal reference baseline. It is defined in Eq. (1):

$$\Delta T(t) = T(t) - \bar{T}_{season} \tag{1}$$

where $T(t)$ is the observed ambient temperature at hour t, and $\bar{T}_{season}$ denotes the mean temperature of the corresponding season derived from the historical training dataset (2012–2022). This transformation captures relative thermal stress rather than absolute temperature levels, which is more closely associated with heating and cooling demand behavior. By modeling deviation from seasonal norms, the feature

Table 4
Input features for hourly electricity demand forecasting.

Feature name	Unit	Description
GHI	W/m^2	Global Horizontal Irradiance
DNI	W/m^2	Direct Normal Irradiance
DHI	W/m^2	Diffuse Horizontal Irradiance
Dry-bulb	°C	Ambient air temperature
Dew-point	°C	Dew point temperature
RHum	%	Relative humidity at 2 m
Wspd	m/s	Wind speed at 10 m
TotCld	Tenths	Total cloud cover
Pressure	mbar	Surface atmospheric pressure
Hour	(0–23)	Hour of the day
Day of week	Categorical	Day name (Monday–Sunday)
is_weekend	Binary	1 if Saturday or Sunday, 0 otherwise
is_holiday	Binary	1 if public holiday (Australian calendar)
Season	Categorical	Meteorological season (Summer, Autumn, Winter, Spring)
is_peak_hour	Binary	1 if hour falls in 7–10 AM or 5–9 PM window
Temperature deviation	°C	Difference from seasonal average ($T_{hour} - T_{season\_avg}$)
Extreme heat/cold	Binary	1 if deviation exceeds ±5 °C
Hour bin (encoded)	One-hot	Morning, afternoon, evening, night
Season (encoded)	One-hot	One-hot encoding of seasons

Table 5
Model performance on the 2023 validation dataset for hourly demand forecasting.

Model	MAE (kWh)	RMSE (kWh)	R^2
RF	596.24	887.31	0.8984
XGBoost	593.75	882.74	0.8698
LSTM neural network	704.97	980.14	0.8963

enables the XGBoost algorithm to learn nonlinear demand responses to temperature anomalies (e.g., heatwaves or cold snaps), improving generalization across inter-annual variability. Empirically, including temperature deviation reduced residual variance in extreme demand periods and improved stability of peak load prediction.

To identify the most suitable forecasting engine, this study evaluated three supervised learning models: Random Forest (RF), Extreme Gradient Boosting (XGBoost), and a Long Short-Term Memory (LSTM) neural network. These selections span both tree-based and deep learning paradigms, enabling the capture of complex non-linear and temporal dynamics in residential demand. This approach is consistent with recent advancements in the literature [49,50], where data-driven models have demonstrated strong performance under variable environmental conditions. A unified forecasting pipeline, applicable across all three models, is presented in Algorithm 2.

As presented in Table 5, the XGBoost model demonstrated superior performance on the 2023 validation set, achieving the lowest RMSE (882.74 kWh) and the highest coefficient of determination (R^2 = 0.8698). While RF produced comparable results, the LSTM model underperformed slightly, attributed to its sensitivity to hyperparameter tuning and the relatively limited sequence length in training data.

Based on these results, the XGBoost model was selected for 2024 demand simulation due to its superior accuracy, low bias, and consistent generalization across seasonal variations. This enabled the generation of robust demand signals to feed into the HRES dispatch model, ensuring realistic simulation of supply–demand dynamics. To evaluate the fidelity of the 2024 demand forecasts, Fig. 2 provides a visual comparison against historical 2023 consumption patterns. As shown in Fig. 2(a), the monthly predicted and actual electricity demand exhibit substantial overlap in medians and interquartile ranges, confirming the model's ability to preserve seasonal consumption structures. The Fig. 2(b) highlights a narrow, symmetrical distribution of hourly prediction errors centered around zero, indicating low bias and high consistency across the forecast horizon. Moreover, the time-series overlay in Fig. 2(c) compares the first week of hourly demand profiles between the two years. The predicted curve accurately replicates both the magnitude and timing of diurnal peaks, as well as intra-weekend variations, reflecting the model's strong capacity to learn and reproduce household load dynamics under temporal and climatic variability.

Algorithm 2 Household Demand Forecasting Using Machine Learning

Input:
  Hourly weather and temporal data for 2023:
    {GHI, DNI, DHI, Dry-bulb, Dew-point, RHum, Wspd, TotCld, Pressure}
    {Hour, Day, Weekday/Weekend, Holiday, Season, Peak-hour, Temperature deviation}
  Target variable: Hourly household electricity demand D
// **Step 1: Feature Engineering**
Derive binary flags: {is_weekend, is_holiday, is_peak_hour}
Compute season: {Summer, Autumn, Winter, Spring}
Calculate temperature deviation: $\Delta T = |T_{hour} - T_{season\ avg}|$
Detect extreme conditions: ($\Delta T > 5$°C) → {extreme_cold, extreme_heat}
One-hot encode: {Season, Hour Bin}
// **Step 2: Train ML Models**
Split data: 80% training, 20% validation (on year 2023)
Train models:
  $f_{RF} \leftarrow$ Random Forest on training set
  $f_{XGB} \leftarrow$ XGBoost on training set
  $f_{LSTM} \leftarrow$ LSTM with sequential hourly input
// **Step 3: Validate and Select Model**
Evaluate $\{f_{RF}, f_{XGB}, f_{LSTM}\}$ using MAE, RMSE, and R^2
Select best model f_{best} with lowest RMSE on validation set
// **Step 4: Forecast Demand for 2024**
for each hour $h \in [1, 8784]$ **do**
  Predict $D(h) \leftarrow f_{best}(X_h)$
end for
Output:
  Predicted hourly electricity demand values $\{D(h)\}$ for 2024

2.2. Hybrid system configuration and dispatch strategy

This subsection introduces the structural layout of the proposed HRES and explains the operational control logic governing energy flows between components. It outlines the electrical configuration of the DC and AC buses, the role of battery and hydrogen subsystems, and the hierarchical dispatch strategy used to prioritize renewable utilization while ensuring system reliability. These operational rules form the basis of the hourly simulation embedded within the optimization framework.

2.2.1. Proposed system layout

The system architecture of the HRES retains the validated configuration from our previous study. Which integrated rooftop and centralized PV generation, WTs, Battery Energy Storage System (BESS), and a hydrogen subsystem comprizing a Proton Exchange Membrane (PEM) electrolyzer, hydrogen tanks, and a fuel cell. Energy flows are coordinated through AC and DC buses, connected via a bidirectional power converter to enable flexible interaction among components. The DC bus accommodates PV arrays, battery, and electrolyzer, while WTs operate on the AC side. Distributed rooftop PV is prioritized for household-level consumption, and any surplus is combined with centralized PV and wind generation to address broader community demand. This staged utilization ensures maximum exploitation of available RE resources before engaging storage or backup systems. When renewable generation

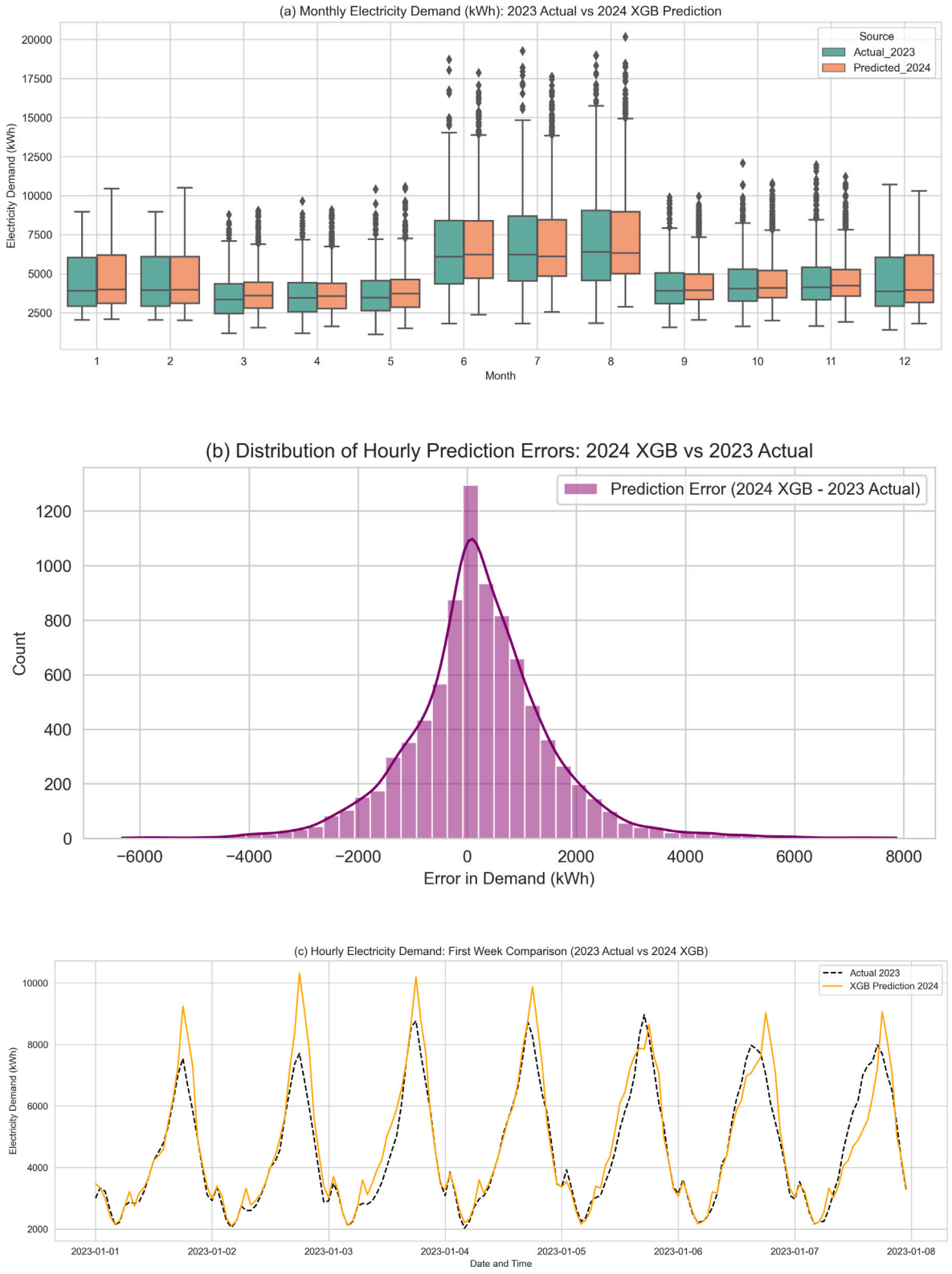

Fig. 2. Performance evaluation of XGB-based electricity demand forecasting. (a) Monthly electricity demand distribution for 2023 (actual) and 2024 (predicted); (b) Distribution of hourly prediction errors (kWh); (c) Hourly demand profile comparison during the first week of January.

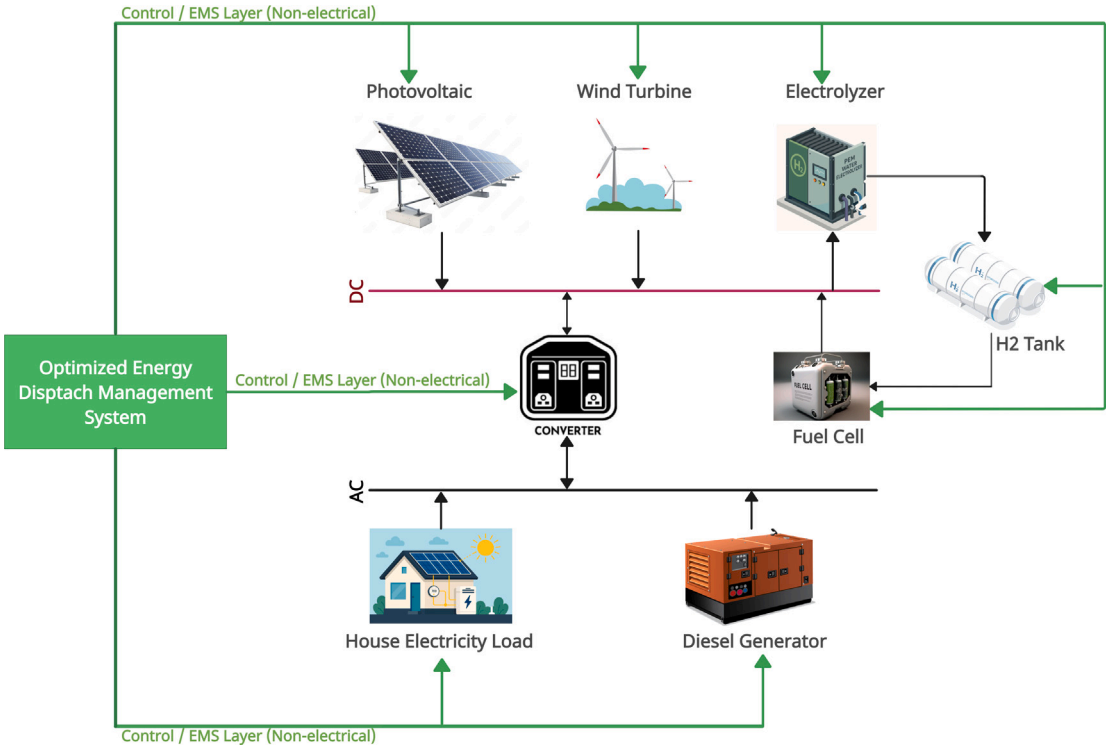

Fig. 3. Proposed HRES architecture showing DC and AC buses, hydrogen subsystem integration, and EMS supervisory control (green lines indicate non-electrical signals). (For interpretation of the references to color in this figure legend, the reader is referred to the web version of this article.)

and storage prove insufficient to meet the load, a diesel generator acts as a last-resort backup to maintain supply reliability.

In this work, the physical system is enhanced with an Energy Management Dispatch Strategy (EMDS) that governs real-time coordination of all components, as depicted in Fig. 3. The EMDS regulates energy flows, manages charging priorities (battery first, followed by hydrogen production), and activates backup dispatch only under sustained shortfalls. This optimization-driven dispatch architecture forms the foundation for the multi-objective analysis discussed in the following sections.

2.2.2. Component modeling and mathematical estimation

This subsection presents the mathematical models used to represent each physical component of the proposed HRES. Detailed formulations are provided for PV generation, WT output, battery storage dynamics, hydrogen production and storage, fuel cell operation, and diesel backup generation. These component-level models are integrated within an hourly dispatch simulation to ensure physically consistent energy balance during optimization.

2.2.2.1. Photovoltaic energy model. The estimation of PV energy generation in this study is based on a time-resolved irradiance-driven model that accounts for panel characteristics, site-specific solar input, and real-world efficiency losses [51]. This modeling approach builds upon the validated framework developed in our previous work, where the irradiance decomposition and system-level derating factors were comprehensively derived. The hourly direct beam irradiance $G_{b,i}(t)$ in (kWh/m^2) is converted into energy terms using the Eq. (2):

$$G_i(t) = \frac{G_{b,i}(t)}{1000} \tag{2}$$

where $G_i(t)$ is the global irradiance per unit area in kWh/m^2. The energy produced by a single panel during hour t is denoted as $E_{\text{panel}}(t)$, calculated using Eq. (3):

$$E_{\text{panel}}(t) = G_i(t) \cdot P_{\text{peak}} \cdot \eta_{\text{global}} \cdot A_{\text{sp}} \tag{3}$$

Here $P_{\text{peak}} = 0.4$ kW is the rated power of a standard panel, $A_{\text{sp}} = 2.1$ m^2 is the surface area of the panel, and η_{global} denotes the total system efficiency under operational conditions. The global efficiency term η_{global} multiplies physical and design-related losses and is defined in Eq. (4):

$$\eta_{\text{global}} = \eta_{\text{FF}} \cdot \eta_{\text{temp}} \cdot \eta_{\text{conn}} \cdot \eta_{\text{dirt}} \cdot \eta_{\text{safe}} \tag{4}$$

The simulation assumes a commercially available ESPSC 400 M PERC module [52], for which the form factor η_{FF} is calculated as 0.775 using standard current–voltage parameters of the panel [52]. The temperature correction coefficient $\eta_{\text{temp}} = 0.885$ is based on an operating cell temperature of 45 °C and a manufacturer-specified temperature coefficient. Additional derating terms are applied for inverter and wiring losses ($\eta_{\text{conn}} = 0.98$), while soiling-related degradation is estimated via ($\eta_{\text{dirt}} = 0.97$). A conservative safety factor ($\eta_{\text{safe}} = 0.95$) is applied to account for long-term uncertainties, yielding a total global efficiency of $\eta_{\text{global}} = 0.637$. All these values are defined in [52], which governs the real output per panel, as used in Eq. (3).

To quantify total rooftop PV generation, it is assumed that each household is equipped with 10 panels (i.e., a 4-kW system). The hourly total energy generated from rooftop installations, $E_{\text{rooftop}}(t)$, across $N_h = 4617$ households is calculated using Eq. (5):

$$E_{\text{rooftop}}(t) = E_{\text{panel}}(t) \cdot 10 \cdot N_h \tag{5}$$

For centralized PV plants, the number of installed panels (N_{panels}) is determined from the total installed capacity C_{pv} (in kW), as shown in Eq. (6):

$$N_{\text{panels}} = \frac{C_{\text{pv}}}{P_{\text{peak}}} \tag{6}$$

The total energy output of a PV plant (E_{PVplant}) is then given by Eq. (7):

$$E_{\text{PVplant}} = E_{\text{panel}}(t) \cdot N_{\text{panels}} \tag{7}$$

Together, Eqs. (2)–(7) form the complete PV modeling framework used in this study. This structure enables detailed simulation of solar

Table 6
Polynomial coefficients for Siemens SWT-2.1-114 wind turbine power curve.

Wind speed interval (m/s)	a	b	c	d
$1.5 \le v < 4.0$	−14.667	169.714	−298.905	170.057
$4.0 \le v < 11.5$	−1.448	−11.271	623.674	−1518.287
$11.5 \le v \le 25.0$	−0.861	39.621	−596.698	5043.653

electricity generation from both residential and utility-scale systems using hourly irradiance profiles under region-specific operating conditions, while maintaining consistency with the validated methodology presented in our previous studies.

2.2.2.2. Wind turbine model. The wind energy generation model employed in this study builds upon the spatially normalized framework developed in previous work, incorporating turbine layout constraints, availability losses, and land area normalization to ensure scalable and realistic energy estimation [53]. Wind power output is estimated for the Siemens SWT-2.1-114 WT using a piecewise polynomial function fitted to the manufacturer's performance curve, following the methodology outlined in [53,54].

The electrical output power $P_{WT}(t)$ of the turbine at wind speed $v(t)$ is expressed using Eq. (8):

$$P_{WT}(t) = \begin{cases} 0, & v < 1.5 \\ a_1 v^3 + b_1 v^2 + c_1 v + d_1, & 1.5 \le v < 4.0 \\ a_2 v^3 + b_2 v^2 + c_2 v + d_2, & 4.0 \le v < 11.5 \\ a_3 v^3 + b_3 v^2 + c_3 v + d_3, & 11.5 \le v \le 25.0 \\ 0, & v > 25.0 \end{cases} \tag{8}$$

where v is the wind speed at hub height (100 m), and the coefficients a_i, b_i, c_i, d_i correspond to different operational regions of the turbine. The polynomial coefficients derived for the Siemens SWT-2.1-114 turbine are summarized in Table 6 as defined in [54].

Turbine operation is restricted below the cut-in speed of 1.5 m/s and above the cut-out speed of 25.0 m/s to mitigate energy inefficiency and mechanical fatigue. The segmented polynomial structure ensures accurate modeling of start-up, ramp-up, and nominal output behavior. The fitted curves exhibit a coefficient of determination $R^2 > 0.995$ in all regions, confirming the fidelity of the curve-fitting process.

To incorporate spatial planning and turbine availability, the hourly wind energy output is normalized by land area and adjusted for operational uptime. The resulting energy output at time t is given by Eq. (9):

$$E_{wind}(t) = \frac{P_{WT}(v(t)) \cdot N_{WT} \cdot \alpha}{A_{WT}} \tag{9}$$

where N_{WT} is the number of turbines, $\alpha = 0.98$ is the availability factor, and $A_{WT} = 0.6498$ km^2 represents the effective area occupied per turbine.

The layout follows standard International Electrotechnical Commission (IEC) guidelines [55], assuming 10 rotor diameters spacing along the wind direction and 5 diameters perpendicular to it, based on a rotor diameter of 114 m. This modeling framework preserves alignment with established wind farm deployment practices and supports robust yield estimation within the hybrid energy system. It is fully consistent with the methodology adopted in our previous studies.

Although the Siemens SWT-2.1-114 turbine has been superseded in recent commercial catalogues, it was selected as a representative mid-scale utility-class turbine with publicly documented performance data and well-characterized power curves. The present study does not model an individual household installation, but rather a community-scale hybrid renewable energy system serving aggregated suburban demand in Broadmeadows. In this context, multi-megawatt turbines represent shared or distributed community wind assets rather than rooftop-scale devices. Importantly, the optimization framework relies on generic turbine power curve behavior and rated capacity, rather than dependence on a specific commercial product. Comparable modern turbines with similar rated power would yield equivalent optimization dynamics and would not alter the methodological conclusions of the study.

2.2.2.3. Battery model. In the proposed HRES, a battery storage model is employed to mitigate temporal mismatches between intermittent renewable generation and fluctuating load demand [56]. This model plays a central role in enhancing system flexibility by absorbing surplus electricity produced from PV and WT sources during periods of generation excess and subsequently discharging stored energy to meet demand during renewable shortfall events. Through this charge–discharge balancing mechanism, the battery storage model supports continuous energy supply, improves renewable energy penetration, and reduces reliance on diesel-based backup generation, thus contributing to a more sustainable and resilient energy architecture.

The system integrates a lead–acid battery configuration, utilizing the Hoppecke 2 V, 3000 Ah module, as established in prior literature [57]. Battery operations are governed to ensure that both charging and discharging occur strictly within predefined safety margins, thereby maintaining system stability and extending the operational lifespan of the battery units [58]. These safety margins are determined by the battery's SOC thresholds, which are bounded by the Depth of Discharge (DoD) constraints. During periods when renewable electricity generation exceeds the load demand, the surplus energy is primarily allocated to charge the battery. Should the battery reach its maximum SOC limit, any additional excess is subsequently redirected to the hydrogen electrolyzer for further utilization. Conversely, in periods of renewable energy deficit, the battery discharges stored energy until the SOC reaches its minimum permissible level. If the deficit persists beyond this threshold, the remaining demand is fulfilled by the hydrogen-based energy subsystems.

The net renewable power available at any given time step t, denoted as $P_{excess}(t)$, is evaluated by accounting for the aggregate generation from PV and WT systems minus the load demand adjusted for conversion losses as calculated in Eq. (10) [17]:

$$P_{excess}(t) = \frac{P_{PV}(t) + P_{WT}(t) - P_{load}(t)}{\eta_{conv}} \tag{10}$$

where $P_{PV}(t)$ and $P_{WT}(t)$ represent the instantaneous power generation from the PV array and WT, respectively; $P_{load}(t)$ is the load demand at time t; and η_{conv} is the AC–DC power conversion efficiency, assumed to be 0.95 in this study as defined in [59].

If $P_{excess}(t) > 0$, the battery charges using the surplus renewable power defined in Eq. (11):

$$SOC(t) = SOC(t-1) + \eta_{ch} \cdot P_{excess}(t) \cdot \Delta t \tag{11}$$

If $P_{excess}(t) < 0$, it indicates a RE shortfall, prompting battery discharge calculated according to Eq. (12):

$$SOC(t) = SOC(t-1) + \frac{P_{excess}(t)}{\eta_{dch}} \cdot \Delta t \tag{12}$$

Here, η_{ch} and η_{dch} represent the battery's charging and discharging efficiencies, both set to 0.90, consistent with typical lead–acid performance [58]. The time step Δt corresponds to 1 h.

To prevent deep discharge cycles and safeguard battery health, SOC is constrained within minimum and maximum bounds as defined in Eq. (13):

$$SOC_{min} \le SOC(t) \le SOC_{max} \tag{13}$$

These limits are derived from the DoD, specified at 90%, restricting discharges below 10% of full capacity [60]. The lower SOC bound is calculated using Eq. (14):

$$SOC_{min} = SOC_{max} \cdot (1 - DOD) \tag{14}$$

where $SOC_{max} = E_{rated} \cdot N_{bat}$ is the total energy capacity of the battery bank, with E_{rated} representing the energy capacity of a single battery unit (3000 Ah) and N_{bat} denoting the number of installed

battery units [59]. In this study, N_{bat} is treated as a continuous decision variable optimized through the multi-objective genetic algorithm.

Battery sizing was not determined using fixed autonomy heuristics (e.g., "x-hours of backup"), but was instead formulated as an optimization decision variable within the NSGA-II and A-NSGA-II search space. The genetic algorithm selects the target battery energy capacity E_{target} (kWh) within predefined bounds chosen to ensure deployable community-scale configurations and to prevent unrealistic oversizing. At each candidate solution, the dispatch simulation enforces feasibility through (i) SOC limits (Eqs. (13)–(14)), (ii) charge/discharge power limits (Eq. (17)), and (iii) the prioritized energy management order in which surplus renewable power charges the battery before hydrogen production. As a result, the final battery capacity emerges from Pareto-optimal trade-offs among LCOE, CO_2 emissions, NRH, and REF penalty, rather than from a single deterministic sizing rule.

The usable energy of one module, assuming a 2 V nominal voltage, is calculated using Eq. (15):

$$E_{battery} = \frac{V_B \cdot C_{single}}{1000} = \frac{2 \cdot 3000}{1000} = 6 \text{ kWh} \tag{15}$$

where $V_B = 2$ V and $C_{single} = 3000$ Ah. The factor of 1000 converts Wh to kWh.

Given a target energy capacity E_{target}, the required number of battery units can be calculated using Eq. (16):

$$N_{batt} = \frac{E_{target}}{E_{battery} \cdot DOD \cdot \eta_B} \tag{16}$$

where η_B is the battery round-trip efficiency, assumed to be 0.86.

To reflect practical operational limits, the battery's charge and discharge power at each timestep is constrained as expressed in Eq. (17) as defined in [61]:

$$0 \le P_{charge}(t) \le P_{charge,max}, \qquad 0 \le P_{discharge}(t) \le P_{discharge,max} \tag{17}$$

These constraints ensure that battery operation remains within manufacturer specifications under fluctuating conditions. Overall, the battery storage model reflects the physical dynamics and control constraints necessary for accurate dispatch modeling within the broader HRES. It serves as the primary buffer for renewable intermittency before engagement of hydrogen-based subsystems, whose modeling is discussed in the following section.

2.2.2.4. Electrolyzer. Within the HRES, the electrolyzer subsystem plays a critical role in converting excess electricity into hydrogen via electrochemical water splitting. This hydrogen is then stored and later reconverted to electricity through the fuel cell during RE deficits, thus enabling temporal decoupling between generation and consumption.

The proposed HRES adopts a PEM electrolyzer configuration due to its fast response, operational flexibility, and compatibility with variable renewable inputs [53]. The electrolyzer activates only after satisfying immediate demand and battery charging requirements, thereby ensuring surplus energy utilization occurs in a hierarchically optimized sequence. The hourly hydrogen production $H_{2,prod}(t)$ (in kg) is computed using Eq. (18) as given by [53]:

$$H_{2,prod}(t) = \begin{cases} \dfrac{P_{excess}(t)\,\eta_{ELC}}{HHV_{H_2}}, & \text{if } P_{excess}(t) \le P_{ELC,cap} \cdot \eta_{ELC} \\ \dfrac{P_{ELC,cap}(t)\,\eta_{ELC}}{HHV_{H_2}}, & \text{otherwise} \end{cases} \tag{18}$$

where $P_{excess}(t)$ denotes the net available surplus electricity at time t (kW), after satisfying both load demand and battery charging requirements; η_{ELC} is the electrolyzer efficiency, assumed to be 0.85; HHV_{H_2} represents the higher heating value of hydrogen, taken as 39.4 kWh/kg; and $P_{ELC,cap}$ is the rated capacity of a single electrolyzer unit [53].

In this study, the electrolyzer efficiency η_{ELC} is assumed to be constant over the operating range, an assumption commonly adopted in system-level HRES studies to balance modeling accuracy and computational tractability.

The piecewise formulation ensures that hydrogen production is capped when the available surplus exceeds the system's electrolyzer capacity, thereby reflecting realistic power conversion constraints. When $P_{excess}(t)$ is within the electrolyzer's rated capacity, the full excess power is used for electrolyzis. Otherwise, production is limited to the system's installed maximum capacity.

Electrolyzer operation is subject to upper-bound constraints to avoid oversizing and to maintain economic feasibility, and the system design ensures that electrolyzer deployment remains efficient under both high and low surplus scenarios. This modular approach facilitates scalability and supports robust system performance during extended renewable overproduction periods.

2.2.2.5. Hydrogen tank. The hydrogen tank functions as a critical energy buffer, storing hydrogen produced via electrolyzis during periods of RE surplus. This stored hydrogen is subsequently supplied to the fuel cell when generation from PV, wind, and battery sources is insufficient, thereby enhancing system autonomy and enabling extended operation during low-resource conditions [62]. The hydrogen tank is modeled as a pressurized vessel with a maximum capacity H_{max}, defined as a continuous decision variable in the system design.

Similarly, the hydrogen tank capacity H_{max} (kg) was treated as a design decision variable, selected by the optimizer within predefined bounds representing practical pressurized storage sizes for community-scale installations. The hourly dispatch model governs hydrogen feasibility through the mass-balance constraint (Eq. (19)) and storage limits (Eq. (20)), ensuring that hydrogen charging and depletion remain physically consistent under seasonal renewable variability. Hydrogen storage is therefore sized to serve long-duration energy shifting and resilience during extended renewable shortfalls, while the battery addresses short-duration diurnal balancing. The final H_{max} values reported in the results reflect optimal Pareto trade-offs under these operational constraints.

The mass of hydrogen stored at each time step t, denoted $H_{store}(t)$, is dynamically updated based on the net difference between the amount of hydrogen produced by the electrolyzer $H_{prod}(t)$ and the hydrogen consumed by the fuel cell $H_{fc}(t)$. This relationship is represented in Eq. (19) as defined in [32]:

$$H_{store}(t) = H_{store}(t-1) + H_{prod}(t) - \frac{H_{fc}(t)}{\eta_{HT}} \tag{19}$$

where η_{HT} is the hydrogen tank efficiency, assumed to be 0.95 in line with standard literature practices [29]. This formulation ensures mass balance and storage continuity, maintaining the operational constraint computed using Eq. (20):

$$0 \le H_{store}(t) \le H_{max} \tag{20}$$

Here, $H_{store}(t)$ is the hydrogen inventory in kilograms at time t, $H_{prod}(t)$ is the hydrogen transferred from the electrolyzer, and $H_{fc}(t)$ is the hydrogen supplied to the fuel cell. This model supports a realistic simulation of dynamic storage behavior across hourly dispatch intervals, enabling accurate assessment of diurnal and seasonal energy-shifting potential.

2.2.2.6. Fuel cell. The fuel cell subsystem serves as a critical backup mechanism within the HRES, enabling the conversion of stored hydrogen into electricity during periods of renewable generation and battery insufficiency. This electrochemical process operates only when the photovoltaic, wind, and battery components fail to meet the residual load, as outlined in earlier sections. The system employs a PEM fuel cell, chosen for its high efficiency, rapid response, and compatibility with intermittent hydrogen input [63].

The mass of hydrogen consumed by the fuel cell at each hourly interval, denoted as $H_{fc}(t)$ in kilograms, is computed based on the fuel cell's actual power output at that time $P_{fc}(t)$, as well as its rated

capacity $P_{fc,rated}$. This relationship is modeled using a linear function (Eq. (21)), which accounts for both baseline and load-dependent hydrogen requirements [64,65]:

$$H_{fc}(t) = f_{cic} \cdot P_{fc,rated} + f_{cs} \cdot P_{fc}(t) \quad (21)$$

Here, f_{cic} is the intercept coefficient representing fixed hydrogen consumption per unit of rated power, while f_{cs} denotes the slope coefficient corresponding to variable hydrogen usage per unit of actual output. For this study, these coefficients are set to $f_{cic} = 0.08$ kg/h/kW and $f_{cs} = 0.25$ kg/h/kW, respectively, following values established in prior literature [29]. Fuel cell efficiency is treated as constant in this study, while load-dependent operational behavior is captured through the linear hydrogen consumption model in Eq. (21).

This formulation captures the operational behavior of the PEM fuel cell under varying power demands, enabling accurate modeling of hydrogen depletion over time. By incorporating both static and dynamic consumption terms, the approach ensures realistic representation of system performance under dispatch conditions and supports comprehensive energy balancing across the hybrid configuration.

2.2.2.7. Diesel generator. The diesel generator serves as the auxiliary power source of last resort within the HRES. Its operation is intended to provide electricity during critical shortfalls when renewable generation, battery storage, and hydrogen-based components are insufficient to meet the residual demand [66]. The generator is assumed to operate in a binary (ON/OFF) mode with a fixed rated capacity P_{DG}^{rated}. The total energy supplied by the generator at time step t, denoted as $E_{DG}(t)$, is computed based on the remaining unmet load after exhausting PV, wind, battery, and fuel cell capacities. While its operational priority is intentionally minimized to reduce fossil fuel dependency and associated emissions, the diesel generator provides essential energy resilience during prolonged RE deficits, such as extended overcast or windless periods.

The fuel consumption of the generator $F_{DG}(t)$ is modeled using a linear function of its electrical output, as expressed in Eq. (22) [66]:

$$F_{DG}(t) = \alpha \cdot E_{DG}(t) + \beta \cdot P_{DG}^{rated} \quad (22)$$

Here, α represents the variable fuel consumption coefficient (L/kWh), and β represents the intercept accounting for idle consumption (L/kW-h). In this study, values of $\alpha = 0.3$ and $\beta = 0.05$ are adopted, consistent with operational data from similar distributed diesel units [65]. The associated CO_2 emissions are calculated by multiplying the diesel usage $F_{DG}(t)$ by the specific emission factor of diesel fuel (2.68 kg CO_2/L) [63], contributing to the overall environmental impact assessment within the optimization process.

This formulation ensures that diesel use is minimized and activated only when strictly necessary. It supports a realistic simulation of energy resilience under worst-case scenarios while enforcing environmental constraints through carbon emission accounting and non-renewable operation tracking.

2.2.2.8. Economical model. The economic analysis employed in this study quantifies the total cost of each hybrid configuration over its lifetime using the Net Present Cost (NPC) method [67]. This comprehensive formulation accounts for capital investment, component replacements, Operation and Maintenance (O&M) expenses, and energy-related fuel costs, normalized over the project horizon. The NPC of the entire HRES is calculated using Eq. (23) [68]:

$$NPC = C_{cap} + C_{rep} + C_{O\&M} + C_{fuel} \quad (23)$$

where, C_{cap} represents the initial capital expenditure, C_{rep} accounts for present-value replacement costs throughout the system's lifetime, $C_{O\&M}$ includes recurring maintenance and operational expenses, and C_{fuel} captures diesel fuel consumption costs, where applicable.

To enable fair comparison across different HRES configurations, the LCOE is computed based on the total NPC and the system's total energy generation using Eq. (24) as defined in [27]:

$$LCOE = \frac{NPC \cdot CRF}{E_{gen}} \quad (24)$$

Here, E_{gen} represents the total energy generated by the system (in kWh) over the project lifetime, i is the real discount rate, and n is the lifetime in years. The Capital Recovery Factor (CRF) used to annualize investment costs is calculated using Eq. (25) [27]:

$$CRF = \frac{i(1+i)^n}{(1+i)^n - 1} \quad (25)$$

This formulation ensures that all relevant economic factors—including upfront capital, recurring O&M, replacement cycles, and fuel usage—are consolidated into a single normalized cost per unit of energy generated. The techno-economic characteristics of all major system components, including capital cost, replacement schedule, and O&M rates, are presented in Table 7.

It is acknowledged that Capital Expenditure (CAPEX) values for emerging technologies such as battery storage and PEM electrolyzers are subject to market variability and technology learning effects. Reported literature, such as in [72,73], indicate that battery system CAPEX may vary by approximately ±15%–25% depending on chemistry, scale, and supply-chain conditions, while electrolyzer costs may fluctuate within ±20%–30% depending on manufacturing maturity and deployment scale. In this study, mid-range literature values [63,71] are adopted to ensure consistency and comparability across configurations. While explicit probabilistic cost modeling is beyond the scope of the present optimization, the sensitivity and multi-objective analysis framework allows trade-offs between cost, emissions, and reliability to be evaluated under these representative baseline assumptions.

To further contextualize the impact of hydrogen cost uncertainty, a qualitative parametric assessment was conducted by considering ±20% variation in electrolyzer and hydrogen tank capital expenditure, consistent with recent reported market volatility ranges. While the absolute LCOE values shift proportionally under these cost adjustments, the relative ranking between the conventional NSGA-II and A-NSGA-II configurations remains unchanged. The adaptive framework continues to demonstrate lower emissions and reduced non-renewable hours under all examined cost scenarios. This indicates that the comparative superiority of the A-NSGA-II solution is structurally driven by improved storage coordination rather than dependence on a specific hydrogen CAPEX assumption. A fully stochastic techno-economic uncertainty propagation is reserved for future work, as the primary objective of the present study is algorithmic and system-level comparative evaluation.

It is noted that hydrogen system capital costs in Table 7 represent aggregated subsystem costs including balance-of-plant components such as power electronics, gas handling units, and compression equipment required for pressurized gaseous hydrogen storage. In this study, hydrogen is assumed to be stored in compressed gaseous form at moderate pressure suitable for community-scale stationary applications. Liquefaction systems are not considered, as cryogenic hydrogen storage is typically associated with large-scale industrial or export-oriented infrastructure rather than distributed hybrid renewable systems. The adopted cost parameters therefore reflect integrated subsystem costs consistent with system-level techno-economic studies in the literature.

2.2.3. Energy management and dispatch strategy

An effective EMDS is central to the coordinated operation of HRES, particularly when multiple distributed and centralized energy sources are integrated. In the proposed system, the EMDS governs real-time interactions between PV modules, WT, the battery model, and hydrogen-based components (electrolyzer, storage tank, and fuel cell), along with diesel generators. Its core function is to ensure that energy supply consistently meets demand while maintaining system performance under varying resource and load conditions.

Table 7
Techno-economic specifications of hybrid energy system components.

Component	Technical data	Economic data	Reference
PV	Model: ESP5C 400 M PERC Efficiency: 20% Capacity: 0.4 kW/panel Lifetime: 15 years	Capital cost ($/kW): 980 Replacement cost ($/kW): 980 O&M cost: 2% of CAPEX	[51,52]
WT	Model: Siemens Gamesa SG 2.1-114 Cut-in speed: 1.5 m/s Cut-out speed: 25 m/s Capacity: 2.1 MW Lifetime: 20 years	Capital cost ($/kW): 50 000 Replacement cost ($/kW): 50 000 O&M cost ($/year): 1500	[53,69]
Battery	Model: Li-Ion Hoppecke Efficiency: 86% Voltage: 2 V Capacity: 3000 Ah Converter Efficiency: 90% Lifetime: 10 years	Capital cost ($/unit): 1644 Replacement cost ($/unit): 1644 O&M cost ($/year): 10	[57,59]
Electrolyzer	Model: PEM Efficiency: 75% Capacity: 1 kW Lifetime: 50,000 h	Capital cost ($/kW): 3000 Replacement cost ($/kW): 2500 O&M cost: 1% of CAPEX	[70]
Hydrogen tank	Lifetime: 25 years	Capital cost ($/kg): 500 Replacement cost ($/kg): 500 O&M cost: 1% of CAPEX	[54,63]
Fuel cell	Model: PEM Efficiency: 59% Capacity: 1 kW Lifetime: 50,000 h	Capital cost ($/kW): 600 Replacement cost ($/kW): 300 O&M cost: 1% of CAPEX	[63,71]

The proposed system not only aims to reduce operational costs and energy losses but also pursues a broader set of techno-environmental objectives. Specifically, it seeks to minimize the LCOE, reduce overall CO_2 emissions, decrease the system's reliance on non-renewable generation — quantified in terms of operational hours — and simultaneously maximize the REF. These objectives are embedded within a dynamic, rule-based dispatch mechanism that allocates energy resources based on component availability, renewable generation forecasts, and storage SOC thresholds, as illustrated in Fig. 4.

The EMDS executes a sequential dispatch logic on an hourly basis. When renewable generation from rooftopPV, farm PV, and WTs is sufficient to meet the load, it is directly utilized. Any surplus is first directed toward charging the battery, constrained by available capacity and charge efficiency. If the battery is full, the remaining surplus is routed to a PEM electrolyzer for hydrogen production, provided the hydrogen storage tank is not full. Any residual excess is curtailed and recorded as dumped energy.

In scenarios where renewable power falls short of meeting the load, the EMDS initiates a staged discharging sequence. The battery is discharged within its minimum SOC threshold to reduce the deficit. If unmet demand persists, stored hydrogen is used via the fuel cell, subject to availability and conversion efficiency. If a gap remains even after battery and hydrogen discharges, the diesel generator is dispatched as a final resort, and the resulting emissions and fuel costs are accounted for. This structured strategy ensures optimal system reliability and energy autonomy while supporting multi-objective optimization across cost, emissions, and renewability.

2.3. Multi-objective optimization

The design of HRES constitutes a multi-objective, multi-constrained problem in which economic and environmental performance indicators must be balanced [61]. In this work, an A-NSGA-II is applied. This variant of the NSGA-II introduces adaptive mutation control, clustering-guided initialization, and feedback-driven evolutionary pressure, creating a tighter link between component sizing decisions and hourly dispatch modeling. The purpose is to identify system configurations that minimize four objectives: LCOE, cumulative CO_2 emissions, NRH, and a REF, the latter being defined as $1 - REF$ to fit the minimization framework. The evolutionary process is illustrated in Fig. 5, and the problem is formulated as Eq. (26) [74]:

$$\min F(x) = \{F_{\mathrm{LCOE}}, F_{\mathrm{CO_2}}, F_{\mathrm{NRH}}, F_{\mathrm{REF\_pen}}\} \tag{26}$$

where the decision vector is defined in Eq. (27):

$$x = (P_{\mathrm{PV}},\ P_{\mathrm{WT}},\ E_{\mathrm{batt}},\ P_{\mathrm{EL}},\ M_{H_2},\ P_{\mathrm{FC}},\ P_{\mathrm{DG}}) \tag{27}$$

subject to component capacity bounds,

$$0 \le P_{\mathrm{PV}}, P_{\mathrm{WT}}, E_{\mathrm{batt}}, P_{\mathrm{EL}}, M_{H_2}, P_{\mathrm{FC}}, P_{\mathrm{DG}} \le S_{\max} \tag{28}$$

dispatch feasibility constraints is defined in Eq. (29) (hourly power balance, rated capacities, SOC and hydrogen storage limits), and

$$0 \le NRH \le 8784, \qquad 0 \le REF \le 1 \tag{29}$$

Upper bounds $S_{\max}$ for each variable are derived from technical specifications and prior feasibility studies. The NRH term represents the number of hours the system requires non-renewable backup (diesel generation), while REF_{pen} penalizes designs with a low share of renewable supply. All objectives are evaluated using an integrated 8784-hour simulation of a representative meteorological year.

In this study, decision variables are treated as discrete sizing parameters to reflect modular deployment in practice. Each HRES component—PV arrays, WTs, battery storage, hydrogen infrastructure, and diesel backup—is represented in total installable capacity (kW, kWh, or kg), avoiding unit-by-unit enumeration while maintaining design flexibility. For example, WT capacity spans 2.1–8.4 MW (one to four 2.1 MW turbines), PV capacity starts at 5 kW in modular steps, and battery/hydrogen capacities are discretized for realistic integration.

Table 8 lists the lower and upper bounds defining the feasible region explored by the optimizer. The fuel cell capacity (P_{FC}) is fixed at 6875 kW, consistent with prior dispatch analysis indicating this as the optimal threshold for peak hydrogen-to-electricity conversion.

The configuration space resulting from this discretization is extremely large. Even with modular steps, the number of possible configurations exceeds 6.2 billion, rendering exhaustive search infeasible. The A-NSGA-II addresses this by using stratified sampling to initialize the population and dynamically adjusting search pressure based on feedback from objective performance. This enables convergence toward a diverse set of feasible Pareto-optimal solutions representing cost–emissions–reliability–renewable trade-offs.

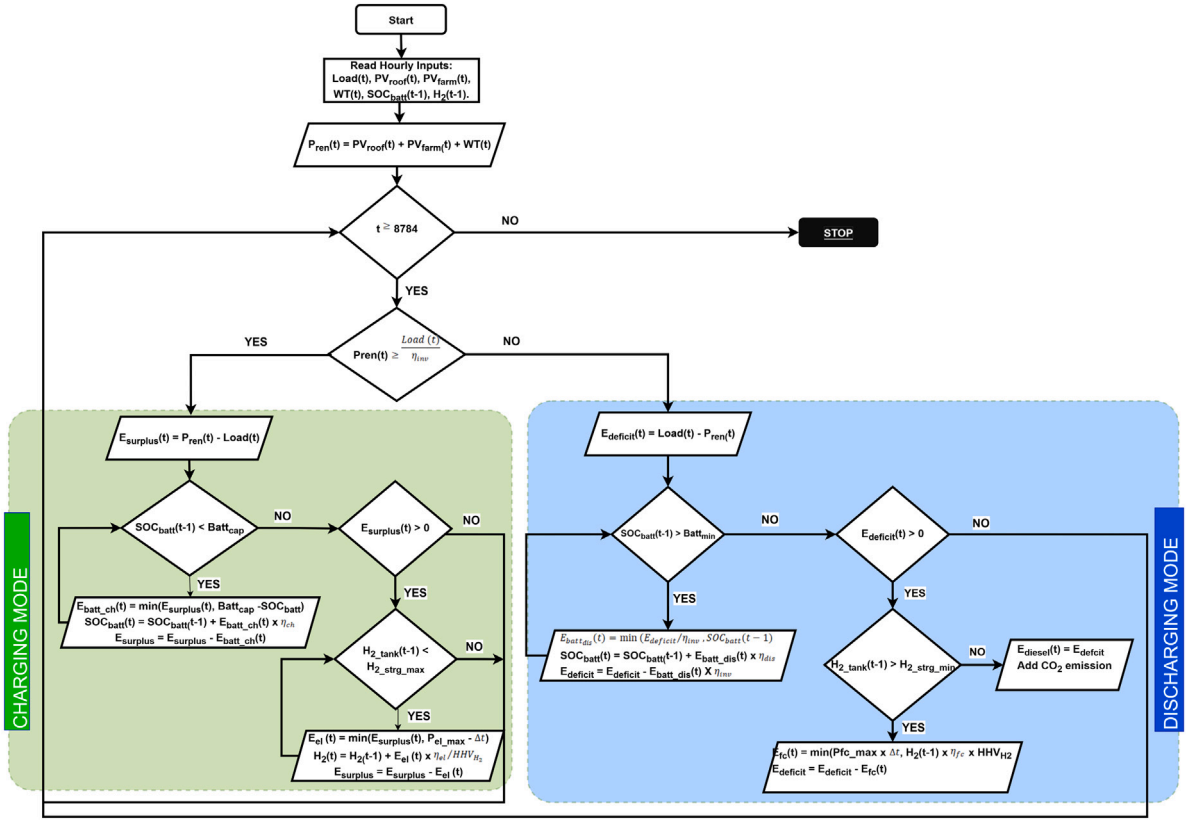

Fig. 4. Hourly dispatch strategy of the proposed HRES, illustrating renewable prioritization, storage utilization, and backup activation.

Table 8
Sizing bounds of HRES components used in the optimization model.

Component	Variable name	Unit	Lower bound	Upper bound
PV	P_{PV}	kW	5	70,000
WT	P_{WT}	kW	2100	8400
Battery storage	E_{batt}	kWh	100	178,894
Electrolyzer	P_{EL}	kW	2166	5200
Hydrogen tank	M_{H_2}	kg	1	1000
Fuel cell	P_{FC}	kW	6875	6875
Diesel generator	P_{DG}	kW	19,261	22,150

2.3.1. Objective functions

The optimization in this study considers four primary objectives: LCOE, total CO_2 emissions, NRH, and a renewable energy fraction penalty (REF_{pen}). These objectives collectively address the techno-economic and environmental trade-offs inherent in the sizing and dispatch of HRES. Each objective is evaluated over an 8784-hour annual simulation, fully capturing hourly variability in load demand, renewable resource availability, and storage state-of-charge.

The economic objective, LCOE, is derived from the NPC method with a fixed real discount rate of 7% over a 25-year lifetime. This approach accounts for capital, replacement, operation and maintenance, and fuel costs, with salvage value deducted, and normalizes the result by the total usable energy supplied. The environmental objective quantifies annual CO_2 emissions from diesel generator operation using an emission factor applied to hourly diesel output. Reliability is represented by NRH, defined as the total number of hours when renewable, battery, and hydrogen generation cannot fully meet demand, resulting in reliance on non-renewable backup. The REF is incorporated as a penalty function, REF_{pen}, which decreases as the share of renewable generation increases.

The mathematical definitions of these objectives, along with the relevant parameters, variables, and abbreviations, are presented in Table 9. These formulations ensure consistent integration into the NSGA-II minimization framework while enabling simultaneous evaluation of cost, emissions, reliability, and renewable energy share.

The REF is incorporated into the optimization as a penalty term, as defined in Eq. (30), to maintain compatibility with the minimization structure of the A-NSGA-II framework. This formulation avoids imposing a rigid feasibility constraint on renewable penetration and instead allows the evolutionary process to progressively favor system configurations with higher renewable contribution.

$$\mathrm{REF}_{pen} = 1 - \mathrm{REF}, \quad 0 \le \mathrm{REF} \le 1 \tag{30}$$

The use of a penalty-based REF objective reflects practical energy planning and policy contexts, where renewable targets are typically aspirational and incentive-driven rather than strict hard constraints. By treating REF as a continuous optimization objective, the proposed framework enables explicit exploration of trade-offs between renewable dominance, system cost, emissions, and reliability, while naturally steering solutions toward high-renewable regimes consistent with contemporary decarbonization policies.

2.3.2. Constraints

For any configuration produced by the optimization, technical feasibility and operational reliability must be preserved. This is achieved by enforcing a set of constraints during every hourly simulation step, rather than filtering infeasible solutions after the fact. Embedding these limits directly into the dispatch model ensures that the simulation reflects the actual behavior of the system under realistic conditions. Over the 8784-hour simulation horizon, these constraints govern energy conversion, storage utilization, and the prioritization of supply sources. Key operational thresholds—such as power balance, battery SOC, hydrogen storage capacity, and diesel generator limits—are thus respected at every timestep.

Table 9
Objective functions applied in NSGA-II optimization.

Objectives	Equations	Abbreviations
Economic objective	$LCOE = \frac{\sum_{i=1}^{n}\left[(CC_i + RC_i \cdot F(i)) \cdot CRF(i_r, R)\right] + C_{O\&M} + C_{fuel} - C_{salvage}}{E_{used}}$ $i_r = \frac{i_{nominal} - f_r}{1 + f_r}$ $CRF(i_r, R) = \frac{i_r(1+i_r)^R}{(1+i_r)^R - 1}$ $F(i) = \sum_{i=1}^{Y_i} \frac{1}{(1+i_r)^{L_{i,v}}}$	CC_i: Capital cost ($/kW) of component i RC_i: Replacement cost ($/kW) of component i $C_{O\&M}$: Annual operation and maintenance cost C_{fuel}: Diesel cost i_r: Real interest rate f_r: Inflation rate $i_{nominal}$: Nominal interest rate R: Project lifetime $F(i)$: Discounted replacement factor Y_i: Number of replacements L_i: Useful life of component i E_{used}: Total energy used (kWh)
Environmental objective	$CO_2 = \sum_{t=1}^{8784} P_{diesel}(t) \cdot EF_{diesel}$	$P_{diesel}(t)$: Diesel power at hour t EF_{diesel}: Emission factor (kg CO_2/kWh)
Reliability objective	$NRH = \sum_{t=1}^{8784} (P_{ren}(t) + P_{batt}(t) + P_{FC}(t) < P_{load}(t))$	NRH: Non-renewable hours $P_{ren}(t)$: PV + wind power $P_{batt}(t)$: Battery power $P_{FC}(t)$: Fuel cell power $P_{load}(t)$: Load demand
Renewable energy objective	$REF_{pen} = 1 - \frac{E_{renewable}}{E_{demand}}$	$E_{renewable}$: Energy from PV + wind E_{demand}: Total annual demand REF_{pen}: Penalty of low renewable share

2.3.2.1. Power balance constraint. At every hour t, the total electricity supplied from renewable generation and storage must equal the load. The dispatch sequence first uses PV and wind generation, followed by discharging the battery and operating the hydrogen fuel cell. If demand remains unmet, the diesel generator provides the deficit. This relationship is given in Eq. (31):

$$P_{\mathrm{PV}}(t) + P_{\mathrm{WT}}(t) + P_{\mathrm{batt}}(t) + P_{\mathrm{FC}}(t) + P_{\mathrm{DG}}(t) = P_{\mathrm{Load}}(t) \tag{31}$$

where $P_{\mathrm{Load}}(t)$ is the hourly demand. Any shortfall covered by the diesel generator contributes to the NRH objective.

2.3.2.2. Battery energy storage constraint. Battery operation is restricted by allowable SOC limits and maximum charge/discharge rates. The SOC progression follows Eq. (32):

$$E_{\mathrm{batt}}(t) = E_{\mathrm{batt}}(t-1) + \eta_{\mathrm{ch}} \cdot P_{\mathrm{ch}}(t) \cdot \Delta t - \frac{P_{\mathrm{dis}}(t) \cdot \Delta t}{\eta_{\mathrm{dis}}} \tag{32}$$

subject to:

$$E_{\mathrm{batt}}^{\min} \le E_{\mathrm{batt}}(t) \le E_{\mathrm{batt}}^{\max} \tag{33}$$

Here, $E_{\mathrm{batt}}^{\min}$ and $E_{\mathrm{batt}}^{\max}$ are determined by the rated capacity and depth of discharge, η_{ch} and η_{dis} are the charge and discharge efficiencies, and $P_{\mathrm{ch}}(t)$ and $P_{\mathrm{dis}}(t)$ represent charging and discharging power. Charging occurs only when excess renewable generation is available, whereas discharging is used to offset renewable shortfalls.

2.3.2.3. Hydrogen storage constraints. Hydrogen storage follows a mass balance linking electrolyzer production and fuel cell consumption as defined in Eq. (34):

$$M_{H_2}(t+1) = M_{H_2}(t) + \eta_{\mathrm{EL}} \cdot P_{\mathrm{EL}}(t) \cdot \Delta t - \frac{P_{\mathrm{FC}}(t) \cdot \Delta t}{\eta_{\mathrm{FC}}} \tag{34}$$

subject to:

$$0 \le M_{H_2}(t) \le M_{H_2}^{\max} \tag{35}$$

Here, $M_{H_2}(t)$ is the hydrogen mass (kg) at hour t, $P_{\mathrm{EL}}(t)$ and $P_{\mathrm{FC}}(t)$ are the electrolyzer input and fuel cell output power, and η_{EL} and η_{FC} are their efficiencies. Excess production is curtailed when the tank is full, while fuel cell operation stops when storage is depleted.

2.3.2.4. Diesel generator constraints. The diesel generator acts purely as a backup supply, operating only when renewables and storage are insufficient. Its operation is bounded by Eq. (36):

$$0 \le P_{\mathrm{DG}}(t) \le P_{\mathrm{DG}}^{\max} \tag{36}$$

Fuel usage is calculated from energy output using a fixed L/kWh factor, contributing directly to both LCOE and CO_2 emissions objectives. Dispatch is designed to avoid excessive cycling, favoring sustained operation when engaged.

2.3.2.5. Curtailment constraint. If renewable generation exceeds demand while battery and hydrogen storage are at maximum capacity, the surplus is curtailed and expressed in Eq. (37):

$$P_{\mathrm{curt}}(t) = \max\left[0,\ P_{\mathrm{PV}}(t) + P_{\mathrm{WT}}(t) - P_{\mathrm{Load}}(t) - P_{\mathrm{ch}}(t) - P_{\mathrm{EL}}(t)\right] \tag{37}$$

Curtailment does not affect the optimization objectives but is recorded for post-analysis.

2.3.2.6. Reliability constraint. Reliability is quantified through NRH, representing the hours when renewables and storage cannot meet demand without diesel support. A binary indicator $\delta(t)$ is defined for each hourly timestep using Eq. (38):

$$\delta(t) = \begin{cases} 1, & \text{if } P_{\mathrm{PV}}(t) + P_{\mathrm{WT}}(t) + P_{\mathrm{batt}}(t) + P_{\mathrm{FC}}(t) < P_{\mathrm{Load}}(t) \\ 0, & \text{otherwise} \end{cases} \tag{38}$$

The NRH value over the simulation period is then calculated using Eq. (39):

$$NRH = \sum_{t=1}^{8784} \delta(t) \tag{39}$$

This ensures that the reliability metric is evaluated consistently with the dispatch simulation and can be optimized directly alongside the other objectives.

2.4. Optimization algorithms configuration

This section describes the configuration and implementation details of the conventional NSGA-II and the proposed A-NSGA-II algorithms used in this study. It outlines the population structure, evolutionary operators, parameter settings, and termination criteria adopted to ensure fair comparison and reproducibility. Both algorithms were executed under identical population sizes and iteration limits, while the adaptive mechanisms introduced in A-NSGA-II are detailed in the subsequent subsections.

Table 10
Parameters used in the conventional NSGA-II.

Parameter	Value
Population size	50
Maximum generations	200
Selection mechanism	Binary tournament
Crossover rate	0.9
Crossover operator	Simulated Binary (SBX)
Mutation probability	0.05
Mutation operator	Polynomial
Termination criterion	Max generations

2.4.1. Conventional NSGA-II

The NSGA-II is one of the most widely used tools in multi-objective optimization. Its strength lies in balancing convergence and diversity through Pareto-ranking and crowding-distance mechanisms [75]. In energy research, and particularly in HRES, the method has proven especially useful for addressing competing economic, environmental, and reliability criteria. Studies ranging from rural microgrids to grid-connected designs confirm its suitability. For instance, [76] applied it for sizing PV–battery–diesel hybrids, while [77] employed it to evaluate renewable penetration in large-scale HRES. More recent studies reaffirm its relevance, positioning NSGA-II as the benchmark against which emerging evolutionary algorithms are compared [61].

Conventional NSGA-II is selected as the primary comparator in this study for three main reasons. First, NSGA-II remains one of the most widely adopted multi-objective evolutionary algorithms in HRES optimization literature, serving as a standard benchmark for evaluating new algorithmic developments [78,79]. Second, the proposed A-NSGA-II framework is an adaptive extension of the conventional NSGA-II structure; therefore, comparing against its non-adaptive baseline enables controlled assessment of the specific contributions introduced through dynamic mutation, clustering-based initialization, and feedback-driven search pressure. Third, maintaining the same underlying evolutionary operators ensures that performance differences can be attributed directly to adaptive mechanisms rather than to fundamentally different algorithmic paradigms.

In this study, NSGA-II is employed as the conventional optimization algorithm. Each candidate solution represents a complete configuration, combining PV, wind, battery, hydrogen, and diesel components. These are evaluated through dispatch simulation to assess four objectives: the LCOE, cumulative CO_2 emissions, NRH, and the renewable energy penalty. Offspring are generated using simulated binary crossover and polynomial mutation, while feasibility is enforced through embedded system-level constraints rather than post-processing checks.

To ensure clarity and reproducibility, the algorithmic parameters used in this conventional NSGA-II are summarized in Table 10. The table lists the key elements that govern evolutionary search—population size, number of generations, crossover and mutation operators, and termination conditions. These parameters define the reference configuration against which the A-NSGA-II variant will later be evaluated, highlighting how modifications in algorithmic design influence convergence behavior, solution diversity, and computational efficiency.

Although NSGA-II remains a powerful tool, it exhibits several weaknesses when applied to HRES optimization. Convergence speed is a major concern. Hybrid or adaptive approaches often achieve similar performance in far fewer iterations, whereas NSGA-II requires extended runs to stabilize [80]. Maintaining diversity in multi-objective contexts is another challenge. The crowding-distance mechanism struggles to distribute solutions evenly across the Pareto front, particularly when more than two objectives are involved [76]. Another limitation is the algorithm's reliance on fixed operator settings, which restricts its adaptability; static crossover and mutation rates fail to support broad exploration in early generations and fine-grained exploitation in later ones [77]. In addition, NSGA-II has difficulty coping with complex operational constraints such as SOC bounds and hydrogen mass balances, which introduce discontinuities that standard variation operators cannot manage effectively. These issues often result in premature convergence and reduced search efficiency, especially when compared with more recent evolutionary variants [19,61].

These limitations highlight the need for an adaptive approach. Such an approach must maintain population diversity and adjust search behavior in response to feedback from the optimization process. It must also be able to cope with the discontinuities that are inherent in HRES operation. This need motivates the A-NSGA-II, which is introduced in the following subsection.

2.4.2. A-NSGA-II:

Given the challenges of HRES optimization, a conventional NSGA-II run often struggles to maintain both convergence speed and solution diversity within such a vast and constraint-laden search space. To address these barriers, this study proposes an A-NSGA-II framework, which builds upon the conventional algorithm while introducing targeted modifications designed specifically for HRES. The novelty of the proposed approach can be summarized in five interconnected elements.

1. ***Knowledge-guided initialization.***
   The initialization process combines both global exploration and targeted exploitation. In the first generation, stratified random sampling ensures diversity and broad coverage of the decision space. For subsequent runs, the A-NSGA-II leverages knowledge from earlier results. K-means clustering is applied to the global Pareto archive, and cluster centroids seed the new population. To prevent premature convergence, about 10% of individuals are still injected randomly. This hybrid approach uses past knowledge while maintaining exploratory pressure, avoiding collapse into narrow local optima.
2. ***Adaptive polynomial mutation.***
   A central departure from the conventional NSGA-II is the introduction of a dynamic mutation operator. Rather than keeping the mutation probability fixed, it evolves across generations according to Eq. (40):

$$p_{\text{mut}}(g) = p_0 \cdot \left(1 - \frac{g}{G_{\max}}\right) \tag{40}$$

   where g is the current generation, $G_{\max}$ is the maximum generation, and p_0 is the initial mutation rate. To further enhance adaptability, the operator strength is adjusted using the feasibility ratio of the population in Eq. (41):

$$p_{\text{mut}}^{\text{eff}}(g) = p_{\text{mut}}(g) \cdot (1 - r_f) \tag{41}$$

   where r_f denotes the fraction of feasible solutions in the current population. When feasibility is low, the mutation rate is amplified to expand exploration. As feasibility improves, the operator naturally transitions into a refinement mode, strengthening exploitation. This dual adjustment allows the algorithm to cover the global search space effectively in early stages while focusing on local improvements in later generations.
3. ***Feasibility-aware local search.***
   Unlike the conventional NSGA-II, where local adjustments are absent, the A-NSGA-II framework introduces a selective refinement stage. Local search is triggered only for offspring that already satisfy dispatch feasibility, including power balance, battery SOC, and hydrogen storage dynamics. Adjustments are incremental—slight changes in PV, battery, or turbine sizing within allowable bounds. This ensures computational effort is not wasted on infeasible designs, while feasible candidates are finely tuned. The result is a mechanism that channels exploitation where it matters most, while leaving exploration to the global evolutionary operators.

Table 11
Comparison between conventional NSGA-II and the proposed A-NSGA-II framework.

Aspect	Conventional NSGA-II	Proposed A-NSGA-II
Initialization	Random population initialization	Stratified and clustering-guided initialization to enhance early diversity
Mutation strategy	Fixed mutation probability	Dynamic mutation adaptation based on evolutionary feedback
Crossover strategy	Fixed simulated binary crossover (SBX)	SBX retained with adaptive search pressure via mutation control
Local search	Not included	Selective local search applied to elite solutions
Constraint handling	Implicit penalty or feasibility checks	Embedded directly within hourly dispatch-coupled evaluation
Learning across runs	Independent runs with no memory	Cross-run learning using archived Pareto solutions
Diversity maintenance	Crowding distance only	Combined crowding distance and adaptive exploration mechanisms
Convergence control	Fixed parameters throughout evolution	Feedback-driven parameter adjustment to balance exploration and exploitation
Suitability for H-HRES	Limited adaptability under complex dispatch constraints	Specifically tailored for large-scale, dispatch-coupled H-HRES optimization

4. ***Dynamic feasibility checks.***
   At every generation, offspring are explicitly screened against dynamic bounds, represented in Eq. (42):

$$LCOE \le LCOE_{\max}, \qquad NRH \le NRH_{\max} \tag{42}$$

   Solutions that violate these conditions are either repaired through constraint-handling routines or discarded before entering the non-dominated archive. By embedding feasibility checks directly into the evolutionary loop, the search process continuously allocates effort toward regions that satisfy system requirements. This ensures exploration is not wasted in infeasible zones, while exploitation is intensified in areas that meet operational thresholds.
5. ***Global pareto archive with cross-run learning.***
   Finally, the algorithm introduces a system-level learning mechanism. A global non-dominated archive is maintained across runs, and before each new execution, the archive is merged and refined to guide population seeding. This cumulative memory allows knowledge to carry forward, unlike standard NSGA-II where each run starts from scratch. By integrating these results across independent executions, the optimizer sustains diversity, improves convergence speed, and avoids rediscovering solutions already explored. This cross-run learning extends the exploration–exploitation balance beyond a single evolutionary cycle, making the framework adaptive not only within generations but across the entire optimization campaign.

These five mechanisms transform NSGA-II from a static evolutionary optimizer into an adaptive, knowledge-driven, and problem-aware solver. The resulting framework learns both within generations and across independent runs, preserving diversity, focusing computational effort where it matters most, and navigating discontinuities in HRES dispatch modeling with greater reliability.

To clearly distinguish the proposed A-NSGA-II from the conventional NSGA-II, Table 11 summarizes the key algorithmic differences and adaptive mechanisms introduced in this study.

To provide transparency in implementation, the workflow of the proposed A-NSGA-II is illustrated in Fig. 5 and formally represented in Algorithm 3. The flowchart highlights the two central phases of the optimizer: the population evaluation phase, which embeds feasibility screening and dynamic constraint checks, and the evolutionary optimization phase, where adaptive operators, local search, and archive updates are performed iteratively. Algorithm 3 then provides the corresponding stepwise computational logic, ensuring reproducibility and making each adaptive element transparent in the optimization process. These two representations give both intuitive and technical clarity to the implementation of A-NSGA-II.

Algorithm 3 A-NSGA-II with K-Means reuse and feasibility-guided local search

Notation:
$\mathcal{B}$: bounds for decision variables
$G_{\max}$: maximum number of generations; N: population size
$\mathcal{A}$: Pareto archive; $\mathcal{A}_g$: global archive
$\mathcal{D}$: dataset (demand, irradiance, wind)
P: current population; x, y: individuals
F_x, F_y: objective vectors [LCOE, CO_2, NRH, REF penalty]
$\mathcal{F}$: ranked population; M: mating pool
C: crossover offspring; O: mutated offspring

Input: $\mathcal{B}$, $G_{\max}$, N
Output: $\mathcal{A}$
$G \leftarrow 1$
$D \leftarrow$ LOAD_DATA()
if $G = 1$ **then**
  $P \leftarrow$ INITIALIZE_POPULATION($\mathcal{B}$, N, method='stratified')
else
  $\mathcal{A}_g \leftarrow$ LOAD_GLOBAL_PARETO()
  $P \leftarrow$ KMEANS_GUIDED_INIT($\mathcal{A}_g$, N, explore_frac = 0.10)
end if
for each $x \in P$ **do**
  $F_x \leftarrow$ EVALUATE(x, D)
  if F_x.LCOE $\le$ LCOE$_{\max}$ **and** F_x.NRH $\le$ NRH$_{\max}$ **then**
    $\mathcal{A} \leftarrow \mathcal{A} \cup \{(x, F_x)\}$
  end if
end for
while $G \le G_{\max}$ **do**
  $\mathcal{F} \leftarrow$ FAST_NON_DOMINATED_SORT($\mathcal{A}$)
  $\mathcal{F} \leftarrow$ CROWDING_DISTANCE($\mathcal{F}$)
  $M \leftarrow$ TOURNAMENT_SELECTION($\mathcal{F}$)
  $C \leftarrow$ CROSSOVER(M, method='SBX')
  $O \leftarrow$ MUTATE(C, adaptive=True)
  for each $y \in O$ **do**
    $F_y \leftarrow$ EVALUATE(y, D)
    if F_y.LCOE $\le$ LCOE$_{\max}$ **and** F_y.NRH $\le$ NRH$_{\max}$ **then**
      $y' \leftarrow$ LOCAL_SEARCH(y, F_y)
      $\mathcal{A} \leftarrow$ UPDATE_ARCHIVE($\mathcal{A}, y'$)
    end if
  end for
  $P \leftarrow$ SELECT_NEXT_GENERATION($\mathcal{A}, N$)
  $G \leftarrow G + 1$
end while
SAVE_FINAL_RESULTS($\mathcal{A}$, logs=True)
return $\mathcal{A}$

Table 12 presents the parameter configuration for the proposed A-NSGA-II. While it retains the same population size, generation count, and crossover rate as the conventional (Table 8). It introduces adaptive mechanisms in mutation, initialization, and search guidance. These enhancements particularly clustering-guided seeding, feasibility-aware local search, and a global Pareto archive, constitute the main departures from the conventional NSGA-II. By embedding these adaptive

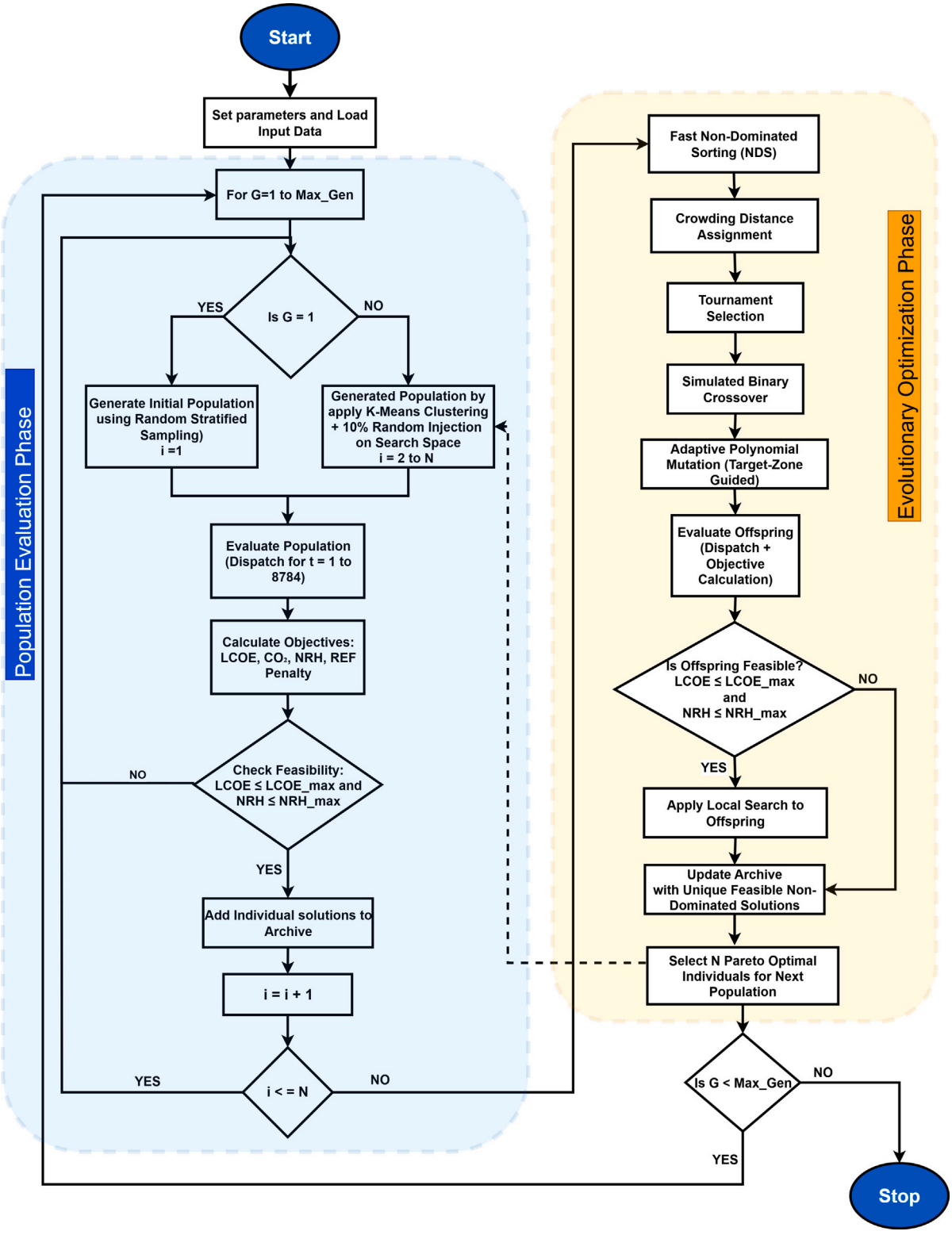

Fig. 5. Flowchart of Proposed A-NSGA-II.

Table 12
Parameters used in the proposed A-NSGA-II.

Parameter	Value	Parameter	Value
Population size	100	Crossover rate	0.9 (SBX)
Maximum generations	200	Mutation operator	Adaptive polynomial mutation
Selection mechanism	Tournament selection	Initialization	Stratified sampling (Gen 1); K-means clustering + 10% random injection
Feasibility mechanism	Dynamic checks on LCOE $\leq$ $LCOE_{max}$ and NRH $\leq$ NRH_{max}	Archive strategy	Global Pareto archive (cross-run learning)
Local search	Feasibility-guided adjustment of PV, battery, and turbine capacities	Termination criterion	Max generations

features into the evolutionary process, A-NSGA-II becomes responsive to the problem landscape rather than static across generations, reflecting its tailored design for HRES optimization.

With these modifications, A-NSGA-II is not simply a parameter-tuned variant of the conventional optimizer. It is a structured enhancement that integrates adaptive operators, feasibility guidance, and cross-run learning into a single coherent framework. The following section evaluates its performance against the conventional NSGA-II. This comparison highlights how the adaptive elements improve convergence behavior, sustain diversity across the Pareto front, and increase the feasibility of solutions in HRES optimization.

2.5. Performance metrics

The performance of multi-objective optimization in HRES cannot be adequately judged by visual Pareto plots alone. Quantitative performance metrics are essential to evaluate both the quality of the obtained solutions and the behavior of the underlying algorithm [81]. In this study, three well-established metrics are employed: hypervolume, spacing, and convergence. Together, they capture complementary aspects of solution quality, namely coverage, diversity, and proximity to optimality, which ensures a balanced evaluation of NSGA-II and A-NSGA-II in the HRES context.

2.5.1. Hypervolume

The hypervolume indicator is one of the most established measures in MOEA. It provides a single scalar value that simultaneously captures two critical properties of a solution set: convergence toward the Pareto-optimal front and diversity across trade-off regions [82]. Hypervolume quantifies the portion of the objective space that is dominated by a given Pareto front when measured against a fixed reference point. A higher hypervolume value therefore implies that the algorithm has produced solutions that are both close to the ideal front and well spread across the range of objectives [83].

In the context of HRES optimization, hypervolume holds particular importance. System planners often face competing objectives, such as minimizing LCOE while reducing CO_2 emissions or limiting reliance on non-renewable generation. This makes hypervolume highly valuable for evaluating algorithms intended to support energy policy and investment decisions.

Formally, if P is the set of non-dominated solutions and $r = (r_1, r_2, \ldots, r_m)$ is a reference point in the objective space, the hypervolume is calculated using Eq. (43) [84]:

$$HV(P) = \lambda\left(\bigcup_{x\in P}\left[f_1(x), r_1\right] \times \cdots \times \left[f_m(x), r_m\right]\right) \tag{43}$$

where λ denotes the Lebesgue measure and m the number of objectives. This formulation treats each solution as defining a hyper-rectangle bounded by the reference point, and the union of these rectangles forms the dominated region.

2.5.2. Spacing metric

The spacing metric measures how evenly solutions are distributed along the Pareto front. Unlike hypervolume, which captures both convergence and coverage, spacing isolates diversity by measuring how evenly solutions are spread [85]. A lower spacing value reflects a more balanced spread of solutions, while a higher value points to clustering or gaps.

The metric is calculated using Eq. (44) [85]:

$$S = \sqrt{\frac{1}{|P|-1}\sum_{i=1}^{|P|}(d_i - \bar{d})^2} \tag{44}$$

where d_i is the minimum distance from solution i to its nearest neighbor in objective space, and $\bar{d}$ is the mean of all distances. It penalizes irregularity, rewarding Pareto fronts where solutions are evenly distributed.

In the context of HRES, spacing plays a critical role. Energy planning requires decisions across multiple, often conflicting objectives—such as cost, CO_2 emissions, system reliability, and REF [86]. If solutions are unevenly distributed, some trade-off regions may remain unexplored, limiting the flexibility available to planners. Prior studies such as [61,87,88], have emphasized the importance of diversity metrics in energy system optimization to ensure that all policy-relevant strategies, from low-cost to low-carbon extremes.

2.5.3. Convergence score

Convergence assesses how closely the obtained Pareto front approaches the true or reference front. While diversity ensures that decision-makers see a range of alternatives, convergence ensures that these alternatives are not only varied but also globally efficient [83]. A front with poor convergence may appear diverse yet still represent suboptimal designs.

In formal terms, convergence is measured as the average Euclidean distance between solutions in the obtained set P and their nearest neighbors on the reference Pareto front P^*, expressed in Eq. (45):

$$C = \frac{1}{|P|}\sum_{i=1}^{|P|}\min_{y\in P^*}\left\|f_1(x_i) - f(y)\right\| \tag{45}$$

A lower value of C indicates that the solution set lies closer to the global trade-off boundary.

This definition is widely adopted in MOEA and has been applied across engineering and energy system studies [83,89]. A lower value of C indicates that the solution set lies closer to the global trade-off boundary.

For HRES, strong convergence is essential. Recommendations such as the sizing of storage, the share of renewable energy, or the level of backup generation must be not only feasible but also close to the global optimum. Otherwise, planners risk committing to configurations that are technically workable but economically or environmentally inferior [42,90]. In this way, convergence acts as a safeguard, ensuring that the diversity captured by spacing and the coverage quantified by hypervolume are anchored in true system efficiency. These three metrics ensures that evaluation is both rigorous and meaningful. Hypervolume reflects overall coverage of the objective space, spacing secures a balanced spread of trade-offs, and convergence confirms proximity to the global frontier. Together, they form a concise yet robust framework for judging the effectiveness of multi-objective optimization algorithm variants in HRES optimization

Table 13
Benchmark functions employed for performance evaluation.

Name	Function	Dim	Range	Reference
Sphere4	$f(x) = \sum_{i=1}^{n} x_i^2$	4	$[-100, 100]^n$	[97]
Rastrigin4	$f(x) = 10n + \sum_{i=1}^{n} \left(x_i^2 - 10\cos(2\pi x_i)\right)$	4	$[-5.12, 5.12]^n$	[97]
Griewank4	$f(x) = 1 + \frac{1}{4000}\sum_{i=1}^{n} x_i^2 - \prod_{i=1}^{n} \cos\left(\frac{x_i}{\sqrt{i}}\right)$	4	$[-600, 600]^n$	[93]
Schaffer F7	$f(x) = \left[\frac{1}{n-1}\sum_{i=1}^{n-1}\left(\sqrt{s_i} + \sqrt{s_i}\sin^2\left(50 s_i^{0.2}\right)\right)\right]^2$	4	$[-100, 100]^n$	[91]
CEC2021-F1	$f(x) = \sum_{i=1}^{n}(x_i - o_i)^2$	4	$[-100, 100]^n$	[95]
CEC2021-F4	$f(x) = \sum_{k=1}^{K} \omega_k f_k\left(T_k(x - o_k)\right)$	4	$[-100, 100]^n$	[95]

2.6. Benchmark problem setup

To evaluate the robustness of the conventional and A-NSGA-II algorithms, a suite of well-established benchmark functions was employed. These functions are drawn from recent multi-objective optimization literature [91–94]. They also include functions from international competitions such as the Commission of the European Communities (CEC) 2021 benchmark set [95] and classical scalable functions including Sphere, Rastrigin, Griewank, and Schaffer F7 [96]. Each function reflects a specific landscape property that stresses evolutionary search: separability or non-separability, unimodality or multimodality, and smooth or discontinuous Pareto fronts. By combining classical test functions such as Schaffer and Griewank with more recent designs such as CEC2021-F1 and F4, the suite provides a balanced evaluation platform.

The chosen functions cover both analytical and competition-based benchmarks. Classical functions are useful for conventional performance on convex or multimodal surfaces. In contrast, the CEC and Sphere, Rastrigin, Griewank, and Schaffer F7 benchmarks add higher-dimensional challenges and discontinuities that resemble real-world problems [95,96]. For consistency, all functions are considered in a four-objective setting. Their dimensionality and decision space bounds follow standard practice. The mathematical definitions are provided in Table 13.

It should be noted that the feasibility-aware local search mechanism is context-dependent. In the H-HRES application, feasibility evaluation involves dispatch constraints, NRH limits, and system-balance requirements. However, for the mathematical benchmark functions listed in Table 13, no physical constraints are imposed beyond predefined variable bounds. Accordingly, the feasibility component of the local search reduces to bound enforcement, while the refinement mechanism focuses solely on objective-space improvement within the admissible search region.

These six benchmarks form a comprehensive testbed. The simpler cases test convergence speed and baseline stability. Multimodal and hybrid problems assess resilience against local optima, while the high-dimensional and discontinuous challenges evaluate robustness. This mix ensures that both the conventional NSGA-II and A-NSGA-II evaluated under rigorous and widely accepted standards.

3. Results

All optimization experiments were conducted on a personal computing system featuring an Intel® Core™ i5-6300U CPU with a clock speed of 2.40–2.50 GHz and 16 GB of RAM, operating within a 64-bit Windows environment. The optimization framework was developed using Python 3.11 and implemented via the Spyder IDE. This computational setup provided adequate resources for executing the multi-objective NSGA-II and A-NSGA-II simulations, including dispatch modeling and performance metric evaluation, without necessitating high-performance computing facilities.

Table 14
Heuristic-based baseline configuration (non-optimized reference system).

Component	Capacity	Assumption basis
PV capacity	22,366 kW	~50% of peak demand with irradiance adjustment
Wind turbines	2 units (~2.1 MW each)	Fixed (representative small-scale integration)
Battery storage	42,000 kWh	~30% of average daily demand
H_2 storage	300 kg	Fixed (conservative tank size)
Electrolyzer	3500 kW	Fixed (typical small-scale setup)
Fuel cell	6875 kW	Fixed (sized for backup)
Diesel generator	20,000 kW	Fixed (conservative emergency backup capacity)

3.1. Heuristic-based baseline configuration (non-optimized reference system)

Before applying evolutionary optimization, a heuristic-based static configuration was evaluated to establish a non-optimized reference system. This configuration was constructed using conventional engineering rules of thumb rather than evolutionary search and therefore does not represent the outcome of the conventional NSGA-II algorithm. Its purpose is to illustrate the limitations of heuristic component sizing prior to formal multi-objective optimization.

Component capacities were selected using simplified design assumptions. For example, PV capacity was set to approximately 50% of peak demand with irradiance adjustment, and battery storage was sized to cover roughly 30% of average daily consumption. Hydrogen storage, electrolyzer capacity, fuel cell rating, and diesel generator capacity were chosen to reflect plausible small-scale integration under local demand conditions. The resulting system layout is presented in Table 14.

The performance of this heuristic baseline configuration is summarized in Table 15. The results highlight the inherent limitations of static sizing in balancing economic, environmental, and reliability objectives. The LCOE reaches 2.46 AUD/kWh, which remains high for grid-scale adoption. Annual CO_2 emissions total 921,119 kg, with more than 1000 h of reliance on diesel backup. The REF remains limited to 75.3%, leaving nearly one quarter of demand dependent on fossil-based sources. Diesel generation contributes 3.68 GWh annually, significantly increasing both emissions and operational cost. Hydrogen operation is also inefficient, with over 1.06 million kilograms consumed compared with only 46,378 kg produced, leading to a high Levelized Cost of Hydrogen (LCOH) of 8.14 AUD/kg. These outcomes demonstrate that while the system is technically functional, heuristic sizing results in elevated cost, heavy fossil reliance, and suboptimal renewable integration.

These results underline the necessity of systematic multi-objective optimization. In the following subsections, the term “Conventional

Table 15
Performance results of the heuristic baseline configuration.

Metric	Result
LCOE (AUD/kWh)	2.46
CO_2 emissions (kg)	921,119
NRH	1059
REF	0.753 (75.3%)
REF penalty	0.247
Diesel used (kWh)	3,684,475
H_2 produced (kg)	46,378
H_2 used (kg)	1,060,254
LCOH (AUD/kg)	8.14

NSGA-II" refers specifically to the fully optimized evolutionary solution obtained using the standard NSGA-II algorithm, and should be clearly distinguished from the heuristic baseline presented above.

3.2. Multi-objective optimization outcomes

This section presents the optimization results obtained from the conventional NSGA-II and the proposed A-NSGA-II frameworks. The analysis focuses on Pareto front characteristics, trade-off behavior among the four defined objectives, and comparative performance across solution quality metrics. The results highlight differences in convergence, diversity preservation, and system design implications emerging from the two optimization strategies.

3.2.1. Pareto front characterization and trade-off visualization

The optimization generated distinct Pareto fronts for the conventional NSGA-II and the A-NSGA-II. Both were evaluated across four objectives: LCOE, CO_2 emissions, NRH, and REF penalty. Fig. 6 illustrates the results in three dimensions, with the REF penalty represented by the color scale. This format highlights the shape of the trade-off surface and the distribution of feasible solutions.

The conventional NSGA-II, as shown in Fig. 6(a), produced a wide spread of solutions. CO_2 emissions extend beyond 3.5, while non-renewable reliance exceeds 4000 h in some cases. These extreme outcomes indicate weak sustainability. The REF penalty also rises to 0.40, suggesting that many solutions provide only modest RE contributions. The distribution is stretched and scattered, with gaps in the frontier, reflecting weaker balance across objectives. In contrast, the A-NSGA-II, as shown in Fig. 6(b), reveals a much tighter and more compact front. The solutions are concentrated in the region of low CO_2 emissions and reduced NRHs, with most values below 2000. The REF penalty remains consistently low, never exceeding 0.25, pointing to stronger renewable integration. Trade-offs between LCOE and emissions are smoother, and the frontier is continuous, demonstrating improved convergence and coverage. The comparison shows a clear advantage for the A-NSGA-II. While the NSGA-II algorithm explores more widely, it often converges to extreme or impractical designs. The A-NSGA-II algorithm, on the other hand, delivers a denser set of solutions that balance cost, emissions, and reliability more effectively. For decision-makers, this provides a more practical set of alternatives that avoid the poor-quality trade-offs of the conventional approach.

These findings, as summarized in Table 16, compare the main features of the pareto fronts and present A-NSGA-II algorithm as the stronger optimizer. It consistently identifies fronts with lower non-renewable dependency, reduced REF penalties, and tighter balance among objectives. The following subsections build on this foundation, moving from the overall front to the selection of rank-based and policy-guided solutions.

Table 16
Comparative features of pareto fronts from conventional NSGA-II and A-NSGA-II.

Feature	Conventional NSGA-II	A-NSGA-II
CO_2 emissions range	Up to ~3.5 (high-emission solutions)	Mostly below ~1.6 (low-emission focus)
NRH	Often above 4000	Concentrated below 2000
REF penalty	Up to 0.40 (poor renewable share)	Below 0.25 (improved renewable fraction)
Distribution	Wide and scattered, with visible gaps	Compact, continuous, and well-balanced
Convergence pattern	Uneven, weaker trade-off surface	Smoother, tighter trade-off structure

3.2.2. Optimal solution identification: Rank-based approach

A sensitivity-informed multi-objective evaluation was applied to identify the most balanced solutions from the global Pareto sets of both algorithms. Configurations were first filtered using feasibility thresholds (LCOE $\leq$ 6.0 AUD/kWh and NRHs $\leq$ 500 per year) to ensure economic and operational realism. All objectives were normalized with min–max scaling, and more than 100 weight vectors were generated with a step size of 0.1 and a maximum of 0.7 for any single objective. For each weight set, the best-performing solution was extracted, and rank aggregation was applied. Each solution was ranked across all four objectives, and the configuration with the lowest cumulative rank was selected as the optimal trade-off.

The result of this comparison is presented in Table 17. Both algorithms converge on similar capacities for wind and fuel cells, indicating stable design choices across optimization strategies. However, important distinctions emerge in other components. The A-NSGA-II algorithm allocates more storage, with battery capacity that increases from 105,385 to 112,378 kWh and hydrogen storage increasing more than twofold (1000 kg compared with 386 kg). It also employs a slightly larger electrolyzer, enhancing renewable-to-hydrogen conversion. These adjustments reduce diesel reliance, as indicated by the smaller generator size and the halving of non-renewable operating hours.

Performance indicators reinforce the advantage of the A-NSGA-II. It achieves a lower LCOE (5.81 AUD/kWh versus 5.92 AUD/kWh) while simultaneously cutting annual CO_2 emissions almost in half (51,823 kg compared to 93,979 kg). The REF improves from 82.3% to 88.4%, confirming higher penetration of renewable supply. Most notably, non-renewable reliance falls from 103 to 53 h per year, representing a near 50% reduction, demonstrating higher resilience and reduced fossil dependence.

Overall, the A-NSGA-II demonstrates clear superiority across economic, environmental, and reliability dimensions. Its emphasis on enhanced storage capacity and renewable conversion directly translates into lower system cost, deeper decarbonization, and greater resilience against non-renewable reliance. These outcomes confirm that the A-NSGA-II algorithm can capture more balanced trade-offs compared with the conventional NSGA-II.

To illustrate these improvements in real operation, Fig. 7 presents the A-NSGA-II dispatch profile for a representative two-day period (13–14 June 2024). Renewable generation supplies the bulk of daytime demand, with surpluses allocated to battery charging and hydrogen production. During evening and early morning hours, the system strategically discharges the battery to cover demand peaks, thereby substantially reducing diesel reliance. Hydrogen production is activated in periods of high renewable availability, while its discharge remains limited in this window, underscoring its function as a long-term balancing vector rather than a short-term provider. Importantly, certain hours such as hour 19 show no dispatch activity, indicating that demand was

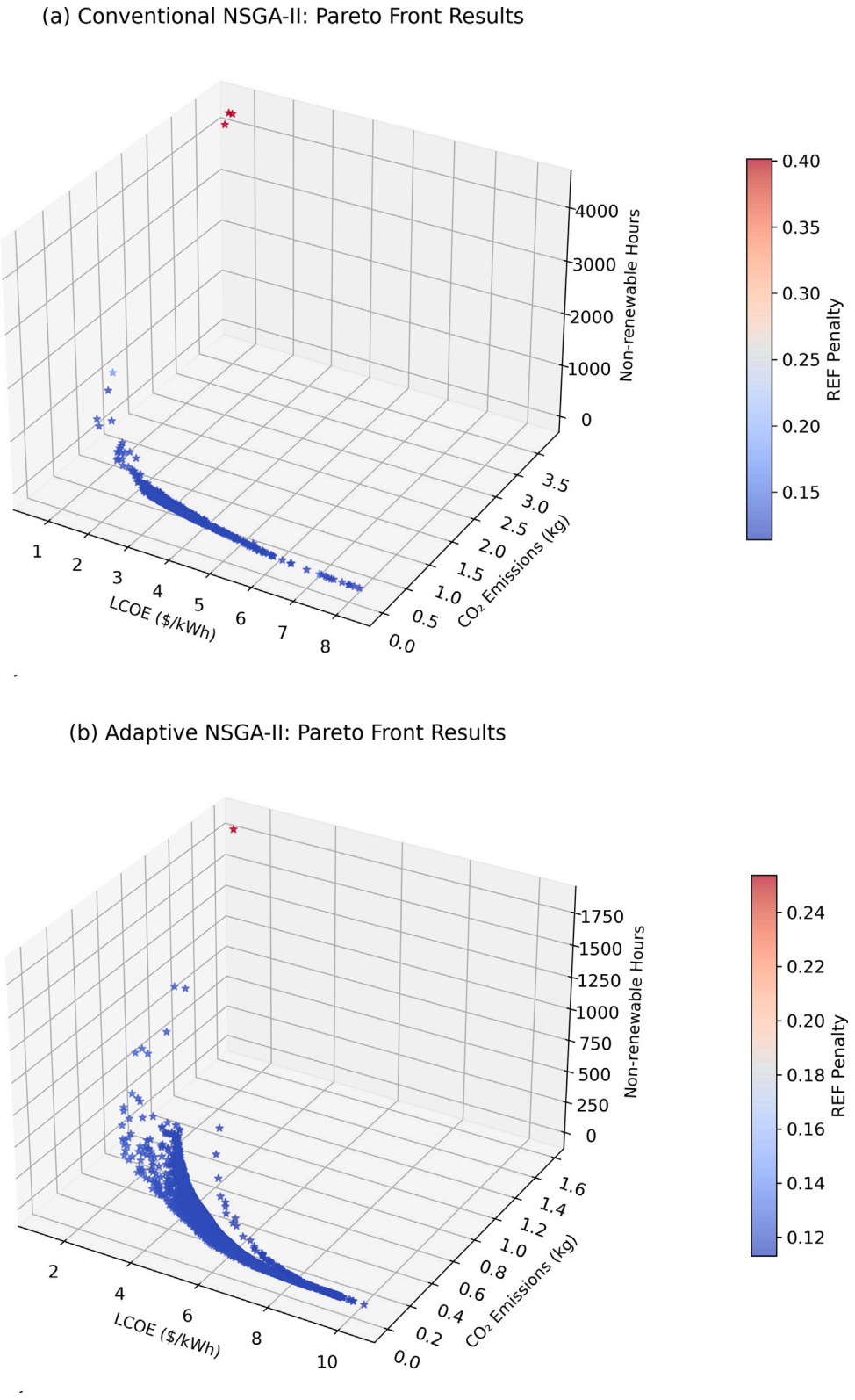

Fig. 6. Pareto fronts for the hybrid system optimization showing LCOE, CO_2 emissions, and NRH, with REF penalty as color scale: (a) conventional NSGA-II, (b) A-NSGA-II. (For interpretation of the references to color in this figure legend, the reader is referred to the web version of this article.)

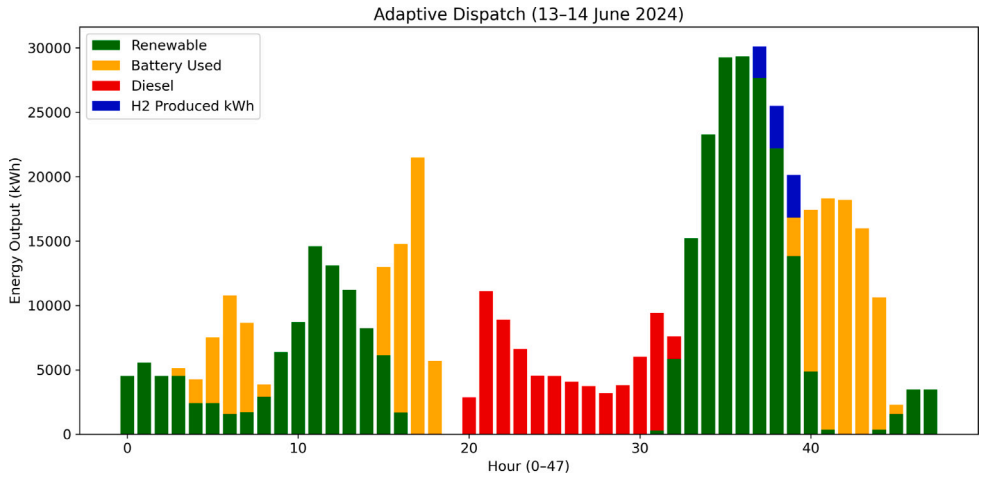

Fig. 7. Hourly dispatch profile of the adaptive NSGA-II optimal solution for 13–14 June 2024, showing contributions from renewable generation, battery discharge, diesel backup, and hydrogen production.

Table 17
Comparison of rank-based optimal solutions from conventional NSGA-II and A-NSGA-II.

Component/Metric	Conventional NSGA-II	A-NSGA-II	Interpretation
PV capacity (kW)	47,121	46,518	A-NSGA-II requires slightly less PV while still improving outcomes, suggesting better overall system synergy
WT capacity (MW)	8.4	8.4	Identical wind integration; not a distinguishing factor
Battery storage (kWh)	105,385	112,378	A-NSGA-II invests more in battery storage, enhancing short-term renewable utilization
Hydrogen storage (kg)	386	1000	A-NSGA-II emphasizes hydrogen, providing stronger long-duration backup capacity
Fuel cell capacity (kW)	6875	6875	Same in both cases, ensuring consistent hydrogen-to-electricity conversion capability
Electrolyzer capacity (kW)	4798	5161	A-NSGA-II opts for a larger electrolyzer, improving renewable-to-hydrogen conversion
Diesel generator capacity (kW)	20,882	20,724	Slightly reduced diesel reliance in Adaptive, consistent with reduced backup fossil hours
LCOE (AUD/kWh)	5.9169	5.8083	A-NSGA-II achieves lower cost, confirming superior economic efficiency
CO_2 emissions (kg/year)	93,979.06	51,822.53	Significant emissions reduction in A-NSGA-II, supporting sustainability goals
REF	82.34%	88.41%	A-NSGA-II improves renewable penetration and grid independence
NRH (h/year)	103	53	A-NSGA-II cuts reliance on non-renewables nearly in half, enhancing resilience

exactly met by renewable output without surplus or deficit, thereby avoiding unnecessary cycling of storage or backup systems.

Diesel generation is confined to residual hours of renewable scarcity, most notably during the first night, confirming its role as a last-resort backup rather than a primary energy source. It is important to emphasize that diesel generator capacity is determined by peak contingency requirements rather than annual operating hours alone. Although the A-NSGA-II configuration utilizes the diesel generator for only 53 h per year, its rated capacity remains above 20 MW to ensure supply adequacy during rare but critical high-demand and low-renewable events. In such scenarios, instantaneous peak load must be satisfied without violating reliability constraints. Therefore, generator sizing reflects worst-case power balance requirements rather than average energy contribution. The low utilization rate indicates effective renewable–storage coordination, while the retained capacity serves as a reliability reserve to guarantee system security under extreme operating conditions.

This operational sequence reflects the quantitative improvements observed in Table 17, where fossil fuel dependence and CO_2 emissions were significantly reduced relative to the conventional NSGA-II optimization. The result demonstrates the effectiveness of the A-NSGA-II optimization in coordinating multiple energy vectors to ensure reliability while advancing sustainability objectives.

The following subsection therefore extends the analysis by presenting weighted top-3 solutions under varying preference regimes, providing a broader basis for decision support.

3.2.3. *Weighted top-3 solutions for policy-guided decision support*

Energy planning decisions rarely rest on a single objective. They emerge from trade-offs where cost, emissions, reliability, and renewable integration are weighted differently by stakeholders. To address this reality, a policy-guided weighting vector was applied:

- LCOE (0.5) – Prioritizing economic viability,
- NRHs (0.3) – Encouraging reduced fossil fuel reliance,
- CO_2 emissions (0.1) – Capturing environmental externalities,
- REF penalty (0.1) – Ensuring strong renewable integration.

This reflects procurement practices where cost minimization dominates, yet sustainability remains a significant concern.

The selected weighting vector is scenario-based and does not originate from formal expert elicitation. Instead, it represents an illustrative procurement-oriented decision perspective commonly observed in practical energy planning contexts, where economic viability typically dominates initial screening, followed by reliability and sustainability considerations [98]. The purpose of this weighting structure is not to prescribe a single normative preference set, but to demonstrate how Pareto-optimal configurations respond to a realistic stakeholder priority scenario. Additional robustness to alternative weight regimes is examined in Section 3.2.4 through sensitivity analysis.

From the Pareto front sets, the three top distinct solutions per algorithm (NSGA-II, A-NSGA-II) were extracted based on their weighted

Table 18
Comparison of weighted top-3 solutions from conventional NSGA-II and A-NSGA-II.

Rank	Optimizer	PV (kW)	WTs	Battery (kWh)	H_2 (kg)	Fuel cell (kW)	Electrolyzer (kW)	Diesel Gen (kW)	LCOE (AUD/kWh)	NRH (h)	CO_2 (kg)	REF (%)
1	Conventional	2800	4	16,232	263	6875	3864	21,853	0.9583	803	742,545.52	81.36
	Adaptive	16,617	4	35,744	937	6875	4151	20,021	2.1434	323	338,087.55	87.91
2	Conventional	6022	4	39,644	278	6875	3631	22,131	1.8173	587	461,690.17	84.52
	Adaptive	12,275	4	29,604	452	6875	4649	20,744	1.7702	457	453,433.89	87.78
3	Conventional	11,002	4	3061	194	6875	2330	19,499	0.9078	1123	1,012,836.19	78.73
	Adaptive	17,002	4	62,571	958	6875	5200	21,486	2.9948	216	228,749.24	87.92

composite scores. A diversity filter was used to avoid clustering and to ensure coverage of different regions of the pareto front. This yielded a set of high-quality, policy-aligned solutions that provide decision-makers with a shortlist rather than a single compromise. Fig. 8(a) and (b) show the placement of the top-3 weighted solutions against the global pareto fronts, and Table 18 reports their component configurations and performance indicators.

The conventional NSGA-II algorithm identifies extremely low-cost designs, with LCOE values below 1 AUD/kWh. Yet these come with heavy penalties. CO_2 emissions exceed 700,000 kg and non-renewable reliance is above 800 h, rising to more than 1000 h in the third-ranked case. Renewable penetration also drops below 80%. These outcomes underline the limitations of the conventional NSGA-II, that is low cost is achieved only by sacrificing sustainability and resilience.

The A-NSGA-II algorithm presents a more balanced portfolio. LCOE values range between 1.77 and 2.99 AUD/kWh, modestly higher than those of the conventional NSGA-II algorithm, as shown in Table 18. However, CO_2 emissions are reduced by more than 50%, with the best solution emitting only 228,749 kg. NRH fall dramatically, reaching as low as 216. REF consistently exceeds 87.7%, showing strong renewable integration across all A-NSGA-II candidates. Larger hydrogen and battery capacities provide the technical foundation for these improvements, enabling deeper decarbonization while maintaining system reliability.

Overall, the A-NSGA-II delivers superior policy-guided solutions. It avoids the extreme, high-emission trade-offs of the conventional NSGA-II algorithm and instead offers renewable-rich designs that balance cost, emissions, and reliability. For decision-makers, this portfolio represents not only technically feasible systems, but also practical strategies aligned with long-term decarbonization and energy security. The next subsection extends this evaluation by examining robustness across a wider range of weighting regimes through sensitivity analysis.

3.2.4. Sensitivity analysis of optimization robustness under policy weight variations

Energy system planning requires solutions that remain robust under shifting policy priorities. To evaluate this robustness, both the conventional NSGA-II and A-NSGA-II were subjected to a comprehensive sensitivity analysis across more than seventy distinct policy weighting scenarios. Each scenario reflects a plausible decision context. In some cases, cost dominates, while in others emissions, reliability, or renewable penetration are given more weight. This approach allows the analysis to capture the full diversity of trade-offs seen in real-world planning.

The ranking of solutions was based on a composite weighted score. For a solution i, under a policy vector $w = (\omega_1, \omega_2, \omega_3, \omega_4)$, the score is defined in Eq. (46):

$$S_i(w) = \sum_{j=1}^{4} \omega_j \hat{f}_{j,i} \tag{46}$$

where $\hat{f}_{j,i}$ are the normalized values of the four objectives: LCOE, NRH, CO_2 emissions, and REF penalty. The policy weights satisfy $\sum_{j=1}^{4} \omega_j = 1$.

For each weight vector, the top-1 solution was selected using a ranking operator in Eq. (47):

$$\pi(w) = \arg\min_{i \in P} S_i(w) \tag{47}$$

where P denotes the feasible pareto-optimal set. This procedure yields the best-performing solution under a given preference regime. The weight space w was explored systematically using a constrained grid search as defined in Eq. (48):

$$w = \left\{ w \in [0,1]^2 \;\middle|\; \sum_{j=1}^{4} \omega_j = 1, \;\; \omega_j \in \{0.1, 0.2, \ldots, 0.7\} \right\} \tag{48}$$

This resulted in 80 distinct weighting vectors, each producing one candidate "best" configuration per algorithm. In total, 80 solutions were assessed for both conventional NSGA-II and A-NSGA-II frameworks.

Fig. 9(a–d) show the sensitivity of each individual objective to policy weighting. The conventional NSGA-II produces strong fluctuations. LCOE values sometimes fall below 4 AUD/kWh, but these low-cost solutions coincide with spikes in CO_2 emissions and non-renewable reliance. In several weight sets, CO_2 emissions exceed 400,000 kg/year and diesel use rises above 300 h. REF penalty also fluctuates more widely, indicating weaker stability in renewable penetration. In contrast, A-NSGA-II remains smoother across the full spectrum of weights. Its cost profile is narrower, emissions stay consistently lower, and NRH rarely deviate from low-dependency regions. REF values remain close to high-renewable configurations even when renewable integration is not explicitly prioritized.

The trade-off perspective in Fig. 10 (a–c) strengthens these observations. In the LCOE–CO_2 plane, conventional NSGA-II solutions scatter widely. Very low-cost designs appear only when emissions rise well above 300,000 kg. A-NSGA-II solutions instead form a more compact curve, where moderate cost increases are accompanied by substantial emission reductions. A similar trend emerges in the LCOE–NRH relationship. Conventional NSGA-II solutions extend above 300 h of fossil dependence, while adaptive outcomes cluster tightly below 200 h. Finally, in the LCOE–REF space, NSGA-II maintains renewable fractions close to 88%, whereas conventional NSGA-II solutions frequently dip below this threshold under cost-focused weights.

Taken together, the A-NSGA-II demonstrates clear robustness under changing policy priorities. It avoids the unstable extremes of the conventional NSGA-II algorithm and delivers stable, renewable-aligned outcomes even when objectives are weighted differently. For decision-makers, this robustness is particularly important: it ensures that energy system designs remain technically viable and consistent with decarbonization goals, regardless of how policy emphasis shifts over time.

Beyond the objective-level comparisons, it is important to visualize how the optimized system functions dynamically under real-world demand conditions. Fig. 11 illustrates the weekly energy flow of the A-NSGA-II optimal configuration. Renewable generation (PV and wind) provides the primary supply, while batteries and hydrogen act as balancing buffers. Surplus generation is directed into hydrogen production, which later complements battery discharge during evening peaks. Diesel operates only as a minimal backup in residual deficit hours. The inset highlights short-term balancing across consecutive hours, showing how storage and renewables interact seamlessly to meet demand.

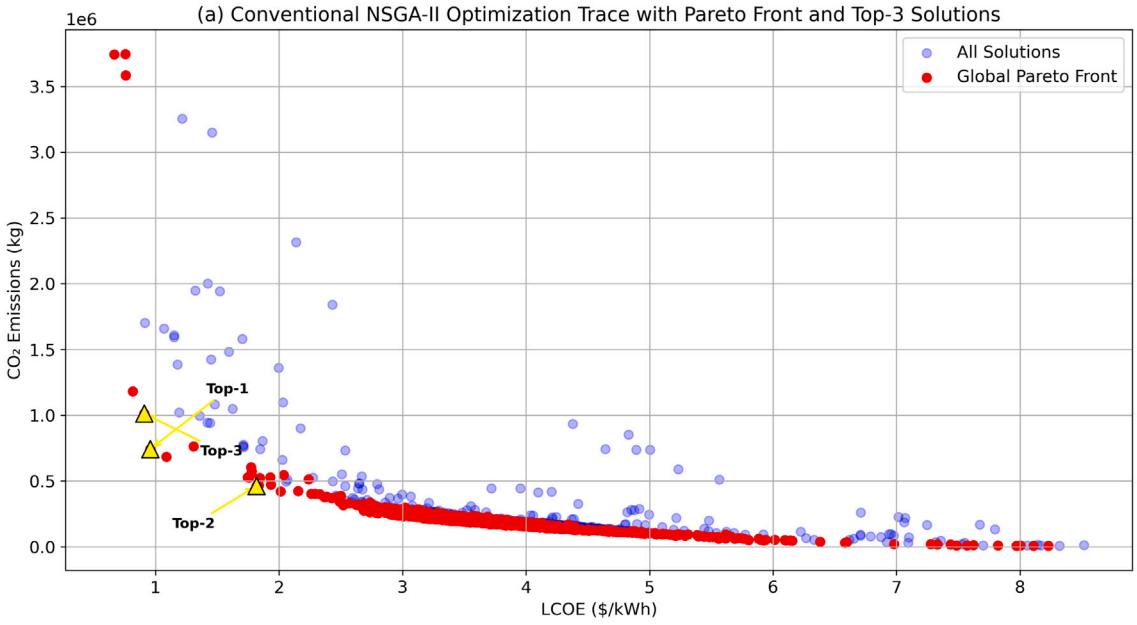

Rank	LCOE	CO_2 Emissions	Non-Renewable Hours	REF (%)
Top-1	0.9583	742545.52	803	81.36%
Top-2	1.8173	461690.17	587	84.52%
Top-3	0.9078	1012836.19	1123	78.73%

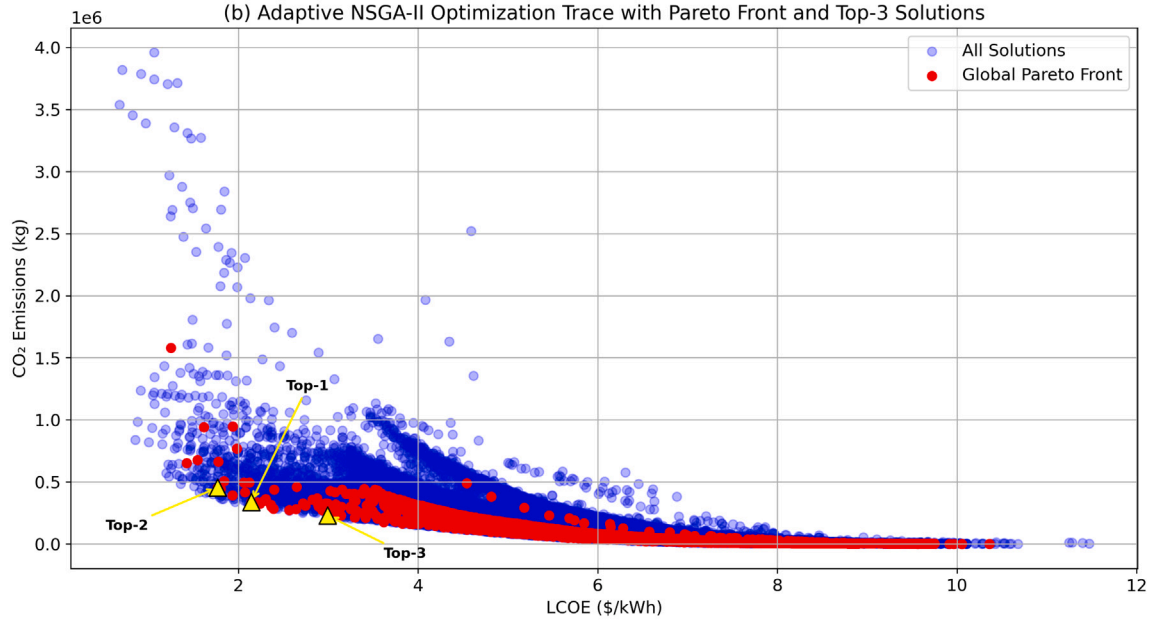

Rank	LCOE	CO_2 Emissions	Non-Renewable Hours	REF (%)
Top-1	2.1434	338087.55	323	87.91%
Top-2	1.7702	453433.89	457	87.78%
Top-3	2.9948	228749.24	216	87.92%

Fig. 8. Weighted top-3 solutions for (a) conventional NSGA-II and (b) A-NSGA-II, highlighted against Pareto fronts.

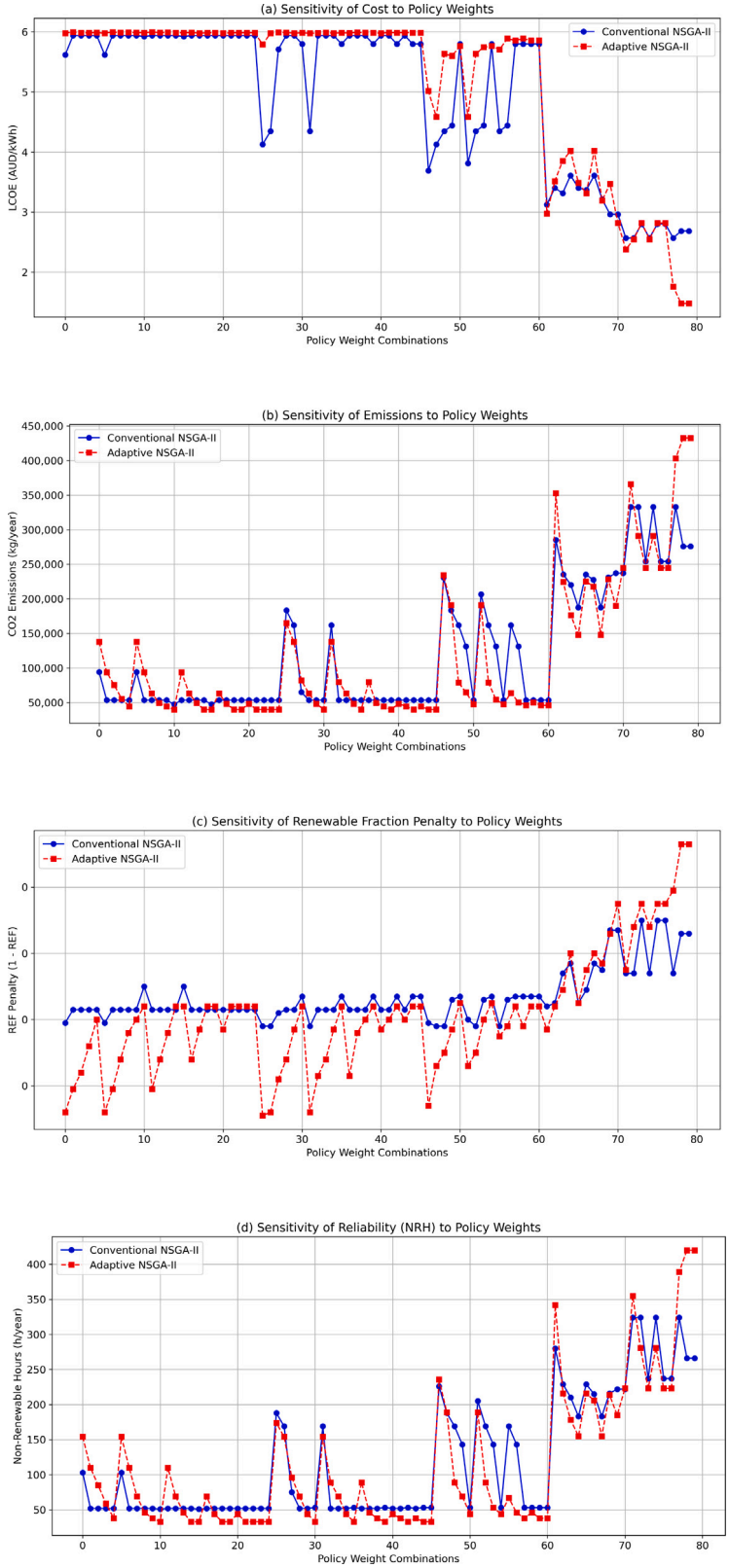

Fig. 9. Sensitivity analysis of conventional NSGA-II and A-NSGA-II across 80 policy weight combinations: (a) LCOE, (b) CO_2 emissions, (c) REF penalty, and (d) NRH.

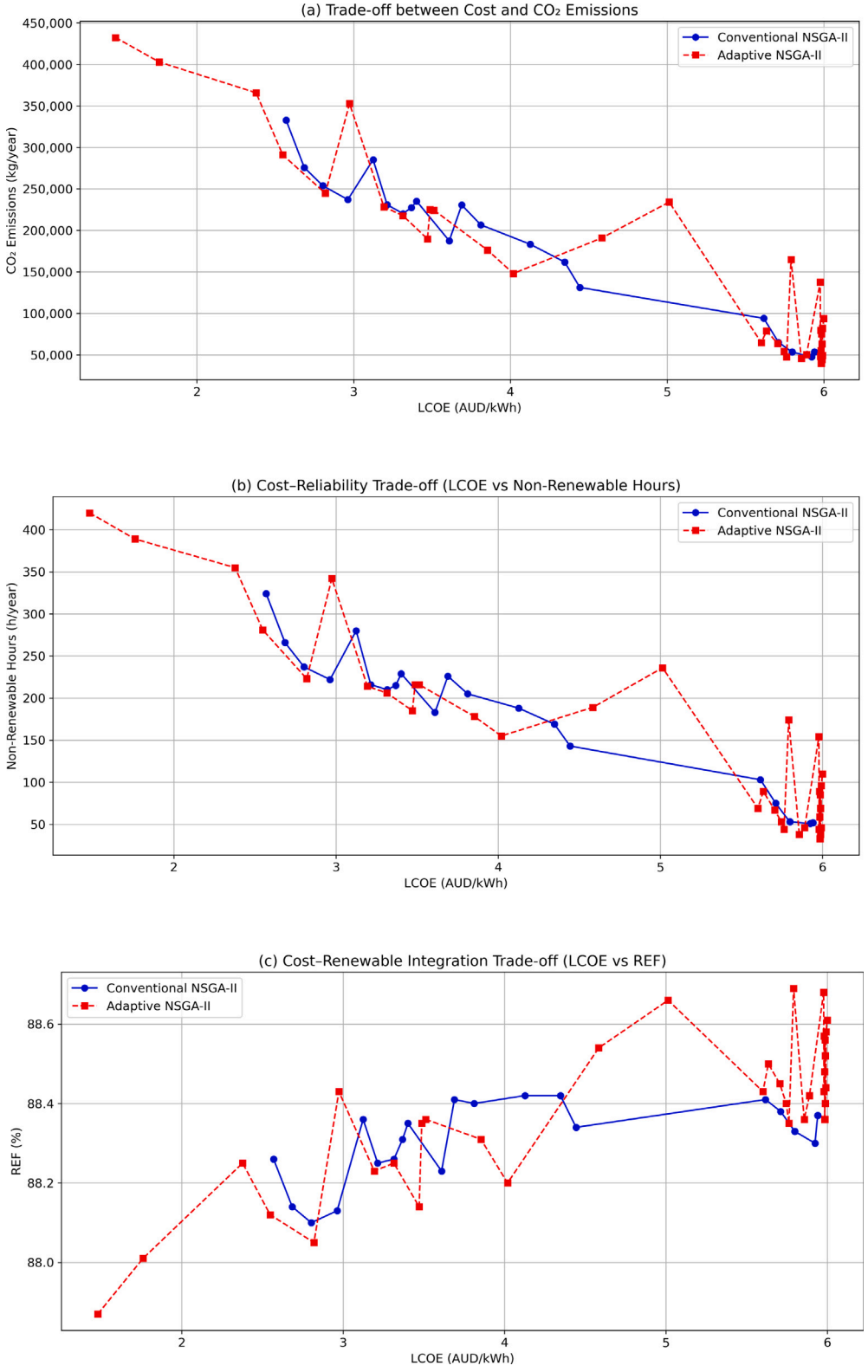

Fig. 10. Trade-off analysis between cost and key performance indicators between conventional NSGA-II and A-NSGA-II: (a) LCOE vs. CO_2 emissions, (b) LCOE vs. NRH, and (c) LCOE vs. REF.

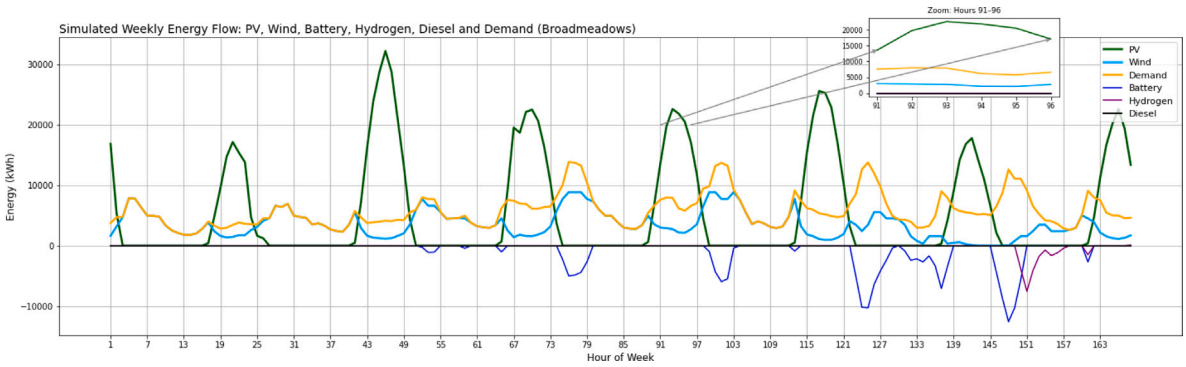

Fig. 11. Weekly energy flow under the A-NSGA-II optimal configuration, showing interactions among PV, wind, battery, hydrogen, diesel, and demand.

This system-level view confirms the earlier sensitivity findings that the A-NSGA-II design not only stabilizes objective outcomes but also ensures coordinated multi-source operation across timescales. Such synergy between renewable supply and storage integration underpins the A-NSGA-II framework's superiority in delivering practical, policy-resilient solutions. Having established both objective-level robustness and dynamic operational stability, the next section quantifies optimizer performance more formally using hypervolume, convergence, and spacing indicators.

3.3. Performance metrics evaluation

Beyond Pareto-front comparisons, formal indicators are required to quantify optimizer behavior. Three metrics were applied: Hypervolume, spacing distance, and convergence score. These measure the breadth of trade-off exploration, the distribution of solutions, and the proximity to the global optimum, respectively. Fig. 13(a–c) present results for both conventional NSGA-II and A-NSGA-II.

1. Hypervolume:
   In Fig. 12(a), A-NSGA-II achieves a rapid rise in Hypervolume within the first few generations and sustains a consistently higher value compared to the conventional NSGA-II. This indicates that A-NSGA-II strategies explore the objective space more effectively and capture a larger portion of the pareto-optimal region. The conventional NSGA-II algorithm shows slower growth and plateaus at a lower hypervolume, reflecting limited diversity and weaker coverage of trade-off surfaces.
2. Spacing:
   Fig. 12(b) shows the evolution of spacing distance. Both conventionla NSGA-II and A-NSGA-II algorithms reduce spacing distance as generations progress, but the A-NSGA-II maintains greater stability. The conventional NSGA-II algorithm displays sharper oscillations and occasional clustering, while A-NSGA-II remain evenly distributed. This uniform spread supports smoother trade-off representation and improves the interpretability of the final pareto front.
3. Convergence: As shown in Fig. 12(c), the A-NSGA-II steadily lowers its convergence score and approaches the reference front more closely. The conventional NSGA-II converges more slowly and stabilizes at higher distances, confirming that it remains further from the global optimum. whereas, A-NSGA-II balances exploration with exploitation, avoiding premature stagnation while moving populations toward globally efficient designs.

The three metrics converge on the same conclusion that A-NSGA-II produces pareto sets that are both broader and closer to the global optimum. The higher hypervolume confirms that it captures a wider and more valuable region of the solution space. The smoother spacing demonstrates its ability to maintain diversity without sacrificing balance, ensuring decision-makers receive a well-distributed portfolio of options in A-NSGA-II.

The improved convergence shows that these gains are not superficial but reflect a deeper movement toward globally efficient trade-off. In practice, this means that A-NSGA-II is less prone to premature stagnation and avoids the unstable extremes observed in the conventional NSGA-II algorithm. Instead, it delivers resilient and policy-relevant configurations that hold value across different planning priorities.

These findings not only confirm the superiority of A-NSGA-II within the case study system but also raise the question of whether such advantages generalize to other problem classes. To address this, the next section evaluates both algorithms on established benchmark functions, providing external validation of performance and robustness for both conventional NSGA-II and A-NSGA-II.

3.4. Benchmark function validation

To evaluate the generalizability of both solvers beyond the HRES, six well-established benchmark functions were used: *Sphere4*, *Rastrigin4*, *Schaffer_f7*, *Griewank4*, and two CEC2021 functions (*F1* and *F4*). These functions span convex, multimodal, and competition-grade landscapes, providing a rigorous test of convergence stability and robustness. All experiments were conducted under uniform conditions of 200 iterations and a fixed population size to ensure comparability. To maintain dimensional consistency with the four-objective HRES formulation, all benchmark problems were evaluated in a four-objective configuration. For classical test functions (e.g., Sphere4, Rastrigin4, Griewank4, Schaffer_f7), four objective components were constructed from the same decision vector to preserve comparable multi-objective search structure. Similarly, the CEC2021 benchmark functions were implemented in their four-objective variants. This uniform objective dimensionality ensures a fair and structurally consistent comparison between the synthetic benchmark problems and the four-objective HRES optimization case.

Performance was assessed from two complementary perspectives: statistical distributions of best fitness across runs (Fig. 13) and iteration-wise convergence trajectories (Fig. 14).

Fig. 13 highlights systematic differences in reliability. For *Sphere4*, *Rastrigin4*, *Schaffer_f7*, and *Griewank4*, the A-NSGA-II achieves consistently lower median fitness and narrower interquartile ranges. Outliers are sparse, indicating stable behavior across independent runs. In contrast, the conventional NSGA-II shows wider spreads, especially in *Rastrigin4* and *Schaffer_f7*, where multimodal features lead to weaker exploration and frequent stagnation. The CEC2021 functions present a greater challenge. On *F1*, A-NSGA-II results show more variability but still reach lower minima than the conventional NSGA-II. On *F4*, the A-NSGA-II demonstrates a clear advantage, with best fitness values nearly an order of magnitude smaller, confirming scalability to competition-grade problem structures.

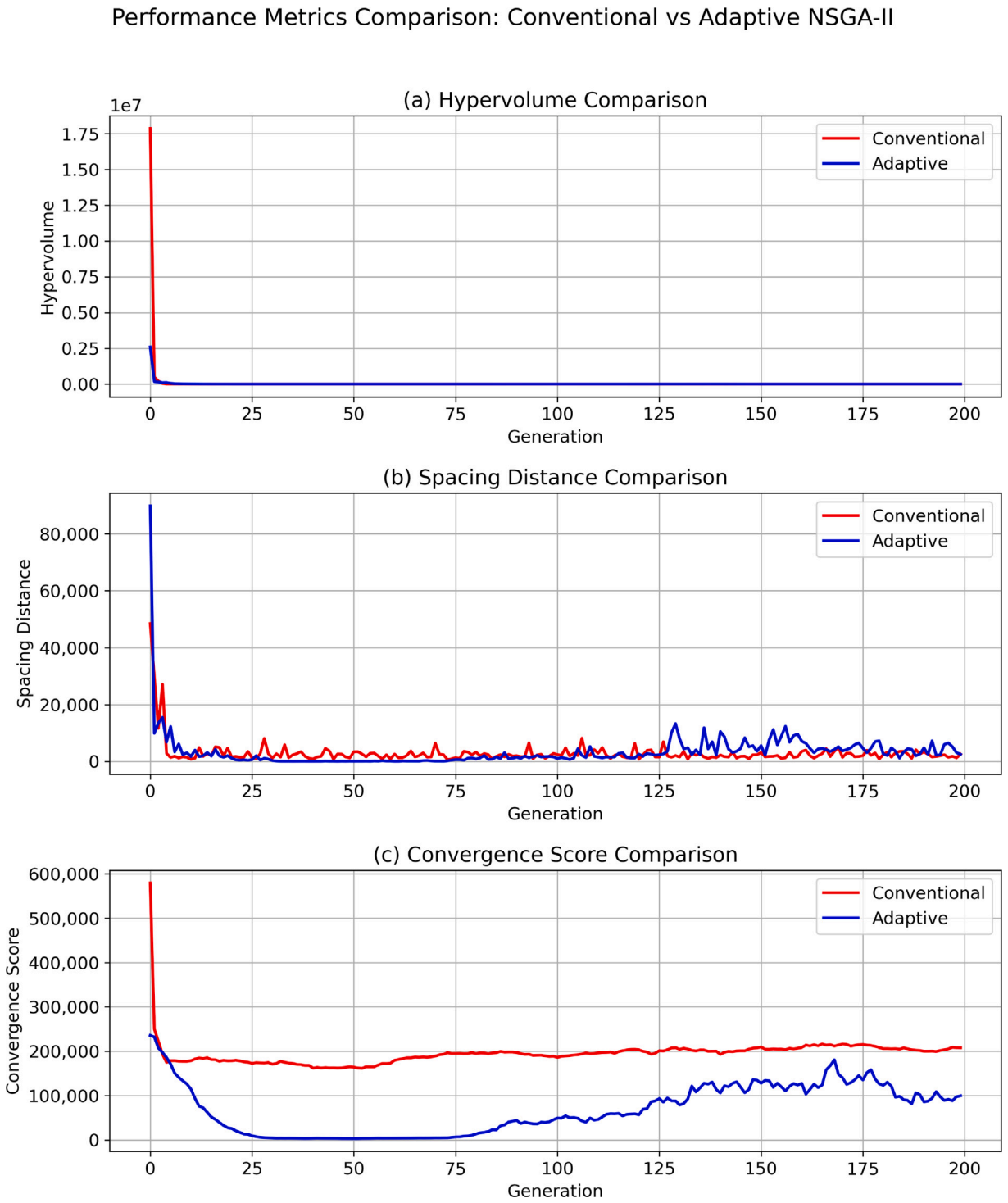

Fig. 12. Performance metrics comparison between conventional NSGA-II and A-NSGA-II: (a) hypervolume, (b) spacing distance, and (c) convergence score.

Iteration-wise results in Fig. 14 provide further evidence. On smooth landscapes such as *Sphere4* and *Schaffer_f7*, the A-NSGA-II convergence is faster and sustained, while the conventional NSGA-II plateaus early. In multimodal problems like *Rastrigin4* and *Griewank4*, the A-NSGA-II solutions avoid stagnation and continue refining beyond 100 iterations, where conventional NSGA-II progress largely halts. The advantage is most pronounced in *CEC2021-F4*, where the A-NSGA-II solver converges sharply and stably, whereas the conventional NSGA-II solver oscillates heavily before flattening at higher fitness values. This behavior demonstrates the A-NSGA-II capacity to maintain exploration while steadily guiding populations toward global optima.

The superiority of the A-NSGA-II arises from its design. Adaptive mutation pressure and preference-guided search maintain diversity in multimodal landscapes while accelerating convergence on smooth ones. This balance between exploration and exploitation explains why A-NSGA-II consistently outperform conventional NSGA-II results. Importantly, the reduced variance seen in Fig. 13 confirms that performance is stable across runs, not dependent on chance. Such robustness strengthens confidence that the A-NSGA-II algorithm can be reliably deployed in both controlled benchmark settings and real-world energy planning.

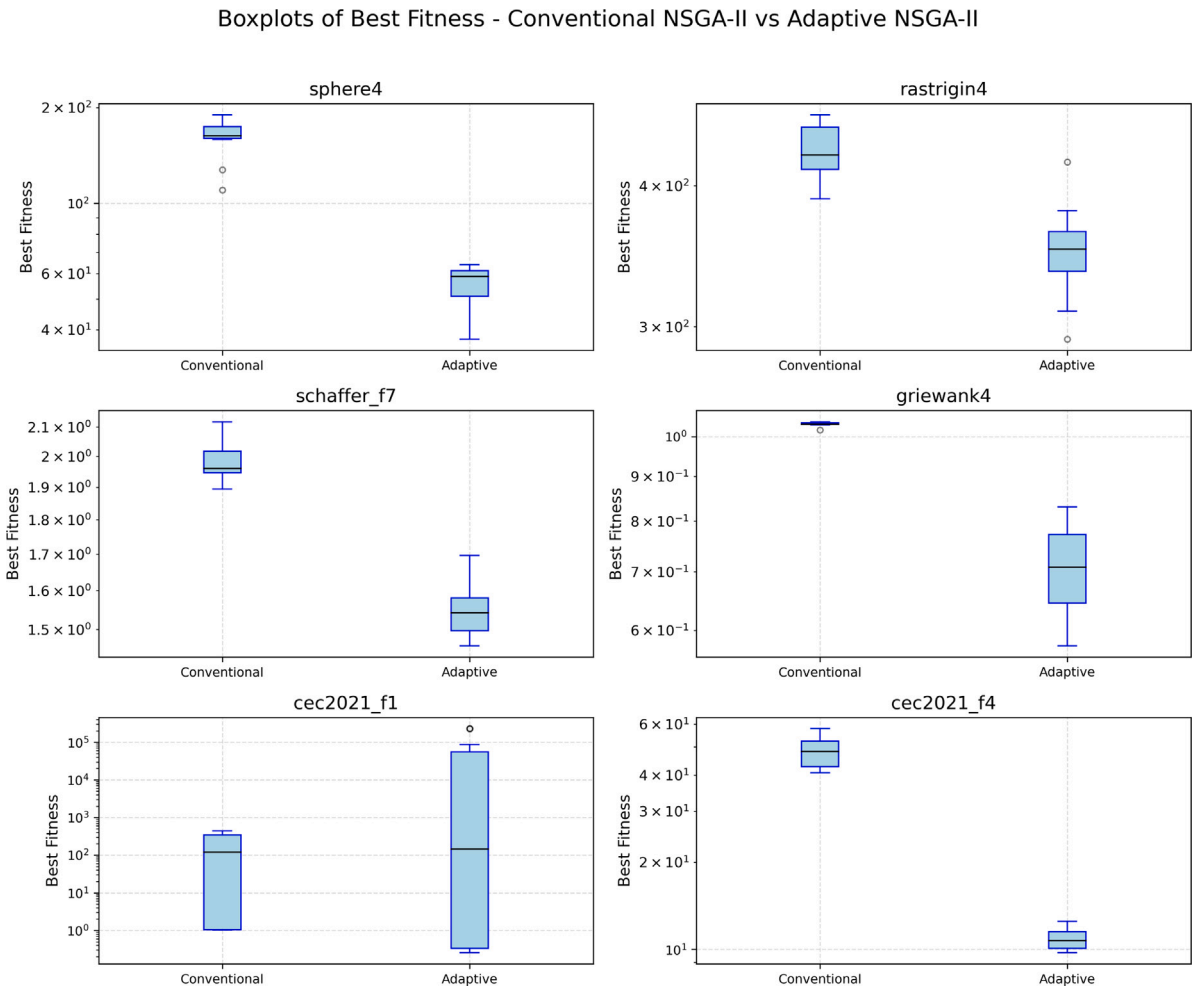

Fig. 13. Boxplots of best fitness values for six benchmark functions comparing conventional NSGA-II and A-NSGA-II.

These benchmarks analysis shows that the A-NSGA-II is not problem-specific. It performs strongly across convex, multimodal, and competition-grade landscapes. The results confirm that the adaptive mechanisms are transferable, offering faster convergence, reduced variance, and better resilience against local optima. This broad applicability reinforces the earlier findings from the HRES case study, and positions proposed A-NSGA-II as a versatile and dependable evolutionary framework.

4. Discussion

This section interprets the optimization results from technical, environmental, and economic perspectives, and relates the findings to broader energy transition objectives. It examines the role of hydrogen integration, storage coordination, policy-driven weighting scenarios, and benchmark validation outcomes. Practical implications, techno-economic considerations, and transferability to other contexts are also discussed to position the proposed framework within real-world planning applications.

4.1. Implications for H-HRES design and operation

The results highlight the operational and design benefits of using A-NSGA-II optimization for H-HRESs. The conventional NSGA-II configuration performs poorly, with high cost, extensive diesel use, and limited renewable utilization. Both NSGA-II variants improve these outcomes, but the A-NSGA-II achieves significantly better performance, including a 45% reduction in CO_2 emissions, a 49% reduction in NRHs, and an increase in REF from 82.3% to 88.4%. Similar observations, such as [99,100], were made in recent comparative optimization studies where conventional NSGA-II often struggled to maintain diversity when handling multiple conflicting objectives. [99] found that standard NSGA-II fails to preserve solutions representing distinct system configurations despite their non-dominance in high-dimensional objective spaces, while [100] reported that crowding-distance mechanisms become uninformative beyond three objectives. The present results reinforce these findings and demonstrate that A-NSGA-II mechanisms including dynamic mutation, K-means clustering, and feasibility-aware local search address these limitations without fundamentally modifying the NSGA-II architecture. Although the A-NSGA-II incorporates additional mechanisms such as K-means initialization and feasibility-aware local search, the overall computational burden remains dominated by the hourly dispatch simulation (8784 time steps) evaluated for each candidate solution. Consequently, the incremental runtime associated with adaptive operations is small relative to the full simulation cost. The focus of this study is therefore on solution quality and robustness rather than algorithmic execution time, which remains comparable in practical planning-scale applications.

A key insight is the coordinated use of battery and hydrogen storage across different timescales. The A-NSGA-II consistently increases both storage capacities and deploys them strategically: batteries manage short-term diurnal fluctuations (4–8 h of discharge), while hydrogen provides multi-day to seasonal support (8–48 h of fuel cell discharge). This layered storage architecture directly reduces curtailment and improves operational stability across varying demand and renewable

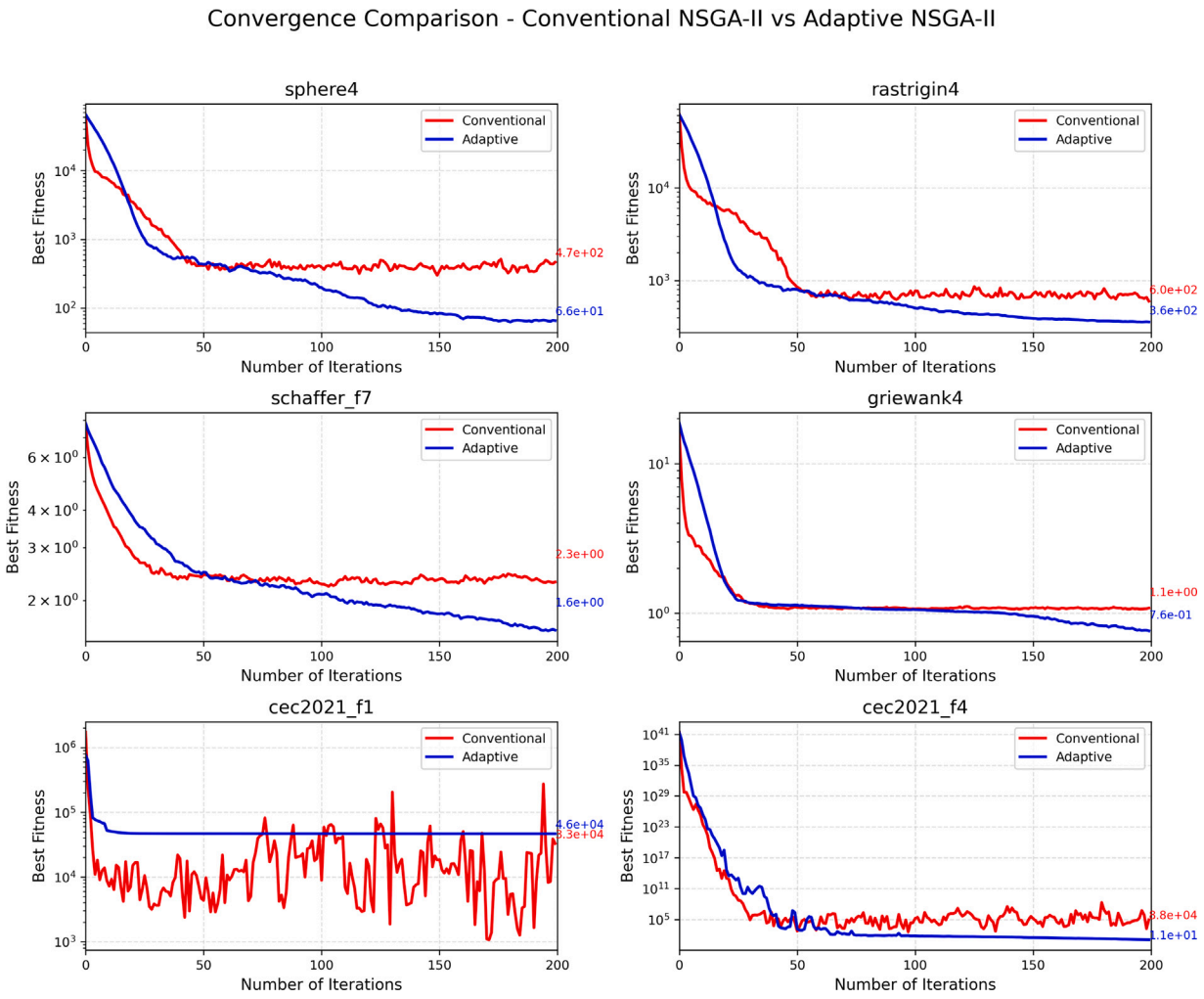

Fig. 14. Convergence trajectories of best fitness across 200 iterations for six benchmark functions for conventional NSGA-II and A-NSGA-II.

resource conditions. This behavior aligns with recent H-HRES studies [101,102], showing that balanced storage chains reduce energy waste and enhance system resilience. [101] used surrogate-assisted optimization and found that coordinated battery-hydrogen systems significantly outperform single-storage designs in minimizing cost-emissions trade-offs. While [102] showed that multi-timescale storage coordination is essential for maintaining stable frequency and power quality in high-renewable penetration scenarios. Diesel operation is also substantially reduced compared to baseline diesel-centric systems. Many hydrogen-based microgrid studies report 200–600 annual diesel hours even after optimization; for example, [103] reported 486 h annually in an off-grid system, and [99] found more than 300 h typical in their case studies. In contrast, the A-NSGA-II reduces diesel operation to only 53 h annually (0.6% of operating time), representing a 10-fold improvement over comparable systems. This achievement demonstrates that increasing hydrogen storage reserves (from 386 to 1000 kg) and enhancing battery flexibility (7% capacity increase) can push H-HRES substantially closer to diesel-free operation while maintaining reliability. A critical objective for regions pursuing high renewable penetration under decarbonization targets.

The A-NSGA-II solutions maintain REF above 87%, exceeding the 70%–85% range reported in comparable PV–wind–H_2 microgrids [104, 105]. Notably, REF stability remains high across all 80 policy weighting scenarios tested, indicating that renewable utilization does not deteriorate even when cost receives higher priority in the optimization objective function. This robustness is valuable for energy planners operating under evolving policy and economic constraints, as it demonstrates that the system can maintain environmental performance targets regardless of shifting stakeholder priorities. Another notable fNotably, REF stability remains high across all 80 policy weighting scenarios tested, indicating that renewable utilization does not deteriorate even when cost receives higher priority in the optimization objective function. This robustness is valuable for energy planners operating under evolving policy and economic constraints, as it demonstrates that the system can maintain environmental performance targets regardless of shifting stakeholder priorities. The A-NSGA-IIselected larger electrolyzer capacity (5161 kW compared to 4798 kW for conventional NSGA-II), enabling more complete capture of renewable oversupply, reduced curtailment, and stronger hydrogen production during high-generation periods. This reserve capacity ensures reliable hydrogen availability during low-renewable windows and reduces forced renewable spillage. [100,106] highlighted electrolyzer sizing flexibility as a key factor in stable power-to-hydrogen operation; the present results provide empirical validation through hourly dispatch-coupled optimization that larger electrolyzer capacity is economically justified when combined with optimized hydrogen storage.

The performance metrics provide quantitative evidence of algorithmic superiority. The A-NSGA-II achieves higher hypervolume (indicating broader coverage of the trade-off surface), lower spacing values (indicating more uniform distribution of solutions), and superior convergence scores (indicating proximity to the true Pareto front) compared to conventional NSGA-II. These improvements align with

recent work in [107] demonstrating that adaptive mutation and enhanced diversity management significantly improve pareto front quality in multi-objective energy system optimization. The present study extends these insights by validating adaptive mechanisms within a fully dispatch-coupled H-HRES environment with 8784 hourly constraints and non-linear component models.

Overall, the A-NSGA-II produces system designs that are more balanced across conflicting objectives, lower in emissions, more renewable-driven, and substantially less dependent on fossil backup. These outcomes demonstrate the value of coordinated storage sizing, flexible conversion capacity, and adaptive evolutionary search in advancing hydrogen-integrated hybrid systems toward practical, low-emission, community-scale deployment aligned with decarbonization policy goals.

4.2. Robustness to policy priorities and algorithm generalizability

A distinctive feature of the A-NSGA-II framework is its ability to generate solutions that remain viable across different stakeholder priority weightings. When evaluated across 80 policy-weighting scenarios ranging from cost-dominated to emissions-driven to resilience-oriented configurations—the A-NSGA-II variant sustained stable objective trajectories. Across all cases, REF consistently exceeding 87%, LCOE remaining within 1.77–2.99 AUD/kWh, and NRH contained below 500 h annually. In contrast, the conventional NSGA-II showed the opposite behavior. It frequently collapsed toward unrealistic low-cost solutions, with LCOE dropping below 1.0 AUD/kWh and CO_2 emissions rising above 1,000,000 kg in cost-prioritized settings. Similar behavior has been reported in recent multi-objective energy planning studies. [108] comparison of 42 weighting and decision-making models found that ranking stability depends on how well the optimization algorithm captures the full structure of the Pareto front. Likewise, [109] showed that renewable energy rankings can shift sharply when criterion weights change, highlighting the need for robust portfolios rather than single-point solutions. The behavior observed in the A-NSGA-II confirms that its adaptive mechanisms generate genuinely diverse pareto fronts that preserve coherent trade-offs instead of collapsing toward fragile corner regions when policy preferences shift.

The weighted-ranking approach used in this study further strengthens the optimization framework as a decision-support tool. By combining objective-specific ranks according to stakeholder preferences, the method highlights solutions that deliver balanced performance rather than excelling in a single objective. Recent multi-criteria studies reinforce this point. [110] showed that stable rankings for clean energy technologies arise only when evaluation methods account for trade-off stability across criteria. [111] similarly reported that fuzzy decision-making paired with pareto analysis offers clearer guidance when algorithms generate evenly distributed fronts. The A-NSGA-II lower spacing metric aligns with these findings, as it allows planners to select configurations that match cost, CO_2 emissions, or resilience priorities without being pushed toward extreme corners of the trade-off space. This ability to maintain coherent and balanced solutions across different governance settings also builds confidence in long-term policy planning, where priorities may shift with changing emissions targets, hydrogen incentives, or energy-security requirements.

The validation of the A-NSGA-II across six benchmark problems—Sphere-4D, Rastrigin-4D, Griewank-4D, Schaffer F7, CEC2021-F1, and CEC2021-F4—shows that its strengths extend well beyond the H-HRES application. Across all six benchmark problems, the adaptive variant achieved faster convergence, lower fitness values, and reduced variance across independent runs compared with the conventional NSGA-II. These outcomes are consistent with recent benchmarking studies. [112] reported that clustering-enhanced NSGA-II variants improve convergence on CEC multi-objective test sets by preserving population structure. [113] showed that good-point initialization and opposition-based learning reduce local-optima entrapment and increase solution uniformity. [114] found that NSGA-II variants equipped with diversity-management strategies outperform MPSO and Multi-objective Ant Lion Optimizer Algorithm (MOALOA) for energy-storage optimization in distribution networks. Similar findings have been reported in other recent works. [115] demonstrated that adaptive mutation schedules improve exploration on multimodal functions, while [116] showed that hybrid NSGA-II structures achieve better stability across heterogeneous test landscapes. The consistent performance of the A-NSGA-II across both synthetic benchmarks and the real-world H-HRES model therefore confirms that its mechanisms — dynamic mutation, K-means clustering, and feasibility-aware refinement — deliver genuine algorithmic improvements rather than case-specific tuning.

These insights have important implications for planners and regulators. Algorithm selections directly shapes the quality of solutions produced in multi-objective optimization, and methods that perform well only on narrow problem types can mislead decision-makers when applied to new settings. [117] noted that such overfitting often appears when benchmarking relies on limited test suites, which can hide weaknesses that surface in real-world applications. The A-NSGA-II avoids this issue by performing consistently across diverse benchmark functions, including the highly multimodal CEC2021-F4 where the conventional NSGA-II showed clear oscillatory behavior. This stability indicates that its adaptive mechanisms are robust to different landscape characteristics. For researchers and practitioners deploying H-HRES in varied geographic or climatic contexts, this transferability reduces the risk that optimization outputs are shaped by algorithmic artefacts rather than real system trade-offs, and it strengthens confidence in using optimization tools for hydrogen-integrated energy planning.

4.3. Hydrogen storage integration and pathway to low-carbon distributed energy systems

Hydrogen storage emerges as a central component of the A-NSGA-II optimal designs and plays a key role in enabling low-carbon distributed energy systems. The A-NSGA-II solution set includes 1000 kg of hydrogen storage, more than double the baseline configuration. This increase highlights the importance of coordinating storage across multiple timescales. Batteries provide high-power, short-duration balancing and cycle over 4–8 h, making them suitable for diurnal fluctuations. Hydrogen offers long-duration support by capturing multi-day renewable surpluses and supplying energy during extended low-generation periods that last days to weeks. This temporal separation reduces pressure on single-technology storage and allows each resource to operate where it is most efficient.

It is important to clarify that the dispatch strategy follows a hierarchical priority in which battery storage is utilized before hydrogen discharge (Fig. 4). This rule-based sequencing reflects practical microgrid energy management practice, where short-duration storage is preferred to minimize conversion losses and preserve hydrogen for long-term balancing. Although hydrogen is not prioritized at the hourly control level, seasonal utilization is not constrained by this hierarchy. Hydrogen accumulation during extended renewable surplus periods is governed primarily by electrolyzer capacity, storage size, and inter-temporal mass balance rather than dispatch order alone. Therefore, the ability to support multi-day or seasonal deficits remains determined by optimized component sizing and cumulative surplus availability. Future work may explore predictive or co-optimized dispatch strategies (e.g., MILP or Model Predictive Control (MPC)-based control) to further enhance seasonal allocation, but the present rule-based framework captures the dominant long-duration storage dynamics within computationally tractable evolutionary optimization.

Recent studies support this architecture. [118] showed that hybrid battery–hydrogen storage increases system capacity factors to more than 60%–80% and boosts capacity credits close to 100% compared with battery-only or hydrogen-only systems. [119] demonstrated that hydrogen acts as both a long-duration storage medium and an energy

carrier that strengthens complementarity among renewable resources. The synergy observed here is consistent with these findings. In contrast, the A-NSGA-II solutions require only 53 h. This difference illustrates the effectiveness of coordinated hydrogen and battery storage in reducing fossil reliance.

While the optimization results demonstrate clear environmental and reliability advantages from increased hydrogen and battery storage capacities, practical deployment requires consideration of physical and operational constraints. Expanded battery banks demand additional installation space, structural support, and thermal management systems, particularly in residential or community-scale settings. Likewise, larger hydrogen storage volumes and electrolyzer capacity introduce balance-of-plant requirements such as compression, safety monitoring, ventilation, and periodic inspection to comply with safety regulations. Therefore, although the A-NSGA-II solutions offer substantial reductions in diesel reliance and emissions, real-world implementation would require careful site-specific engineering assessment to balance technical performance with spatial availability, maintenance planning, and operational complexity.

The optimization results show that hydrogen plays a direct role in supporting community-level decarbonization. The A-NSGA-II solutions reduce annual CO_2 emissions by 45%, from 93,979 to 51,823 kg, which is an absolute reduction of about 42 tons per year. This improvement reflects lower diesel use, with NRH falling from 103 to 53, and higher renewable utilization, with REF increasing from 82.3% to 88.4%. These values represent operational emissions only, but even if embodied CO_2 emissions were added — typically 20%–30% above operational totals — the relative ranking of system configurations would not change. Studies of hydrogen-integrated microgrids often report renewable fractions between 70% and 85% and continued reliance on fossil generators for reliability, as seen in work by [113,120,121]. The performance achieved here exceeds those benchmarks and shows that hydrogen storage, when optimized together with battery capacity and electrolyzer size, can maintain high renewable penetration without reducing system stability. The findings also align with Australia's National Hydrogen Strategy (2024 update) [122], which identifies hydrogen as a core element of national net-zero plans and highlights growth regions such as Gladstone, the Pilbara, and the Eyre Peninsula. The stability of REF above 87% across all 80 stakeholder weightings strengthens this policy relevance and shows that high environmental performance remains achievable even when cost becomes the primary planning criterion. This level of robustness is important for equitable energy transition planning, where communities must manage affordability, CO_2 emissions, and reliability at the same time.

The economic outlook for hydrogen integration depends on expected declines in component costs over the next decade. Current electrolyzer costs of AUD 3000/kW and fuel cell costs of AUD 600/kW yield the reported LCOE of 5.81 AUD/kWh. However, hydrogen industry learning curves suggest substantial cost reductions. [101] conducted learning curve analysis for green hydrogen production and projected LCOH to fall from current levels to AUD 3.40/kg by 2035 via electrolyzer and system efficiency improvements. [123] modeled progressive technology development and found green hydrogen costs likely to fall below AUD 4.80/kg by 2030, achieving competitiveness with incumbent fossil hydrogen. These learning rates, applied to electrolyzer capital costs in the range of 10%–13% per doubling of cumulative deployment. Applying these rates to the present system suggests that the A-NSGA-II LCOE could fall to around 3.5 AUD/kWh within a decade. This shift narrows the cost gap with grid electricity and strengthens the economic case for hydrogen at residential and community scale. It also positions hydrogen as a practical complement to batteries in systems that aim to balance affordability with high renewable penetration.

The renewable energy fraction of 88.41% in the A-NSGA-II solutions represents a major step toward regional energy autonomy. This value is higher than the 70%–85% renewable fractions commonly reported in comparable PV–wind–hydrogen systems, including recent studies [21,83,113]. The stability of REF across all 80 stakeholder weightings shows that the hydrogen-integrated architecture remains robust when planners shift priorities between cost, emissions, and resilience. This flexibility is valuable for regions that face energy security challenges or grid infrastructure limitations. The Australian context fits this profile, as it combines strong solar and wind resources with dispersed demand and growing policy support for distributed renewable deployment [124]. Several national assessments, including the Australian Energy Market Operator (AEMO) [63] and the National Hydrogen Strategy (NHS) [125], highlight the need for localized renewable solutions that can operate reliably under variable conditions. Hydrogen integration in residential and microgrid planning provides a practical bridge between near-term battery-focused designs and long-term hydrogen infrastructure. It allows communities to increase renewable penetration and reduce reliance on centralized grids without requiring a complete redesign of existing energy systems.

A-NSGA-II reveals how hydrogen can operate as a flexible anchor in distributed renewable systems. The proposed A-NSGA-II identifies storage configurations that balance short and long duration needs without increasing reliance on fossil backup. This behavior shows that hydrogen becomes most valuable when its sizing and operation are coordinated through a robust optimization framework rather than fixed by simple heuristics. By exposing stable and feasible design regions across many planning conditions, the A-NSGA-II approach demonstrates that hydrogen-integrated H-HRES can serve as a practical foundation for future low-carbon community energy systems.

Although the present study focuses on Broadmeadows, Melbourne, the proposed optimization and dispatch framework is not location-specific. The modeling structure, including the hourly dispatch logic, component sizing formulation, and multi-objective A-NSGA-II optimization, is fully modular and can be applied to other climatic regions by substituting local meteorological data, demand profiles, and techno-economic parameters.

In regions with higher solar irradiance, stronger wind regimes, or different seasonal load characteristics, the optimization would naturally adjust system sizing and dispatch behavior to reflect local resource availability and demand variability. Similarly, the framework can accommodate diverse policy targets, such as stricter renewable penetration thresholds or carbon pricing mechanisms, without structural modification of the algorithm. Therefore, while quantitative results are case-specific, the methodological framework is transferable to other suburban, rural, or grid-connected contexts with appropriate data calibration.

5. Conclusion

This study developed and validated an A-NSGA-II framework for the optimization of a hydrogen-integrated HRES in Broadmeadows, Melbourne. The framework was benchmarked against conventional NSGA-II across four objectives: LCOE, CO_2 emissions, NRH, and REF penalty. A comprehensive evaluation was undertaken through pareto analysis, rank-based optimal selection, weighted Top-3 solutions, sensitivity testing, and benchmark validation.

The conventional NSGA-II bsed baseline system, constructed through static sizing assumptions, highlighted the limitations of non-optimized configurations, producing prohibitively high costs (LCOE = 2.46 AUD/kWh), over 1000 h of diesel reliance, and an REF of only 75.3%. In contrast, pareto-front comparisons revealed that the A-NSGA-II consistently produced denser and more balanced trade-offs with lower REF penalties and reduced dependence on non-renewables, whereas the conventional NSGA-II often converged to unsustainable extremes. Rank-based evaluations confirmed these advantages, with the adaptive framework achieving ~45% lower CO_2 emissions (93,979 → 51,823 kg/year), halving NRH (103 → 53), and slightly reducing LCOE (5.92 → 5.81 AUD/kWh).

Policy-oriented weighted Top-3 solutions further underlined the difference: conventional NSGA-II reached very low costs (<1 AUD/kWh) only by incurring excessive emissions (>700,000 kg) and prolonged diesel use (>800 h), while A-NSGA-II portfolios consistently maintained REF above 87.7% and emissions as low as 228,749 kg, providing a more practical basis for decarbonization strategies. Sensitivity analysis across 80 weighting scenarios demonstrated the stability of the A-NSGA-II approach, showing smooth trajectories for cost, CO_2 emissions, and REF under shifting priorities, unlike the sharp fluctuations exhibited by the conventional NSGA-II algorithm. Performance metrics reinforced these outcomes, with A-NSGA-II achieving higher hypervolume, smoother spacing, and stronger convergence.

Benchmark validation across six synthetic functions (Sphere4, Rastrigin4, Schaffer_F7, Griewank4, CEC2021-F1, and CEC2021-F10) confirmed transferability, as the A-NSGA-II framework converged faster, achieved lower median values, and reduced variance across runs, excelling particularly in multimodal and competition-grade landscapes.

As summary, these results establish that proposed A-NSGA-II is more effective framework for HRES planning. It improves economic efficiency, lowers CO_2 emissions, enhances renewable penetration, and delivers stable outcomes across diverse policy preferences. The method is not only effective for Broadmeadows but also transferable to broader renewable–hydrogen contexts, strengthening the evidence base for adaptive evolutionary approaches in sustainable energy transitions.

One of the limitation of this study is restricted to a single case study in Broadmeadows, and broader validation across different regions, with varied resource and demand conditions, remains necessary. The economic analysis reflects present technology costs and does not incorporate projected cost reductions for renewable and hydrogen technologies. In addition, environmental impacts are limited to operational CO_2, excluding full life-cycle effects. Future research should address these gaps through dynamic cost learning curves, life-cycle assessments, and adaptive dispatch strategies (e.g.. MILP) linked to market and weather signals. Furthermore, the scalability of the framework to larger and more complex multi-energy systems warrants further investigation.

Despite these limitations, the proposed A-NSGA-II demonstrates strong potential as a transferable optimization tool. Its capacity to balance cost, emissions, and reliability provides actionable insights for energy planners and supports policy objectives targeting deep decarbonization and long-term energy security. As the global energy transition accelerates, adaptive multi-objective optimization frameworks such as proposed A-NSGA-II provide essential tools for designing resilient, low-carbon, and hydrogen-ready energy systems.

Acronyms

R^2	R-squared
A-NSGA-II	Adaptive Non-dominated Sorting Genetic Algorithm II
AC	Alternating Current
AEMO	Australian Energy Market Operator
BESS	Battery Energy Storage System
CAPEX	Capital Expenditure
CEC	Commission of the European Communities
CO_2	Carbon dioxide
CRF	Capital Recovery Factor
DC	Direct Current
DoD	Depth of Discharge
EA	Evolutionary Algorithm
EMDS	Energy Management Dispatch Strategy
EV	Electrical Vehicle
GA	Genetic Algorithm
GHG	Greenhouse Gas
GHI	Global Horizontal Irradiance
$GtCO_2$	Gigatons of carbon dioxide
GWO	Gray Wolf Optimizer
H-HRES	Hydrogen-Integrated Hybrid Renewable Energy Systems
H_2	Hydrogen
HRES	Hybrid Renewable Energy Systems
IEC	International Electrotechnical Commission
LCOE	Levelized Cost of Energy
LCOH	Levelized Cost of Hydrogen
LSTM	Long Short-Term Memory
MAE	Mean Absolute Error
MILP	Mixed-integer Linear Programming
ML	Machine Learning
MOALOA	Multi-objective Ant Lion Optimizer Algorithm
MOEA	Multi-Objective Evolutionary Algorithm
MPC	Model Predictive Control
MPSO	Multi-objective Particle Swarm Optimization
NASA POWER	National Aeronautics and Space Administration Prediction Of Worldwide Energy Resources
NPC	Net Present Cost
NRH	Non-renewable operating hours
NSGA-II	Non-dominated Sorting Genetic Algorithm II
NSGA-III	Non-dominated Sorting Genetic Algorithm III
O&M	Operation and Maintenance
PEM	Proton Exchange Membrane
PV	Photovoltaic
PVGIS (TMY)	Photovoltaic Geographical Information System Typical Meteorological Year
RE	Renewable Energy
REF	Renewable energy fraction
RF	Random Forest
RMSE	Root Mean Square Error
SOC	State of Charge
TOPSIS	Technique for Order Preference by Similarity to Ideal Solution
WT	Wind turbines
XGBoost	Extreme Gradient Boosting

CRediT authorship contribution statement

Waqar Ali Khan: Writing – original draft, Visualization, Software, Methodology, Investigation, Formal analysis, Conceptualization. **Ashkan Pakseresht:** Writing – review & editing, Supervision. **Caslon Chua:** Writing – review & editing, Supervision. **Ali Yavari:** Writing – review & editing, Supervision, Investigation, Funding acquisition, Conceptualization.

Declaration of competing interest

The authors declare that they have no known competing financial interests or personal relationships that could have appeared to influence the work reported in this paper.

Acknowledgments

The work has been supported by the Future Energy Exports Cooperative Research Centre (FEnEx CRC), whose activities are funded by the Australian Government's Cooperative Research Centre Program.

References

[1] Raimi D, et al. Global energy outlook 2024: Peaks or plateaus. 2024.
[2] Diesendorf M, Taylor R. Transitioning the energy system. In: The path to a sustainable civilisation. Springer; 2023, p. 53–88.
[3] Duraiswami RA. Global carbon capture and storage efforts: Challenges and opportunities. J Geol Soc India 2025;101(2):143–8.
[4] Gielen D, Boshell F, Saygin D, Bazilian MD, Wagner N, Gorini R. The role of renewable energy in the global energy transformation. Energy Strat Rev 2019;24:38–50.
[5] Al-Rawashdeh H, et al. Performance analysis of a hybrid renewable-energy system for green buildings to improve efficiency and reduce ghg emissions with multiple scenarios. Sustainability 2023;15(9):7529.
[6] Raturi AK. Renewables 2019 global status report. 2019.
[7] Khan WA, Pakseresht A, Chua C, Yavari A. Energy resilience and decarbonisation via hybrid renewable energy systems: A techno-economic study. Int J Hydrog Energy 2026.
[8] Sinha S, Chandel S. Review of recent trends in optimization techniques for solar photovoltaic–wind based hybrid energy systems. Renew Sustain Energy Rev 2015;50:755–69.
[9] Gutiérrez-Martín F, Amodio L, Pagano M. Hydrogen production by water electrolysis and off-grid solar pv. Int J Hydrog Energy 2021;46(57):29038–48.
[10] Modu B, et al. A systematic review of hybrid renewable energy systems with hydrogen storage. Int J Hydrog Energy 2023;48(97):38354–73.
[11] Birol F. The future of hydrogen: seizing today's opportunities, iEA report for the G20. 2019.
[12] Council H. Hydrogen insights 2022. 2022.
[13] Yavari A, Harrison CJ, Gorji SA, Shafiei M. Hydrogen 4.0: A cyber–physical system for renewable hydrogen energy plants. Sensors 2024;24(10). URL https://www.mdpi.com/1424-8220/24/10/3239.
[14] Olabi A, et al. Compressed air energy storage systems: Components and operating parameters. J Energy Storage 2021;34:102000.
[15] Roy TK, et al. Techno-economic and environmental optimization of hydrogen-based hybrid energy systems for remote off-grid australian communities. 2025, 101083,
[16] Dawood F, Anda M, Shafiullah G. Hydrogen production for energy: An overview. Int J Hydrog Energy 2020;45(7):3847–69.
[17] He Y, et al. Multi-objective planning-operation co-optimization of renewable energy system with hybrid energy storages. Renew Energy 2022;184:776–90.
[18] Deb K, et al. A fast and elitist multiobjective genetic algorithm: Nsga-ii. IEEE Trans Evol Comput 2002;6(2):182–97.
[19] Doerr B, Korkotashvili D, Krejca MS. Difficulties of the nsga-ii with the many-objective leadingones problem. IEEE Trans Evol Comput 2025.
[20] Hlal MI, et al. Nsga-ii and mopso based optimization for sizing of hybrid pv/wind/battery energy storage system. Int J Power Electron Drive Syst 2019;10(1):463.
[21] Reis MJ. Symmetry-guided surrogate-assisted nsga-ii for multi-objective optimization of renewable energy systems. Symmetry 2025;17(8):1367.
[22] Hossain MA, et al. Modified pso algorithm for real-time energy management in grid-connected microgrids. Renew Energy 2019;136:746–57.
[23] Liang H, et al. A multiobjective hybrid bat algorithm for combined economic/emission dispatch. Int J Electr Power Energy Syst 2018;101:103–15.
[24] Zhang J, et al. Safety resilience evaluation of hydrogen refueling stations based on improved topsis approach. Int J Hydrog Energy 2024;66:396–405.
[25] Zhu Z, et al. Improved grey wolf optimizer based on neighborhood trust model for parameter identification of pemfc. Int J Hydrog Energy 2024;60:769–79.
[26] Shayeghi H, et al. A survey on microgrid energy management considering flexible energy sources. Energies 2019;12(11):2156.
[27] Agajie TF, et al. A comprehensive review on techno-economic analysis and optimal sizing of hybrid renewable energy sources with energy storage systems. Energies 2023;16(2):642.
[28] Sharma H, et al. Sizing a hybrid hydrogen production plant including life cycle assessment indicators using nsga-iii and pca. Energy Convers Manag: X 2023;18:100361.
[29] Tezer T. Multi-objective optimization of hybrid renewable energy systems with green hydrogen integration and hybrid storage strategies. Int J Hydrog Energy 2025.
[30] Zhang X, et al. Performance investigation and operation optimization of an innovative hybrid renewable energy integration system for commercial building complex and hydrogen vehicles. Energy 2024;301:131640.
[31] Mullanu S, Chua C, Molnar A, Yavari A. Artificial intelligence for hydrogen-enabled integrated energy systems: A systematic review. Int J Hydrog Energy 2025;141:283–303.
[32] Bareev-Rudy M, Schedler S, Clees T. Sizing optimization of hybrid hydrogen energy storage systems: A metamodel-based approach. Int J Hydrog Energy 2025.
[33] Ceylan C, Devrim Y. Design and simulation of the pv/pem fuel cell based hybrid energy system using matlab/simulink for greenhouse application. Int J Hydrog Energy 2021;46(42):22092–106.
[34] Bryan J, et al. Modeling and design optimization of carbon-free hybrid energy systems with thermal and hydrogen storage. Int J Hydrog Energy 2023;48(99):39097–111.
[35] Ruiming F. Multi-objective optimized operation of integrated energy system with hydrogen storage. Int J Hydrog Energy 2019;44(56):29409–17.
[36] Song Y, et al. Multi-objective optimization and long-term performance evaluation of a hybrid solar-hydrogen energy system with retired electric vehicle batteries. Int J Hydrog Energy 2024;62:867–82.
[37] Jamil H, Naqvi SSA, Kim DH. Hydrogen storage capability optimization based on multi-objective function for decision of hydrogen production and utilization. Int J Hydrog Energy 2024;95:1095–110.
[38] Roy TK, Saha S, Oo AMT. Optimizing hybrid energy systems for remote australian communities: The role of tilt angle in cost-effective green hydrogen production. Appl Energy 2025;391:125921.
[39] Wade F, et al. Optimal sizing and energy management of an integrated energy system coupling a hydrogen-fueled gas turbine with storage. Int J Hydrog Energy 2025;135:31–47.
[40] Mohandes B, et al. Renewable energy management system: Optimum design and hourly dispatch. IEEE Trans Sustain Energy 2021;12(3):1615–28.
[41] Hashmi R, Liu H, Yavari A. Semantic-aware interoperability for digital twins: A case study on hydrogen power plants. In: 2025 IEEE PES conference on innovative smart grid technologies-middle east. ISGT middle east, IEEE; 2025, p. 1–6.
[42] Giedraityte A, et al. Hybrid renewable energy systems—a review of optimization approaches and future challenges. Appl Sci 2025;15(4):1–30.
[43] Nallolla CA, et al. Multi-objective optimization algorithms for a hybrid ac/dc microgrid using res: A comprehensive review. Electronics 2023;12(4):1062.
[44] Holder D, Percy SD, Yavari A. A review of port decarbonisation options: Identified opportunities for deploying hydrogen technologies. Sustainability 2024;16(8). URL https://www.mdpi.com/2071-1050/16/8/3299.
[45] Holder DM, Yavari A. Port energy models alignment with real port activities, their coverage of hydrogen technologies, and as tools for decarbonisation. Int J Hydrog Energy 2025;150202.
[46] Khan T, Yu M, Waseem M. Review on recent optimization strategies for hybrid renewable energy system with hydrogen technologies. Int J Hydrog Energy 2022;47(60):25155–201.
[47] Yao Z, et al. Machine learning for a sustainable energy future. Nat Rev Mater 2023;8(3):202–15.
[48] Ambrose M. Rbee house averages [online]. 2019, URL https://public.tableau.com/app/profile/michael.ambrose/viz/Dahboards_AVGonly_Lastversionofdata-21082019_15664551425010/Dashboardbyenduse [Accessed: 22 2019].
[49] Parizad B, et al. An intelligent hybrid machine learning model for sustainable forecasting of home energy demand and electricity price. Sustainability 2024;16(6):2328.
[50] Zhang T, et al. Long-term energy and peak power demand forecasting based on sequential-xgboost. IEEE Trans Power Syst 2023;39(2):3088–104.
[51] Ripollés M Pitarch. Dimensionado y diseño de un parque solar fotovoltaico. 2020.
[52] Zhejiang. Espsc 380w-400w. 2025, https://www.enfsolar.com/pv/panel-datasheet/crystalline/44454.
[53] Caravantes D, et al. Estimation of hydrogen production potential from renewable resources in northern peru. Int J Hydrog Energy 2024;50:186–98.
[54] Hussam WK, Abdul-Niby M, Sheard GJ. Techno-economic analysis and optimization of hydrogen production from renewable hybrid energy systems: Shagaya renewable power plant-kuwait. Int J Hydrog Energy 2024;58:56–68.
[55] Marquedant JE. International electrotechnical commission. 2020.
[56] Bayborodina E, et al. Grid-scale battery energy storage operation in australian electricity spot and contingency reserve markets. Energies 2021;14(23):8069.
[57] HOPPECKE. Installation, commissioning and operating instructions for valve-regulated stationary lead–acid batteries. 2025, https://www.hoppecke.com/fileadmin/Redakteur/Hoppecke-Main/Products-Import/vrl_manual_en.pdf [Accessed 03 February 2025].
[58] Prakash K, et al. A review of battery energy storage systems for ancillary services in distribution grids. Front Energy Res 2022;10:971704.
[59] Clark C, Harris B. Valve regulated lead–acid battery degradation model for industry applications. In: World congress on engineering asset management. Springer; 2023, p. 203–14.
[60] Kostopoulos ED, Spyropoulos GC, Kaldellis JK. Real-world study for the optimal charging of electric vehicles. Energy Rep 2020;6:418–26.
[61] Cheraghi R, Jahangir MH. Multi-objective optimization of a hybrid renewable energy system supplying a residential building using nsga-ii and mopso algorithms. Energy Convers Manage 2023;294:117515.
[62] Eriksson E, Gray EM. Optimization of renewable hybrid energy systems–a multi-objective approach. Renew Energy 2019;133:971–99.

[63] IRENA. Scaling up electrolysers to meet the 1.5°C climate goal. 2020.
[64] Das HS, et al. Feasibility analysis of hybrid photovoltaic/battery/fuel cell energy system for an indigenous residence in east malaysia. Renew Sustain Energy Rev 2017;76:1332–47.
[65] Sadeghi D, Naghshbandy AH, Bahramara S. Optimal sizing of hybrid renewable energy systems in presence of electric vehicles using multi-objective particle swarm optimization. Energy 2020;209:118471.
[66] Abdellatif H, et al. Standalone hybrid renewable energy system optimization using linear programming. Arab J Sci Eng 2023;48(5):6361–76.
[67] Abdelhady S. Techno-economic study and the optimal hybrid renewable energy system design for a hotel building with net zero energy and net zero carbon emissions. Energy Convers Manage 2023;289:117195.
[68] Yadav S, Kumar P, Kumar A. Hybrid renewable energy systems design and techno-economic analysis for isolated rural microgrid using homer. Energy 2025;136442.
[69] Siemens. Siemens gamesa renewable energy. sg 2021:2.1e114. 2021, https://www.siemensgamesa.com/es-es/-/media/siemensgamesa/downloads/es/products-and-services/onshore/brochures/siemens-gamesa-onshore-wind-turbinesg-2-1-114-es.pdf.
[70] Basu S, John A, Kumar A. Design and feasibility analysis of hydrogen based hybrid energy system: a case study. Int J Hydrog Energy 2021;46(70):34574–86.
[71] Chamout MW, et al. Simulation and analysis of hybrid hydrogen-battery renewable energy storage for off-electric-grid dutch household system. Int J Hydrog Energy 2024;70:170–82.
[72] Meraghni S, Terrissa LS, Yue M, Ma J, Jemei S, Zerhouni N. A data-driven digital-twin prognostics method for proton exchange membrane fuel cell remaining useful life prediction. Int J Hydrog Energy 2021;46(2):2555–64.
[73] Glenk G, Holler P, Reichelstein S. Advances in power-to-gas technologies: cost and conversion efficiency. Energy Environ Sci 2023;16(12):6058–70.
[74] Tezer T, Yaman R. A pareto optimum approach and a power management strategy for a stand-alone wind turbine–pv–hydrogen system. Environ Prog Sustain Energy 2022;41(4):e13772.
[75] Ren H, et al. Multi-objective optimization of a hybrid distributed energy system using nsga-ii algorithm. Front Energy 2018;12(4):518–28.
[76] Vargas-Hákim G-A, Mezura-Montes E, Galván E. Evolutionary multi-objective energy production optimization: An empirical comparison. Math Comput Appl 2020;25(2):32.
[77] Alshammari NF, Samy MM, Barakat S. Comprehensive analysis of multi-objective optimization algorithms for sustainable hybrid electric vehicle charging systems. Mathematics 2023;11(7):1741.
[78] De Buck V, Nimmegeers P, Hashem I, Muñoz López CA, Van Impe J. Exploiting trade-off criteria to improve the efficiency of genetic multi-objective optimisation algorithms. Front Chem Eng 2021;3:582123.
[79] Morales-Hernández A, Van Nieuwenhuyse I, Rojas Gonzalez S. A survey on multi-objective hyperparameter optimization algorithms for machine learning. Artif Intell Rev 2023;56(8):8043–93.
[80] Hossain MA, et al. Multi-objective hybrid optimization for optimal sizing of a hybrid renewable power system for home applications. Energies 2022;16(1):96.
[81] Rong F, et al. Performance evaluation and multi-objective optimization of hydrogen-based integrated energy systems. Energy 2024;313:133698.
[82] Shah P, Agrawal R, Kachhwaha SS. Energy and exergy analysis of a hybrid renewable energy source. In: Recent advancements in mechanical engineering. Springer; 2020, p. 519–29.
[83] Li Z, et al. Modeling and multi-objective optimization of a stand-alone photovoltaic-wind turbine-hydrogen-battery hybrid energy system based on hysteresis band. Int J Hydrog Energy 2023;48(22):7959–74.
[84] Ma T, et al. Multi-objective optimal configuration of off-grid residential hybrid renewable energy system based on hypervolume-improved nsga-iii. Int J Hydrog Energy 2024;87:277–89.
[85] Pavankumar Y, Kollu R, Debnath S. Multi-objective optimization of photovoltaic/wind/biomass/battery-based grid-integrated hybrid renewable energy system. IET Renew Power Gener 2021;15(7):1528–41.
[86] Wu X, et al. Multi-objective and multi-algorithm operation optimization of integrated energy system. Int J Electr Power Energy Syst 2023;144:108529.
[87] Maheri A, Unsal I, Mahian O. Multiobjective optimisation of hybrid wind-pv-battery-fuel cell-electrolyser-diesel systems. Energy 2022;241:122825.
[88] Neumann F, Brown T. The near-optimal feasible space of a renewable power system model. Electr Power Syst Res 2021;190:106690.
[89] Fan Z, et al. Push and pull search embedded in an m2m framework for constrained multi-objective optimization. Swarm Evol Comput 2020;54:100651.
[90] Tangi M, Amaranto A. Designing integrated and resilient multi-energy systems via multi-objective optimization and scenario analysis. Appl Energy 2025;382:125281.
[91] Ahmadianfar I, Bozorg-Haddad O, Chu X. Gradient-based optimizer: A new metaheuristic optimization algorithm. Inform Sci 2020;540:131–59.
[92] Dehghani M, Hubálovský v, Trojovský P. Northern goshawk optimization: a new swarm-based algorithm for solving optimization problems. IEEE Access 2021;9:162059–80.
[93] Li JY, Zhan ZH, Zhang J. Evolutionary computation for expensive optimization: A survey. Mach Intell Res 2022;19(1):3–23.
[94] Mohamed AW, et al. Evaluating the performance of meta-heuristic algorithms on cec 2021 benchmark problems. Neural Comput Appl 2023;35(2):1493–517.
[95] Alsamia S, Albedran H, Jármai K. Comparative study of different metaheuristics on cec 2020 benchmarks. In: Vehicle and automotive engineering. Springer; 2022, p. 709–19.
[96] Tanabe R, Oyama A. A note on constrained multi-objective optimization benchmark problems. In: IEEE congress on evolutionary computation. CEC, 2017, p. 1127–34.
[97] Hassan MH, et al. Optimal power flow analysis with renewable energy resource uncertainty: a hybrid aeo-cgo approach. IEEE Access 2023;11:122926–61.
[98] Andersen PD, Silvast A. Experts, stakeholders, technocracy, and technoeconomic input into energy scenarios. Futures 2023;154:103271.
[99] Mahmoudi SM, Maleki A, Rezaei Ochbelagh D. Multi-objective optimization of hybrid energy systems using gravitational search algorithm. Sci Rep 2025;15(1):2550.
[100] Shaier AA, Elymany MM, Enany MA, Elsonbaty NA. Multi-objective optimization and algorithmic evaluation for ems in a hres integrating pv, wind, and backup storage. Sci Rep 2025;15(1):1147.
[101] Zhang T, Li W, Wang R. Surrogated-assisted multimodal multi-objective optimization for hybrid renewable energy system. Complex & Intell Syst 2023;9(4):4075–87.
[102] Ming F, Gong W, Zhen H, Li S, Wang L, Liao Z. A simple two-stage evolutionary algorithm for constrained multi-objective optimization. Knowl-Based Syst 2021;228:107263.
[103] Deng H, Wang J, Shao Y, Zhou Y, Cao Y, Zhang X, Li W. Optimization of configurations and scheduling of shared hybrid electric-hydrogen energy storages supporting to multi-microgrid system. J Energy Storage 2023;74:109420.
[104] Abdelsalam RA, Abdallah YS, Shabar NM, Afifi OA, Fouda MH, El-Deib AA. Energy management and techno-economic optimization of an isolated hybrid ac/dc microgrid with green hydrogen storage system. In: 2023 IEEE conference on power electronics and renewable energy. CPERE, IEEE; 2023, p. 1–7.
[105] Saleeb H, El-Rifaie AM, Sayed K, Accouche O, Mohamed SA, Kassem R. Optimal sizing and techno-economic feasibility of hybrid microgrid. Processes 2025;13(4):1209.
[106] Khan MA, Bayati N, Ebel T. Techno-economic analysis and predictive operation of a power-to-hydrogen for renewable microgrids. Energy Convers Manage 2023;298:117762.
[107] Qin H, Li K, Chen Z. Non-pareto genetic algorithm for optimal planning of multi-type energy resources in active distribution networks. Front Energy Res 2022;10:966549.
[108] Ridha HM, Hizam H, Mirjalili S, Othman ML, Ya'acob ME, Ahmadipour M, Ismaeel NQ. Multi-objective optimization and multi-criteria decision making aided by numerical method: Framework and a case study of malaysia and south africa. Energy Convers Manage 2022;274:116468.
[109] Kizielewicz B, Sałabun W. A robust framework for renewable energy policy evaluation using mcda and compromise ranking with stochastic weight identification. J Intell Manag Decis 2024;3:213–23.
[110] Bhatia M, Williams A. Using multi-criteria decision-making techniques to select criteria in renewable energy. Am J Oper Manag Inf Syst 2023;8(2):21–9.
[111] Dhruva S, Krishankumar R, Pamucar D, Zavadskas EK, Ravichandran KS. Demystifying the stability and the performance aspects of cocoso ranking method under uncertain preferences. Informatica 2024;35(3):509–28.
[112] Miyandoab SZ, Rahnamayan S, Bidgoli AA, Ebrahimi S, Makrehchi M. Enhancing diversity in multi-objective feature selection. In: 2024 IEEE congress on evolutionary computation. CEC, IEEE; 2024, p. 1–8.
[113] Zhang Z, Yang F, Cheng R, Ma Y. Paretotracker: Understanding population dynamics in multi-objective evolutionary algorithms through visual analytics. IEEE Trans Vis Comput Graphics 2024.
[114] Xu X-F, Wang K, Ma W-H, Wu C-L, Huang X-R, Ma Z-X, Li Z-H. Multi-objective particle swarm optimization algorithm based on multi-strategy improvement for hybrid energy storage optimization configuration. Renew Energy 2024;223:120086.
[115] Kamarposhti M Ahmadi, Ghandour R, Abdel-Aty M, Hafez M, Alfiras M, Alkhazaleh S, Colak I, Solyman A. Optimizing capacitor bank placement in distribution networks using a multi-objective particle swarm optimization approach for energy efficiency and cost reduction. Sci Rep 2025;15(1):12332.
[116] Su R, He G, Su S, Duan Y, Cheng J, Chen H, Wang K, Zhang C. Optimal placement and capacity sizing of energy storage systems via nsga-ii in active distribution network. Front Energy Res 2023;10:1073194.
[117] Nikolikj A, Cenikj G, Ispirova G, Vermetten D, Lang RD, Engelbrecht AP, Doerr C, Korošec P, Eftimov T. Assessing the generalizability of a performance predictive model. In: Proceedings of the companion conference on genetic and evolutionary computation. 2023, p. 311–4.
[118] Kwon K, Lee H-B, Kim N, Park S, Joshua SR. Integrated battery and hydrogen energy storage for enhanced grid power savings and green hydrogen utilization. Appl Sci 2024;14(17):7631.
[119] Shiraishi K, Park WY, Kammen DM. The role of hydrogen as long-duration energy storage and as an international energy carrier for electricity sector decarbonization. Environ Res Lett 2024;19(8):084011.

[120] Banihabib R, Fadnes FS, Assadi M. Techno-economic optimization of microgrid operation with integration of renewable energy, hydrogen storage, and micro gas turbine. Renew Energy 2024;237:121708.
[121] Arsalis A, Georghiou GE, Papanastasiou P. Recent research progress in hybrid photovoltaic–regenerative hydrogen fuel cell microgrid systems. Energies 2022;15(10):3512.
[122] Shaikh RA, Vowles DJ, Allison A, Abbott D. Evaluation of australia's generation-storage requirements in a fully renewable grid with intermittent and flexible generation. IEEE Access 2023;11:64201–18.
[123] Daniel T, Xing L, Cai Q, Liu L, Xuan J. Potential of progressive and disruptive innovation-driven cost reductions of green hydrogen production. Energy Fuels 2024;38(11):10370–80.
[124] Hargroves K, James B, Lane J, Newman P. The role of distributed energy resources and associated business models in the decentralised energy transition: A review. Energies 2023;16(10):4231.
[125] Andeobu L, Wibowo S, Grandhi S. Renewable hydrogen for the energy transition in australia-current trends, challenges and future directions. Int J Hydrog Energy 2024;87:1207–23.